Paravalvular sealing of percutaneous heart valves

by

David Gideon Conradie

CNRDAV002

SUBMITTED TO THE UNIVERSITY OF CAPE TOWN

In fulfilment of the requirements for the degree

MSc (Biomaterials)

(by dissertation only)

CHM6021W

Faculty of Health Sciences

UNIVERSITY OF CAPE TOWN

Cardiovascular Research Unit, Chris Barnard Division of Cardiothoracic Surgery

Date of submission:	**23 August 2018**
Supervisor:	**Assoc. Prof Deon Bezuidenhout**
Co-supervisor:	**Dr. Jandre de Villiers**

Abstract

Paravalvular regurgitation (PVR), which frequently occurs after transcatheter aortic valve replacements (TAVR) can lead to adverse clinical consequences and has been shown to correlate to an increased late mortality and morbidity. Quantification, graduation and testing for PVR has proven challenging and a standardized method for pre-clinical testing is still sought. Commercial transcatheter heart valves (THV's) rely on sealing skirts made from treated pericardium or polyethylene terephthalate (PET) fabrics. The current study was aimed at developing novel electrospun skirts for the minimization of PVR in THV's.

Thermoplastic polyurethane (TPU) was electrospun onto mandrels and several techniques (CO_2 – laser, ultra-sonic, solvent and conductive heat bonding) used to attach the scaffolds to pre-coated TAVR stents. Attachment strength was modelled by finite element analysis (FEA) of stents in the crimped and expanded conditions and empirically determined by physical pull-off tests. PVR was evaluated for four different skirt designs (1× single layer "FLAT" and 3× double layers: Forward Flow Filling "FFF", No Filling "NF" and Back Flow Filling "BFF") using a pulse duplicator fitted with perforated mounting rings.

Optimization of solution, process and environmental parameters yielded scaffolds with average fibre diameters of 3.17 ± 0.64 µm and average pore sizes 9.52 ± 6.90 µm. Tensile strength was found to be similar in the direction perpendicular to collector rotation ($UTS_{\perp}$ = 5.96 ± 1.98 MPa) to the direction parallel to rotation ($UTS_{//}$ = 5.42 ± 2.91 MPa) (p=0.188), with 10% secant moduli of 1.71 ± 0.43 MPa and 1.53 ± 0.43 MPa, respectively. Conductive heat bonding proved the most successful in terms of reproducibility and accessibility and was further developed into semi-automated bonding processes. FEA showed the relative displacement of high strain areas and bond strengths sufficient to withstand 67% to 134% strain (depending on skirt embodiment). Attachment strength was observed to increase with stent pre-coating thickness. Dual layered skirts improved sealing (over single layered method). The BFF skirt concept was found to have superior sealing capabilities across all simulated conditions with a mean total aortic regurgitation fraction (ARF%) of 6.85 ± 0.67 % compared to the control FLAT skirt with 13.84 ± 1.38%. Splitting the ARF% into its leakage (LF) and closing fraction (CF) components confirmed superior sealing efficiency of the BFF skirt (LF = 2.96 ± 0.72 % compared to 12.00 ± 1.84 % for the control FLAT skirt).

Electrospun scaffolds were successfully spun and attached to balloon expandable TAVI stents for effective use as sealing skirts. The dual layered concepts showed promising results and are currently being employed in large animal trials.

Graphical Abstract

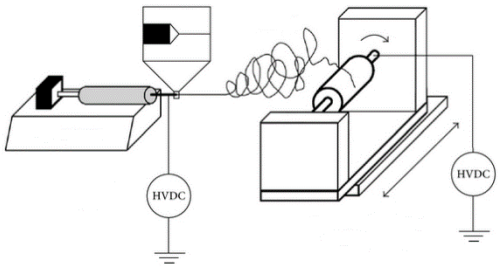

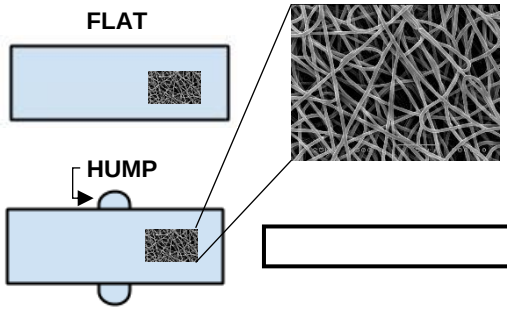

Scaffold Characterization:
Fiber diameter
Pore Size
Porosity
Isotropy
Permeability
Mechanical

SKIRT ELECTROSPINNING

CONDUCTIVE HEAT ULTRASONIC LASER SOLVENT

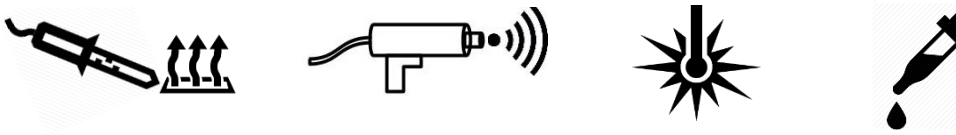

BONDING OF SKIRT TO VALVE STENT

FLAT **H-FFF** **H-NF** **H-BFF**

Attachment Strength:
FEA
PULL-OFF
FATIGUE

PULSE DUPLICATOR

PERFORATED MOUNTING RINGS

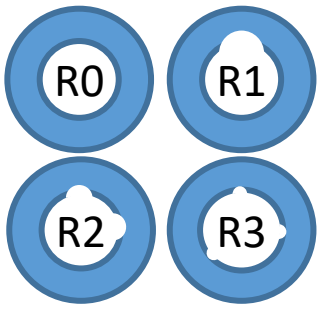

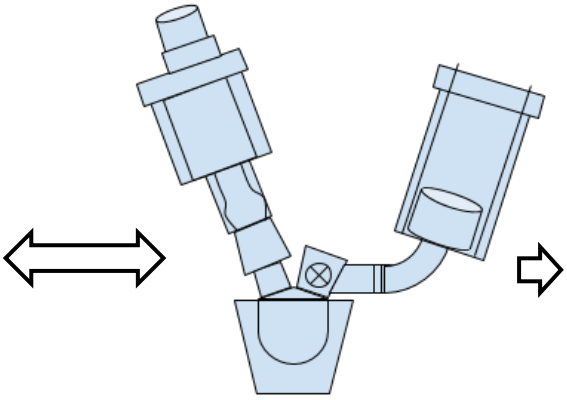

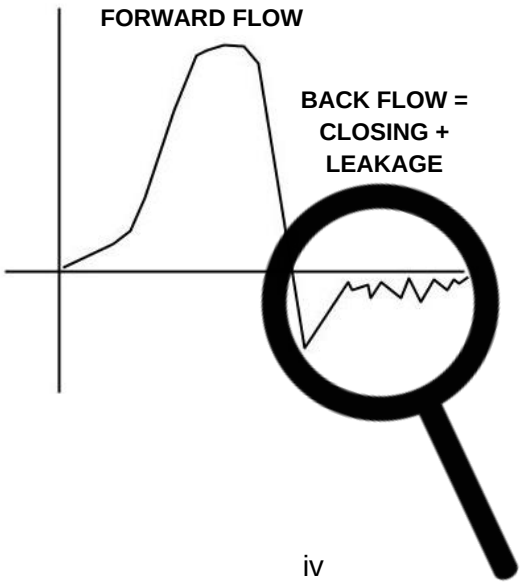

PARAVALVULAR SEALING STUDY

Acknowledgements

"Little by little one travels far" – J.R.R Tolkien

Completion of this thesis would not have been possible without the plethora of colleagues, friends and mentors at **Strait Access Technologies** (SAT) and the **Cardiovascular Research Unit** (CRU). I would like to express sincere thanks to each of you for helping me come this far. I would also like to thank the following people and institutions specifically, for without them this journey would not have been possible:

First and foremost, I would like to thank my supervisor **Assoc. Prof Deon Bezuidenhout** for his extensive guidance and stellar support on this journey. For always having an open door and for always knowing we would make it although I sometimes did not. Also, for instilling in me an interest in biomaterials while teaching me to ask the right questions. To my co-supervisor, **Dr Jandre de Villiers** for the immense amount of help in all aspects of this thesis. Thank you for helping me stay calm, hearing me out when I was at a dead end and helping me interpret the data and making sense of it all. You are a gentleman and a scholar.

To my friend, colleague and confidant that started this journey with me, **Johan Coetzee** – thank you for all the help and support in the physical and cognitive realms. To **Joel du Toit** for being such a dependable and organized help in all the physical testing aspects of this dissertation. To **Aminah Rujub** for always being there and willing to help with a smile on her face in even the smallest of tasks. To **Bruce de Jong** for helping me create the renderings in this dissertation and designing the first bonding rig. To **Dr Harish Appa** for helping me with all things related to FEA and generally always being supportive. To **Robin Smith** for helping me with and teaching me the ways of the pulse duplicator. To **Wesley Elson** for undertaking the task with me of understanding, improving and maintaining the electrospinning setup. To **Ursula Saralina** for stitching the valve leaflets and to **Preyen Perumall** for applying his mind so wonderfully to the 2nd iteration bonding rig. I would also like to thank **Carissa van der Merwe** for her help with the permeability testing.

A big thank you to the CRU and all the students and technical staff that crossed paths with me. Especially **Wian van den Bergh** for his tremendous help with the many technical aspects of image analysis and **Rumbidzai Damita Zireva** for the positive influences you have had on me and helping me see things from a different perspective.

To **Miranda Waldron** at the Electron Microscope Unit on upper campus for her guidance in using the SEM and her willingness to help.

Then, to my housemates, friends and family that all had an impact on my journey, thank you for always encouraging me and listening to what I had to say. And then lastly, a very special thank you to my then girlfriend and now wife **Julia Conradie** for staying with me each step of the way, building me up when I was at a low point and helping me with structure and flow not only in my thesis but also in life.

Funding was generously provided by SAT.

Declaration

I, ***David Gideon Conradie***, hereby declare that the work on which this dissertation/thesis is based is my original work (except where acknowledgements indicate otherwise) and that neither the whole work nor any part of it has been, is being, or is to be submitted for another degree in this or any other university.

I empower the university to reproduce for the purpose of research either the whole or any portion of the contents in any manner whatsoever.

Signature: …Signed by candidate…..Date: ……29.07.2019…….

Table of Contents

List of Abbreviations

AR	Aortic regurgitation
AR-index	Aortic regurgitation index
AS	Aortic stenosis
ASE	American Society of Echocardiography
AV	Aortic valve
AVC	Aortic valve calcium
CAC	Coronary artery calcium
CMR	Cardiovascular magnetic resonance
CSI	Calcification scoring index
DBP	Diastolic blood pressure
DBT-index	Diastolic pressure time index
DLZ-CS	Device landing zone calcification score
EOA	Effective orifice area
ePTFE	Expanded polytetrafluoroethylene
EROA	Effective regurgitant orifice area
ESC	Environmental stress cracking
FDA	Food and Drug Administration (U.S.A)
FEA	Finite element analysis
HS	Hard segment
LA	Left atrium
LV	Left ventricle
LVEDP	Left ventricle end-diastolic pressure
LVOT	Left ventricular outflow tract
MIO	Metal ion oxidation
MSCT	Multi slice computed tomography
PARTNER	Placement of transcatheter valves (clinical trial)
PCU	Poly(carbonate)urethane
PD	Post dilatation or Pulse duplication
PET	Polyethylene terephthalate
PEU	Poly(ether)urethane
PISA	Proximal isovelocity surface area
POSS-PCU	Polyhedral Oligomeric Silsesquioxane Poly(Carbonate-urea) urethane
PU	Polyurethane
PVR	Paravalvular regurgitation
PW	Pulsed wave
RA	Right atrium
REPRISE	Repositionable Percutaneous Replacement of Stenotic Aortic Valve Through Implantation of Lotus™ Valve System
RHD	Rheumatic heart disease
RV	Right ventricle
SAVR	Surgical aortic valve replacement
SBP	Systolic blood pressure
SPU	Segmented polyurethane
SS	Soft segment
TAVI-ECS	Transcatheter aortic valve implantation echocardiographic calcification score
TAVR	Transcatheter aortic valve replacement
TCT	Transcatheter Cardiovascular Therapeutics (Congress)
TEE	Transesophageal echocardiography
THV	Transcatheter heart valve
TTE	Transthoracic echocardiography
VARC	Valve Academic Research Consortium

Nomenclature/Glossary

Angina	A condition marked by severe pain in the chest, often also spreading to the shoulders, arms, and neck, owing to an inadequate blood supply to the heart.
Annulus	A ring shaped structure, object or region
Antegrade	In the direction of normal movement, as in blood flow or peristalsis.
Atrioventricular block	A type of heart block in which the conduction between the atria and ventricles of the heart is impaired.
Biocompatibility	Not harmful or toxic to living tissue.
Bovine	Relating to or affecting cattle.
Cardio pulmonary bypass	A technique that temporarily takes over the function of the heart and lungs during surgery, maintaining the circulation of blood and the oxygen content of the patient's body.
Cardiovascular Magnetic Resonance (CMR)	A medical imaging technology for non-invasive assessment of the function and structure of the cardiovascular system.
Circumferential extent	A measure used to graduate the severity of prosthetic valve regurgitation
Coaptation	A joining or adjustment of parts to one another.
Collagenous	Any of a class of extracellular proteins abundant in higher animals, especially in the skin, bone, cartilage, tendon, and teeth, forming strong insoluble fibers and serving as connective tissue between cells.
Commissure	A point or line of union or junction especially between two anatomical parts.
Congenital	Of a disease or physical abnormality present from birth.
Contrast medium	A substance introduced into a part of the body to improve the visibility of internal structures during radiography.
Coronary arteries	Arteries supplying blood to the heart.
Diamines	A compound whose molecule contains two amino groups, especially when not part of amide groups.
Diastole	The phase of the heartbeat when the heart muscle relaxes and allows the chambers to fill with blood.
Diastolic flow reversal	A brief reversal of flow early in diastole, usually seen in the ascending aorta of patients with aortic regurgitation.
Diisoocyanate	A compound containing two isocyanate groups in the molecule and sometimes used in making resins and plastics.
Doppler Echocardiography	A procedure that uses Doppler ultrasonography to examine the heart.
Echocardiography	An imaging technique that use ultrasound to examine the structure and functioning of the heart for abnormalities and disease.
Embolization	Occurring when the valve prosthesis moves during or after deployment such that it loses contact with the aortic annulus.
Environmental stress cracking	Failure of plastic due to continuously acting external and/or internal stresses in the presence of surface active substances.
Etiologies	The cause, set of causes, or manner of causation of a disease or condition.
Extra cellular matrix	A collection of extracellular molecules secreted by support cells that provides structural and biochemical support to the surrounding cells.
Fibrosis	The thickening and scarring of connective tissue.
Finite element analysis	A type of computer program that uses the finite element method to analyze a material or object and find how applied stresses will affect the material or design.
Glutaraldehyde	A compound that contains two aldehyde groups which is used especially in tanning leather and in the fixation of biological tissues
Hemodynamic	Relating to the flow of blood within the organs and tissues of the body
Hounsfield unit	A quantity commonly used in computed tomography to express CT numbers in a standardized and convenient form.

Hydrodynamic	Relating to the motion of fluids under the influence of internal and external forces.
Hydrolytic	Chemical process of decomposition involving the splitting of a bond and the addition of the hydrogen cation and the hydroxide anion of water.
Hypertension	Abnormally high blood pressure
In-vitro	Testing in an artificially simulated physiological condition.
In-vivo	Testing inside a living organism.
Left atrial appendage	A small, ear-shaped sac in the muscle wall of the left atrium
Left ventricular outflow tract	A portion of the left ventricle of the heart through which blood passes to enter the great arteries.
Long axis	A line parallel to an object lengthwise, as in the body the imaginary line that runs vertically through the head down to the space between the feet.
Metal ion oxidation	Oxidation of polymers by strong oxidative agents in the form of metal ions
Multi slice computed tomography	A form of computed tomography (CT) technology for diagnostic imaging able to acquire multiple slices or sections simultaneously.
Nitinol	A metal alloy of nickel and titanium with shape memory characteristics.
Nodules of Arantius	Thickenings of the tunica intima layer covering the ventricular aspect of the leaflets of the aortic valve.
Pacing	Means of temporarily pacing a patient's heart during a medical emergency or surgery
Parasternal	Situated beside the sternum
Paravalvular	Adjacent to or in the vicinity of a prosthetic valve
Percutaneous	Made, done, or effected through the skin.
Pericardial tissue	Pertaining to the conical sac of fibrous tissue that surrounds the heart and the roots of the great blood vessels.
Platelet	A small disc-shaped cell fragment without a nucleus, found in large numbers in blood and involved in clotting.
Polyols	Organic compounds containing multiple hydroxyl groups
Porcine	Relating to or affecting a pig or pigs
Sclerosis	Abnormal hardening of body tissue
Short axis	Line through and perpendicular to an object's long axis. This line may intersect the long axis anywhere within the object**.**
Sino tubular junction	The region of the ascending aorta between the aortic sinuses (of Valsalva) and where the normal tubular configuration of the aorta is attained.
Sinuses of Valsalva	Any one of the pouches of the aorta and pulmonary artery which are located behind the flaps of the semilunar valves and into which the blood in its regurgitation toward the heart enters and thereby closes the valves.
Stenosis	The abnormal narrowing of a passage in the body.
Suprasternal	Situated above or measured from the top of the sternum.
Syncope	Temporary loss of consciousness caused by a fall in blood pressure.
Systole	The phase of the heartbeat when the heart muscle contracts and pumps blood from the chambers into the arteries.
Thoracotomy	Surgical incision into the chest wall.
Thromboembolic	Pertaining to the blockage of a blood vessel by a thrombus carried through the bloodstream from its site of formation.
Transcatheter	Taking place through a catheter.
Transvalvular	Across a valve.
Vena cava	A large vein carrying deoxygenated blood into the heart.

List of figures

List of tables

1. Introduction

Aortic stenosis (AS) is one of the leading cardiovascular diseases found in the Western world (after hypertension and coronary artery disease) and can affect up to 5% of the elderly population (Bates, 2011; Maganti, Rigolin, Sarano, & Bonow, 2010). On the other hand, rheumatic heart disease (RHD) is one of the most prevalent diseases found in the developing world and is usually caused by poor living standards and a lack of access to proper medical facilities. RHD starts as a simple streptococcal throat infection and is estimated to progress in 60% of cases from rheumatic fever to RHD (Sliwa & Zilla, 2012) and can lead to commissural fusion and decreased valve function.

When it comes to valve replacement, open heart surgery is the gold standard (Yuan et al., 2013). The patient is placed on cardiopulmonary bypass, the diseased valve is excised and replaced by suturing in a mechanical or bio-prosthetic valve. Mechanical valves can last more than 25 years but due to design, material choice and hemodynamic performance, lifelong anti-coagulant treatment is required to prevent thromboembolic events. In contrast, surgically implanted bio-prosthetic valves have more natural hemodynamic performance and only require anticoagulation therapy for a brief period after implantation. They are however prone to calcific degeneration and the durability is less than that of mechanical valves (Tillquist & Maddox, 2011). These valve replacement procedures are expensive and require sophisticated hospital facilities which do not always make them viable options for patients in developing countries.

In the last 15 years, transcatheter aortic valve replacement (TAVR) has emerged as an effective alternative treatment option to surgical aortic valve replacement (SAVR), initially for patients with severe symptomatic AS who were considered inoperable (Merten et al., 2013). TAVR development has made tremendous progress in the last decade and a half with proven safety and efficacy for intermediate risk patients, setting the stage for even lower risk patients and wider use (Agarwal, Kapadia, Tuzcu, & Krishnaswamy, 2016). Transcatheter heart valves make use of collapsible metal frames to which chemically treated pericardial tissue leaflets are sutured. The two leading commercially available TAVR valves are the balloon-expandable Edwards Sapien XT™ (Cobalt-Chromium) and the self-expanding Medtronic CoreValve Evolut™ (Nitinol®). Even though this method of valve replacement has many advantages over surgically implanted valves, complications can arise during and after the procedure.

One of the main complications that arise after a TAVR procedure is the potential occurrence of paravalvular regurgitation (PVR) which has been associated with increased post-procedural mortality and one of the reasons why TAVR valves are not more widespread in use (Lerakis, Hayek, & Douglas, 2013). PVR can be defined as blood leaking back into the ventricle between the prosthesis and the walls of the aorta. This can happen due to valve malposition, prosthesis/annulus mismatch or the native anatomy being heavily calcified, with resulting irregular surface, potentially leading to voids forming between the prosthesis and the annulus. In the United Kingdom (UK), PVR was present in up to 60% of patients after TAVR, and AR has been shown to be an independent predictor of mortality (Moat et al., 2011). To address PVR, commercial TAVR valves contain sealing skirts attached to stents to minimize the effect of voids caused by suboptimal apposition. Most skirts consist of a single layer, and improve sealing if valve positioning is correct, but cannot fully compensate for malposition, under-sizing or voids larger than a certain size. In the case of RHD, the native valve and surrounding anatomy could be dilated and/or compliant, which may require a different approach for TAVR sealing compared to that used for a stenotic valve.

Materials used in sealing skirts for commercial TAVR valves are either woven or knitted Dacron® (Polyethylene terephthalate (PET)) fabric, treated pericardial tissue or polyurethane film, that are usually sutured in a single layer to the collapsible frame. Woven and knitted PET provides a versatile solution, with a confirmed clinical history for use in cardiovascular and other applications. Coatings such as gelatin or fibrin gel may be applied to improve performance and reduce the porosity of the open structures. Chemically treated pericardial tissue has been used for nearly 50 years as valve leaflets or cardiac patches, making it a very well researched topic and sensible material choice as a sealing skirt.

Dual layered electrospun scaffolds are proposed as an alternative to the current sealing skirts. Electrospinning is a process that makes use of an electrostatic field to draw micro to nanosized fibers from a polymer solution, creating an interconnected porous structure. The process permits the scaffold to be manufactured from a wide variety of biocompatible materials and in a chosen geometry by using custom collecting mandrels. Potential subsequent tissue ingrowth into a sealing skirt of a transcatheter valve could be desirable as it would help with anchorage and provide permanent sealing. Additionally, an electrospun scaffold can be manufactured from a biocompatible material and fulfill the requirements for a sealing skirt similar to Dacron or pericardial tissue.

Requirements for stented replacement valves are stringent, needing to open and close 40 million times a year while maintaining good hydrodynamic function, successful anchoring in the conduit to prevent embolization or migration, and proper sealing once fully deployed.

Additionally, the sealing skirt should have adequate attachment strength and elongation to survive the forces experienced by the skirt during crimping and expansion as well as sheathing and re-sheathing. This project and the resulting thesis forms part of a larger TAVR valve project undertaken by researchers at the Cardiovascular Research Unit at the University of Cape Town and Strait Access Technologies. This study investigates the manufacturing and attachment processes of the scaffold and then concentrates on the sealing aspects of the skirt to prevent PVR.

2. Literature review

2.1. Valvular disease and current surgical solutions

The human heart contains four chambers and four one-directional valves. During diastole, the heart muscle relaxes and deoxygenated blood from the superior and inferior vena cava as well as the coronary arteries fills the right atrium (RA), leading to increased atrial pressure. When the pressure within the RA exceeds that of the right ventricle (RV) the tricuspid valve opens, allowing blood to flow to the RV. As pressure builds due to the filling and the RV contracts, the tricuspid valve closes, and the pulmonary valve ejects the blood through the pulmonary arteries into the lungs where oxygenation takes place. The newly oxygenated blood reaches the left atrium (LA) through the pulmonary veins. When the pressure in the LA exceeds that of the left ventricle (LV) it passes through the mitral valve into the LV. Rising pressure due to the increase in the ventricular chamber volume leads to the mitral valve closing and the oxygenated blood to be ejected through the aortic valve by a contraction motion of the LV and distributed throughout the body and heart via the circulatory system and coronary arteries (Shah, Gnanasegaran, Sundberg-Cohon, & Buscombe, 2009) (See Figure 1). When any of these valves become stenotic or regurgitant due to calcification or disease, the heart must work harder to prevent pressure and volume overload.

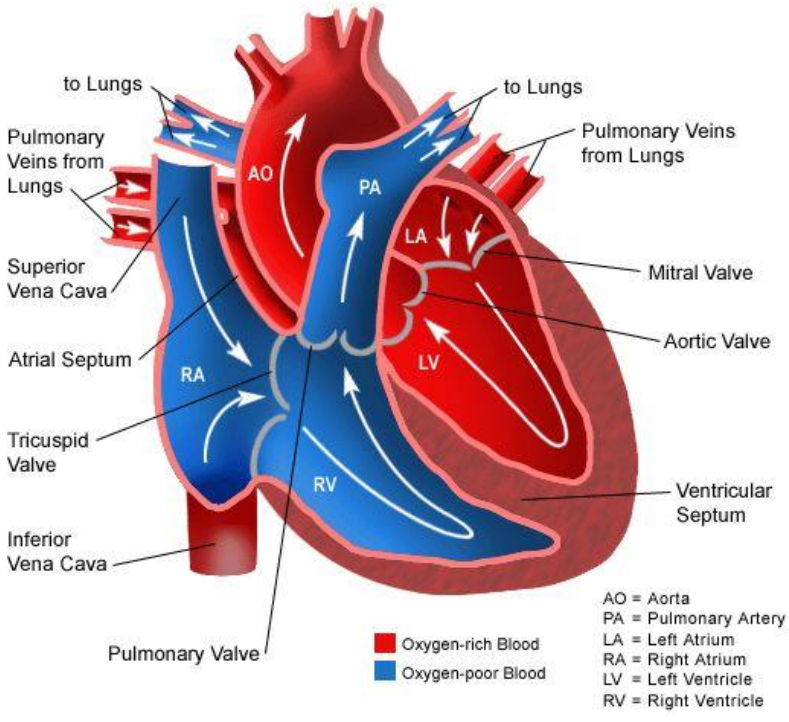

Figure 1: Gross anatomy of the heart

The aortic valve consists of three leaflets, each having a free edge with thickened ends, called the nodules of Arantius which act as the coaptation zone, a belly and the basal attachment part. They attach in a crown shape by inserting into the wall, forming a fibrous structure which is usually called the annulus. The three bulges behind the leaflets are named the sinuses of Valsalva, where from the right and left sinuses, the coronary arteries originate at the coronary ostia. The commissures are where the attachment points of the leaflets converge and insert into the aortic wall forming the sino-tublar junction. Below the commissures, extensions of the left ventricular outflow tract (LVOT) are found in the form of thinned aortic wall and are termed the inter-leaflet triangles (see Figure 2). During valve replacement procedures, damage to the inter-leaflet areas should be avoided since it could lead to permanent conduction problems (Charitos & Sievers, 2013).

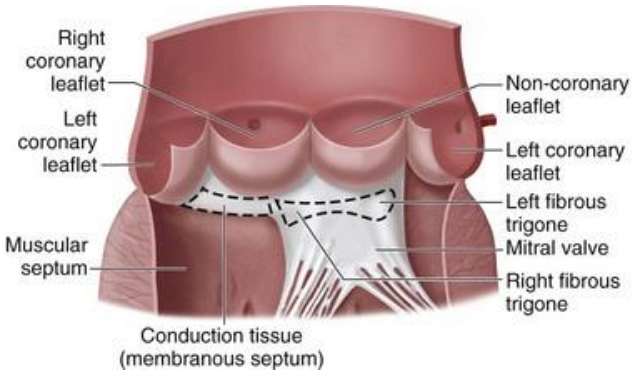

Figure 2: The aortic complex

Broadly, valvular diseases can be classified into aortic stenosis (AS) or aortic regurgitation (AR). AS implies a narrowing of the aortic valve (AV) due to stiffening or fusion of the leaflets, which leads to incomplete opening. This could be caused by degenerative calcification, RHD or the gradual stenosis of a congenital bicuspid valve (Maganti et al., 2010) (see Figure 3).

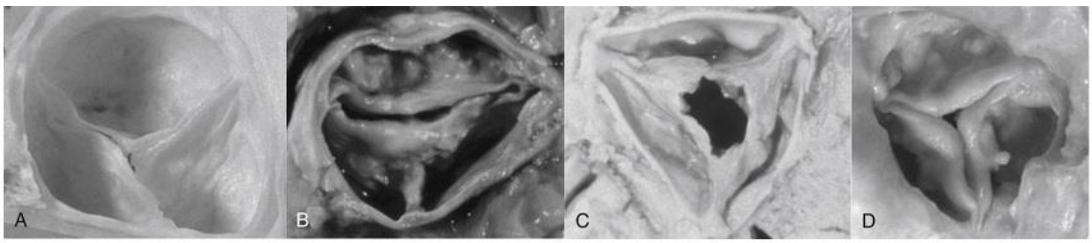

*Figure 3: Aortic valve pathologies. (**A**) Healthy, (**B**) Bicuspid, (**C**) Rheumatic and (**D**) Calcific Stenosis*

This narrowing prevents the heart from pumping sufficient blood to the rest of the body, leading to pressure overload in the ventricle, resulting in symptoms that include shortness of breath, angina, syncope or death (Carabello & Paulus, 2009). In contrast, AR implies that the valve does not fully close, and blood can leak back or regurgitate into the ventricle (see Figure 4). This volume overload results in ventricular hypertrophy where the chamber

volume increases, and pumping efficiency decreases. AR can be caused by a myriad of etiologies including but not limited to fibrosis, infection, calcification, dilatation of the valve and degeneration (W. Zoghbi, 2003).

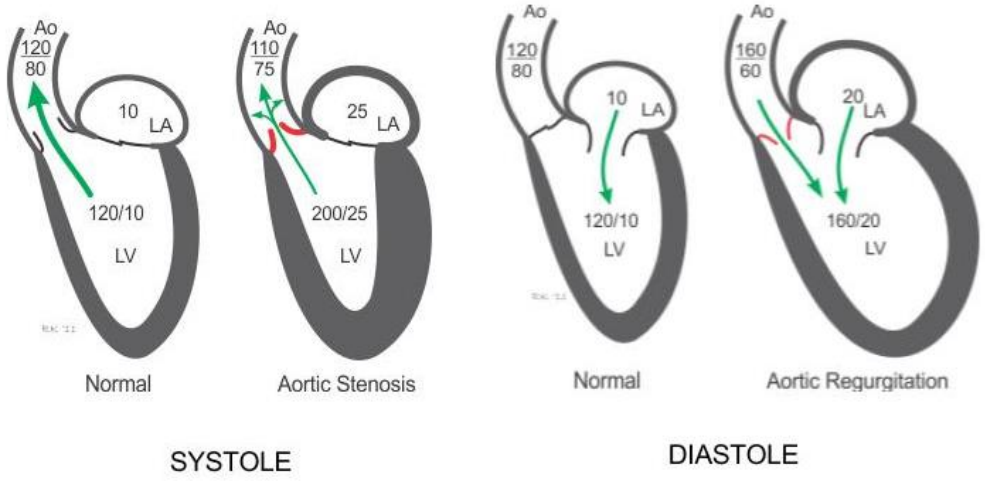

Figure 4: Schematic representation of aortic stenosis and regurgitation with representative pressures within the relative chambers

A survey conducted in 2001 in Europe, including 5001 adult patients with a mean age of 64 ± 14 years, found that from the patients suffering from single native left-side valvular disease (2779 patients), AS was the most prominent condition with 1197 patients (43.1%) and AR, with 369 patients (13.3%) was third most prominent (Iung et al., 2003).

The early 1960s marked the era where the first successful, surgically implanted mechanical heart valve replacements were reported (Braunwald, 2000). These were open heart surgical procedures, requiring a full thoracotomy and excision of the diseased valve which would then be replaced with a mechanical valve such as the St Jude Medical bi-leaflet valve (see Figure 5). Such mechanical valves require patients to undergo lifelong anticoagulation therapy due to but not limited to, the high shear stresses that is experienced by the blood as it flows through the valve, which can lead to platelet activation and potential thromboembolic events (Kulik, Rubens, Mesana, & Lam, 2006). When looking at a mechanical valve as a treatment option, the major factors to consider are the patient's life expectancy (age younger than 65) and willingness to undergo long-term anticoagulation (Pibarot & Dumesnil, 2009).

Another surgical treatment option for heart valve replacement is the use of bio-prosthetic tissue valves which mimic the natural anatomy of the tricuspid aortic valve. They can be stented, where either chemically treated porcine valves (e.g. Medtronic Hancock) or pericardial tissue (e.g. Carpentier-Edwards Perimount valve) are attached to a support frame via sutures, or stentless, where a full porcine root (e.g. Medtronic Freestyle) (see Figure 5)

is excised and chemically treated. The major advantage of tissue valves is that patients do not require lifelong anticoagulation therapy since the valve function mimics that of the native valve and hence induces lower shear stresses on blood that can cause platelet activation. The difficult choice between the use of mechanical valves and bio-prosthetic tissue valves is very patient-specific and many factors should be considered. A study analysis from a single-center dataset in Canada shows, in that population, the surgical bio-prosthetic option with its reduced risk of bleeding throughout the patient's life, compared to mechanical valves, outweighs the increased risk of structural valve deterioration and consequent risk for reoperation, and hence is seen as the superior therapy choice (van Geldorp et al., 2008). Once again when choosing a suitable valve replacement prosthesis, patient life expectancy must be considered. Additionally, if the patient is a woman of childbearing age valve choice has to be evaluated, since the use of anticoagulation during pregnancy can lead to increased chances of hemorrhage and other adverse complications to the mother and fetus (Gibson & Powrie, 2009).

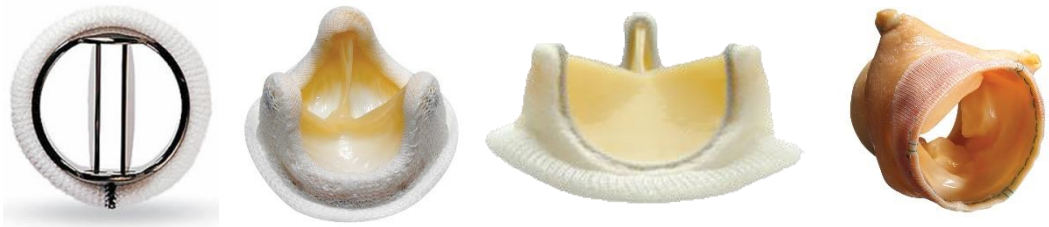

Figure 5: From left to right - St Jude bi-leaflet mechanical valve, Medtronic Hancock and Carpentier-Edwards Perimount skirted tissue valves, Medtronic Freestyle stentless bio-prosthesis

In a randomized controlled trial running from 1995-2003, where the mean patient age was 64, 165 patients received bio-prosthetic valves and 155 patients' mechanical valves. Results from the study showed no significant difference between overall mortality (Kaneko, Cohn, & Aranki, 2013).

A new procedure, namely transcatheter aortic valve replacement (TAVR) which do not require open heart surgery is a recent treatment option that has arisen and is deemed the best choice for patients with aortic stenosis that have been identified as inoperable or at too high risk to survive a sternotomy and pulmonary bypass (Ye, Soon, & Webb, 2012). The first successful implantation of a transcatheter heart valve (THV) was done in 2002 in France. After open heart surgery was declined for the 57-year-old male patient with calcific aortic stenosis, a stented bovine valve was implanted using the antegrade transseptal catheter approach. The 48 hours post implantation showed clinical improvements with reduced signs of heart failure. In the subsequent 4 month follow-up ,however several noncardiac-related

complications arose, eventually leading to death at 17 weeks post-TAVR (A. Cribier et al., 2002).

2.2. Minimally invasive transcatheter aortic valve replacement (TAVR)

In 2011, nearly 10 years after the first successful TAVR procedure, the United States Food and Drug Administration (FDA) approved the balloon expandable Edwards Sapien THV™ for clinical use in patients who are at high risk for open heart surgery. This initial valve was manufactured at diameters of 23 mm and 26 mm, the latter being made specifically to solve the high degree of PVR observed in the initial Rouen series of TAVR (A. G. Cribier, 2014). The Sapien valves are all similar in design, making use of treated pericardial leaflets sutured to a PET fabric sealing skirt, which in turn is attached to the metal stent frame. The Edwards Sapien XT, approved in 2014 by the FDA is the successor to the Sapien THV. It boasts improved stent material choice and design, leading to improved radial strength and a decreased crimp profile. The Edwards Sapien XT (see Figure 6) at a diameter of 23 mm has an expanded height of 14.3 mm and an inner fabric skirt which extends up from the bottom to a height of 9.9 mm. The Edwards Sapien 3™ is the 3rd iteration with further stent design improvements leading to a lower crimp profile and decreased stent lengthening, but also improved circularity. The Edwards Sapien 3 (see Figure 6) at a 23 mm diameter has an expanded height of 18 mm and an inner and outer skirt height of 9.3 and 6.6 mm respectively. Recently the FDA approved the Edwards Sapien 3 and XT for use in intermediate risk patients. Furthermore, the Sapien 3 became the first THV approved for valve-in-valve treatment when previously placed aortic or mitral valves fail.

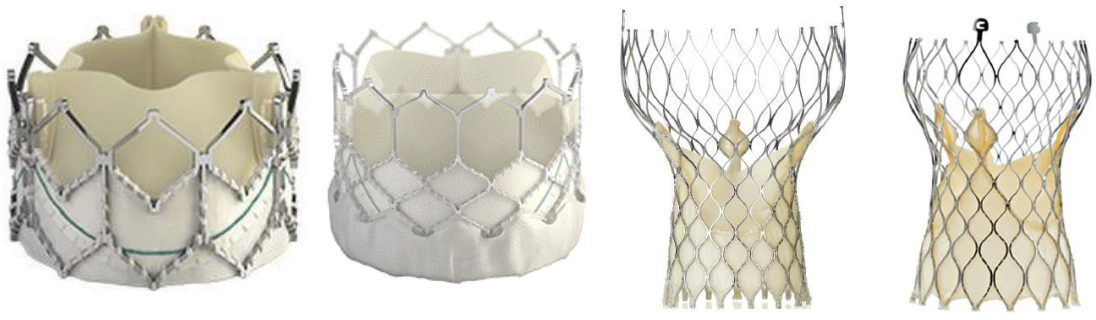

Figure 6: From left to right – Edwards Sapien XT THV, Edwards Sapien 3 THV, Medtronic CoreValve, Medtronic CoreValve Evolut-R

The other FDA approved valves are the self-expanding Medtronic CoreValve and CoreValve Evolute®. They make use of treated porcine pericardial tissue as leaflets and sealing skirts. The leaflets and skirts are individually cut and sutured to each other before they are sutured

to the inside of a self-expanding stent which is made from Nitinol and is intended to have high radial force at the inflow region and lower radial force at the outflow region while maintaining high hoop strength in the leaflet region. The pericardial skirt is cut to follow the struts of the bottom row (see Figure 6). The CoreValve Evolut-R valve replacement system is the second iteration and is designed to be repositionable to facilitate precise positioning as well as have an extended skirt and improved stent design to reduce the possibility of PVR (Iqbal & Serruys, 2014). This valve (see Figure 6) minimizes PVR by a conforming frame and a pericardial skirt. At 23 mm diameter, it has a height of 45 mm of which 12 mm from the bottom up is covered by a pericardial skirt. In 2017 the FDA approved the new CoreValve Evolut Pro® for the treatment of AS for symptomatic patients.

2.3. Complications post-TAVR

Potential postoperative complications such as stroke, renal failure, atrioventricular block ,and paravalvular regurgitation could arise after a TAVR procedure (Neragi-Miandoab & Michler, 2013). Of these complications, PVR (at varying degrees of severity) is a fairly frequent occurrence and the incidence post-TAVR has been reported to range from 50% to 85% (Lerakis et al., 2013).

According to the randomized multi-center PARTNER (Placement of Aortic Transcatheter Valves) trial, TAVR valves compare favorably to SAVR in terms of hemodynamic function, effective orifice area (EOA) and overall clinical outcome, but the incidence of moderate or severe PVR was more frequently observed after TAVR procedures, with PVR observed in 6.8% of cases in the TAVR group and only 1.9% of the SAVR group at the 1 year follow-up (Smith et al., 2011). It was observed during these trials that post-dilatation of TAVR valves decreased PVR and increased EOA.

At the advent of TAVR as therapy option, some regurgitation after the procedures was common and accepted. If it was graded as moderate or below, no further action would be taken, and the long-term effects might have been overshadowed by the relative improvement of the patient's condition. In a residual AR study, it was shown that patients with AR graded mild or greater has a 5-fold higher risk of death compared to patients that have no or trivial AR, 1-year post-TAVR (Lemos et al., 2012).

AR after a TAVR procedure can classically be divided into transvalvular regurgitation, (leakage through the valve itself), and paravalvular regurgitation. Paravalvular leakage or regurgitation (PVL/PVR) (also known as para-aortic regurgitation (PAR)) after TAVR occurs

due to incomplete circumferential apposition of the stented prosthesis relative to the native annulus (J. M. Sinning et al., 2013) and can be defined as leakage between the prosthesis and the wall of the conduit it is placed in. The irregular surrounding anatomy can be investigated in full detail with the help of imaging modalities such as transthoracic echocardiography (TTE) and multi-slice computed tomography (MSCT) before a TAVR procedure takes place. Irregularities can be due to calcification or annulus eccentricities. Recently, a third form of AR has been observed in some case reports using the Sapien XT and is termed supra-skirtal where the leakage is due to device design coupled with inferior implantation (Stähli et al., 2013) (see Figure 7). Leakage in the latter form occurs through the uncovered areas on the prostheses.

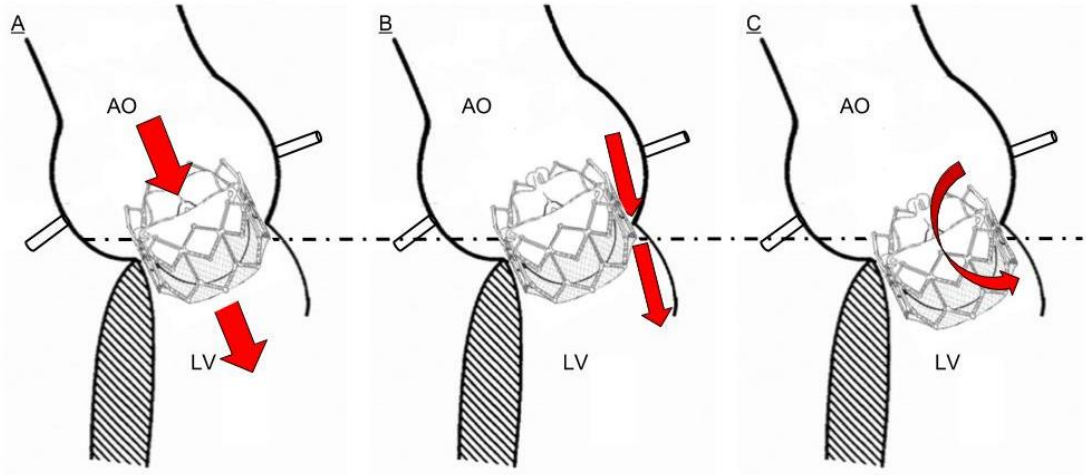

*Figure 7: Mechanisms of Aortic Regurgitation post-TAVR. (**A**) Transvalvular regurgitation, (**B**) Paravalvular regurgitation, (**C**) Supra-skirtal regurgitation. AO – Ascending Aorta, LV – Left Ventricle*

Prosthetic AR is a phenomenon which is dependent on many factors that cannot rely on a single measurement but should rather follow an integrated multi-parametric approach to successfully assess its severity and location (Zamorano et al., 2011). To fully grasp the mechanism which causes post-procedural AR and more specifically PVR, several anatomical and procedural factors in conjunction with methods of quantification should be considered.

2.4. Quantification of PVR

To standardize the measure of valvular regurgitation, the American Society of Echocardiography (ASE) has set recommendations for the grading of severity for native valvular regurgitation using two-dimensional and Doppler echocardiography. These recommendations have been used over the years and form the basis for the assessment of

valvular regurgitation, be it native or prosthetic. The graduation of PVR is one of the most challenging problems in the field of valvular disease because certain parameters overlap, and the severity of regurgitation depends on the hemodynamic condition of the patient. The conclusion was to graduate the severity in 3 tiers as mild, moderate or severe, leaving room for the mild to moderate, moderate to severe and trace categories where overlap or indetermination was evident (W. Zoghbi, 2003).

Quantification of native AR, which ultimately forms the basis for severity assessment of prosthetic valvular regurgitation, should employ an integrative process using several parameters to quantify valve function. For example, color flow Doppler can be used to visualize and assess the area of the regurgitant jet which can loosely be correlated to AR. It is important to note that it can only be used as a practical visual assessment and is dependent on the pressure gradient across the valve as well as inter-observer variability.

The vena contracta width is a measure of the smallest flow diameter in the plane of the LVOT and an estimation of the effective regurgitant orifice area (EROA). Shape and number of orifices influence the measured values and widths of <3 mm usually correlate to mild AR whilst widths of >6 mm is indicative of severe AR (W. A. Zoghbi et al., 2009).

The flow convergence or PISA (proximal isovelocity surface area) method is a quantitative method that employs the principle of conservation of mass and color flow Doppler to equate flow rate across the regurgitant orifice to flow rate across a convergence zone which can be used to calculate the EROA.

Aortic diastolic flow reversal is a normal observation and is usually measured in the upper descending aorta. It can be measured by pulsed wave (PW) Doppler from a suprasternal view and duration and velocity of the reversal can be directly correlated to aortic regurgitation. Other quantities that can be ascertained from PW Doppler to help characterize aortic regurgitation are the flow calculations, yielding values for regurgitation volume and EROA. Severe AR correlates to values ≥ 60 ml for regurgitant volume and ≥ 30cm^2 for the EROA (W. A. Zoghbi et al., 2009).

With prosthetic valve AR, the recommended integrative method for native valve regurgitation can be followed with certain conditional modifications. For example, the ratio of jet diameter to LVOT as measured by color Doppler is more applicable when looking at transvalvular regurgitations of the prosthetic valve. TTE is widely used within the field of cardiology and is useful when identifying the occurrence of transvalvular and paravalvular leakage. It is the most common approach in diagnostic cardiac ultrasound and the parasternal long and short axis views together with the apical and 5-chamber views are used for the detection of

regurgitating lesions. Measuring the vena contracta as a parameter for AR severity in the presence of a prosthetic valve can be challenging due to acoustic shadowing of the metal stent.

Another measure, namely the circumferential extent of the regurgitant jet, is measured by evaluating the jet in the short axis view at the level just below the stent. This value can specifically be correlated to paravalvular regurgitation and if the jet is <10% of the circumference of the stent it suggests mild PVR, between 10-20% it suggests moderate PVR and >20% it suggests severe PVR (see Table 1). Transesophageal echocardiography (TEE) can also be used and usually helps delineate the mechanism of aortic regurgitation (W. A. Zoghbi et al., 2009). The circumferential extent of PVR jets is measured by looking at the entire valve circumference from the trans-gastric view, using known landmarks like the left atrial appendage and assessing visually the number of paravalvular jets present and assigning them to corresponding minutes on the face of a clock. This is then divided by 60minutes and expressed as a percentage which has been correlated to PVR severity. Due to the plane that the valve is in or the diseased state of the patient, obtaining short axis and face views of the valve might prove challenging in the aortic position. Different echocardiographic views should be attempted to obtain the required face view.

The Valve Academic Research Consortium documents (VARC-1 and VARC-2) that have been compiled in recent years, were devised to serve as practical tools that help define standardized endpoints for TAVR and quantify potential complications that can arise post-operatively (Leon et al., 2011).

According to these updated standards, quantitative and semi-quantitative assessment parameters for the evaluation of AR post-TAVR should be ascertained with Doppler echocardiography. A clear distinction should be made between transvalvular and paravalvular AR and values for prosthetic regurgitant volume, EROA and regurgitant fraction should be collected where possible. AR can be graduated per the VARC-2 consensus documents into 1) none or trace, 2) mild, 3) moderate and 4) severe. Specifically, PVR is deemed mild if the circumferential extent of the regurgitation is <10%, moderate for values between 10-29% and severe for anything over 30% (Kappetein et al., 2012) (see Table 1). It was found however that in the PARTNER II trial, by mostly using the circumferential extent criteria, the severity of PVR was overestimated in one of the patient cohorts (Hahn, Pibarot, Weissman, Rodriguez, & Jaber, 2015).

Table 1: VARC-2 guidelines for prosthetic valve regurgitation with one row showing the ASE guidelines for circumferential extent. CE – Circumferential extent

	Mild	Moderate	Severe
Semi-quantitative parameters			
Diastolic flow reversal in descending aorta	Absent or brief early diastolic	Intermediate	Prominent holodiastolic
CE of prosthetic valve PVR (%) (VARC)	<10%	10-29%	≥30%
CE of prosthetic valve PVR (%) (ASE)	<10%	10-20%	>20%
Quantitative parameters			
Regurgitant volume (ml/beat)	<30ml	30-59ml	≥60ml
Regurgitant fraction (%)	<30%	30-49%	≥50%
EROA (cm^2)	0.10cm^2	0.1-0.29 cm^2	≥0.30 cm^2

As seen in Table 1, the ASE and VARC-2 guidelines differ in their ranges for circumferential extent of prosthetic valve regurgitation. Using the ASE guidelines and weighting the circumferential extent of the regurgitant jet more heavily than other parameters has been the source of some disparity when it comes to the graduation of PVR.

For example, a study presented at Transcatheter Cardiovascular Therapeutics (TCT) 2016, scrutinized the accuracy of using circumferential extent as a semi-quantitative assessment of PVR by recreating patient-specific anatomies using CT images. Applying differing amounts of PVR within the patient-specific valve models and correlating regurgitant fraction with circumferential extent showed discrepancies. The four models showed regurgitant volumes of 8.4, 19.0, 38.0 and 55.3 ml/beat, while the circumferential extent was measured as 13, 16, 32 and 48% respectively. Using the VARC guidelines, the correlated values did not reconcile and it was concluded that using the circumferential extent as a measure for PVR tends to overestimate the severity of PVR post-TAVR (Vahidkhah & Azadani, 2016).

These semi-quantitative parameters used to grade the severity of AR/PVR given in the VARC/VARC-2 documents are derived from the assessment of native aortic valve regurgitation with slight adjustments with regards to jet descriptions. End-point definitions and their cut-offs present certain limitations as acknowledged by the authors (Leon et al., 2011) and should be taken in the light that longer-term data in recent years is changing the understanding of the reason behind, and effect of PVR.

Another scoring system that is used to grade the severity of AR uses angiographic measurements, in which the 4-tiered graduation of the aortic regurgitation is based on the concentration of contrast medium in the left ventricle (during diastole) and visualized as opacification of the ventricle. This method grades the AR as: 0) no regurgitation, 1) traces of contrast medium is visible in the LV but is cleared during systole, 2) contrast fills the entire LV with less density as compared with opacification of the ascending aorta 3) contrast visible in the entire left ventricle during diastole is equivalent in density to contrast in the ascending aorta as measured by opacification and 4) contrast fills the entire LV with the first beat and the density compared with the contrast opacification of the ascending aorta is greater (Sellers, Levy, Amplatz, & Lillehei, 1964). It has been shown that the Seller's method of quantification is visually subjective and there exists a range in the amount of regurgitation, and an overlap between the grades (Michel, Vahanian, Besnainou, & Acar, 1987). Other factors that should be considered when evaluating angiographic measurements are the volume of contrast medium injected and the type and position of the catheter tip. It must also be noted that this method has not been validated for post-TAVR assessment of AR since multiple jets, a common characteristic of PVR, can influence the perceived density of the contrast medium and so skew the graduation.

Recently, in a study with 146 patients who underwent TAVR with a Medtronic CoreValve, a new hemodynamic measure, the aortic regurgitation index (AR index), was defined and correlated to the severity of paravalvular regurgitation. The measure is defined as:

$$AR\ index = \frac{(DBP - LVEDP)}{SBP} \times 100 \qquad (1)$$

where DBP is the diastolic blood pressure in the aorta, LVEDP the left ventricular end-diastolic pressure and SBP the systolic blood pressure. The gradient between DBP and LVEDP was found to decrease with increasing severity of PVR as measured by echocardiography (see Figure 8), complying with the VARC defined criteria. Patients with an index value of <25 had a 46% increase in 1-year mortality risk compared to a 16.7% increase for patients with an AR index ≥25 (J.-M. Sinning et al., 2012). It must be noted that overlap between graduations does exist and the AR-index does not discriminate between paravalvular or transvalvular regurgitation.

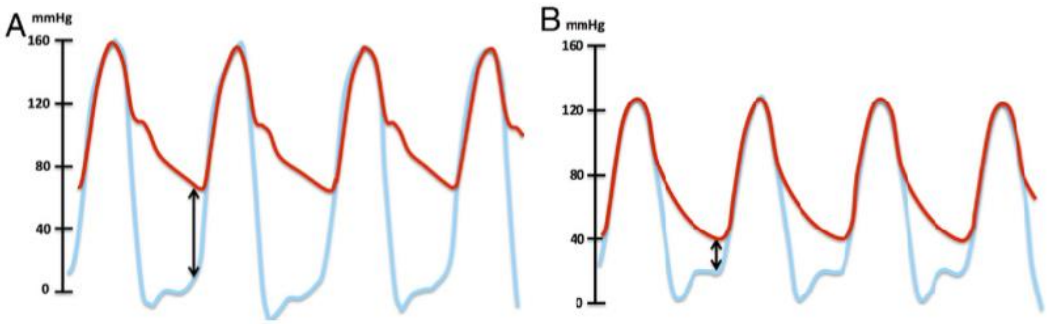

Figure 8: Calculation of AR index. A. Patient without PVR, B. Patient with moderate PVR

It is important to assess AR directly after the procedure to determine what potential additional procedures should be done in severe cases AR. Another hemodynamic assessment method which calculates the diastolic pressure-time (DPT) index after deployment has been proposed. The DPT-index is calculated by dividing the area between the aortic and left ventricular pressure-time curves by the duration of diastole (see Figure 9)

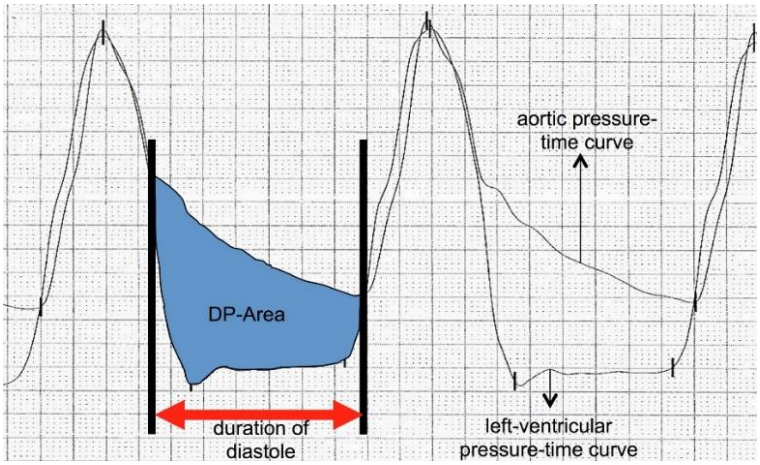

Figure 9: Calculation of DPT index

In a study including 362 patients, it was shown that patients with angiographically non-relevant AR (grade <2, graduated per the Seller's criteria) had higher DPT-index values compared to patients who had relevant AR. A DPT-index ≤27.9 was associated with higher 1-year mortality risk (Höllriegel et al., 2016).

A unifying grading scheme has been proposed to replace and expand on the three and four-tiered systems (see Table 2). Further, separating the mild category into mild and mild-to-moderate and the moderate category into moderate and moderate-to-severe will allow for more accurate graduation and characterization of PVR. The reasoning behind expanding the grading scheme is to prevent the operator from having to choose the middle option if there is any doubt between the grades. All the different modalities used to identify and quantify PVR have their own drawbacks and limitations and once again it is shown that when

assessing the severity of PVR, a multi-window, multi-parametric, integrative method is needed (Pibarot, Hahn, Weissman, & Monaghan, 2015).

Table 2: Proposed 5-class unifying grading scheme. (Pibarot et al, 2015)

Scheme, modalities, parameters and criteria for grading the severity of PVR						
3-class grading scheme	**Trace**	**Mild**	**Mild**	**Moderate**	**Moderate**	**Severe**
4-class grading scheme	**1**	**1**	**2**	**2**	**3**	**4**
Unifying 5-class grading scheme	**Trace**	**Mild**	**Mild-to-moderate**	**Moderate**	**Moderate-to-Severe**	**Severe**
Cineangiography	Grade 1	Grade 1	Grade 1	Grade 2	Grade 3	Grade 4
Invasive Hemodynamics						
Aortic regurgitation index	>25	>25	>25	10-25	10-25	**<10**
Doppler Echocardiography - Structural parameters						
Valve Stent	Usually normal	Usually normal	Normal/ Abnormal	Normal/ Abnormal	Usually Abnormal	Usually Abnormal
LV size	Normal	Normal	Normal	Normal/mildly dilated	Mildly/ moderately dilated	Moderately/ severely dilated
Doppler parameters (qualitative or semiquantitative) – Jet Features						
Extensive/wide jet origin	Absent	Absent	Absent	Present	Present	Present
Multiple jets	Possible	Possible	Often present	Often present	Usually present	Usually present
Jet path visible along stent	Absent	Absent	Possible	Often present	Usually present	Present
Proximal flow convergence visible	Absent	Absent	Absent	Possible	Often Present	Often Present
VC width (mm): colour Doppler	<2	<2	2-4	4-5	5-6	>6
VC area (mm^2):2D/3D colour Doppler	<5	5-10	10-20	20-30	30-40	>40
Jet Width at its origin (%LVOT diameter)	Narrow (<5)	Narrow (5-15)	Intermediate (15-30)	Intermediate (30-45)	Large (45-60)	Large (>60)
Jet density (CW Doppler)	Incomplete or faint	Incomplete or faint	Variable	Dense	Dense	Dense
Jet deceleration rate (PHT, ms): CW Doppler	Slow (>500)	Slow (>500)	Slow (>500)	Variable (200-500)	Variable (200-500)	Steep (<200)
Diastolic flow reversal: PW Doppler	Absent	Absent/ brief	Intermediate	Intermediate	Holodiastolic	Holodiastolic
Circumferential extent	<10	<10	10-20	20-30	>30	>30
Doppler Parameters (quantitative)						
Regurgitant Volume (ml/beat)	<15	<15	15-30	30-45	45-60	>60
Regurgitant fraction (%)	<15	<15	15-30	30-40	40-50	>50
Effective regurgitant orifice area (mm2)	<5	<5	5-10	10-20	20-30	>30
Cardiac magnetic resonance imaging						
Regurgitant fraction (%)	<10	<10	10-20	20-30	20-30	>30
	<15	<15	15-25	15-25	25-50	>50

A study assessing the discordance between different methods to determine the incidence and severity of PVR was done by re-evaluating 100 studies from the PARTNER IIB cohort. The studies were assessed by the original core laboratory personnel using their original

methods coupled with a more granulated 7-class grading scheme. The studies were also evaluated by a consortium of echocardiographers from the core laboratory using a multi-parametric approach coupled with the 7-class grading scheme. The core original PARTNER IIB laboratory personal more frequently reported PVR as being moderate and severe (compared to the consortium). Overall, relying heavily on the circumferential extent parameter as it is defined in the ASE guidelines leads to an overestimation of PVR incidence (Hahn et al., 2015).

2.5. Anatomical factors

The anatomy of the aortic complex plays a key role in pre-procedural planning and certain measured values can act as predictors of PVR. When a patient is deemed suitable for TAVR, anatomical factors such as accurate sizing of the annulus, angle of the LVOT and calcification extent and distribution should be investigated to reduce risk factors and improve patient-prosthesis matching (Wilczek, Bujak, Reguła, Chodór, & Osadnik, 2015).

Annulus measurement, accurate patient-prosthesis matching, and choice of measurement method are all crucial prior to any TAVR procedure to help reduce the occurrence of PVR. Two-dimensional techniques such as TEE, that tend to underestimate the annular size, are not sufficient for accurate quantification. Three-dimensional techniques such as MSCT, cardiovascular magnetic resonance (CMR) and 3D echo are considered the standard as they allow for accurate measurements of the aortic root at any level. These 3D techniques could help improve size selection for TAVR procedures.

Causes of AR related to anatomy and prostheses-anatomy interaction were investigated in a study that divided the relevant anatomical structures into three quadrants using MSCT. PVR was more common at the aorto-mitral fibrous continuity and the inside curve of the LVOT/ascending aorta when assessed from multiple views (using TEE) after implantation of a Medtronic CoreValve (C. J. Schultz et al., 2011).

The aortic annulus, which is usually depicted as a ring-like structure has been shown to be ovoid in nature by 3D techniques like CMR and MSCT (Burman, Keegan, & Kilner, 2008; Carl J. Schultz et al., 2010). These findings gave rise to the definition of an annulus eccentricity index (using CT) which can be defined as:

$$Eccentricity\ index = 1 - \left(\frac{\text{Sagittal diameter}}{\text{Coronal diameter}}\right) \quad (2)$$

where the two diameters are orthogonal to each other and correlate to the maximal and minimal diameters of the annulus. The prostheses are only regarded as circular if the index value is <0.1 (Delgado et al., 2010).

The often-elliptical nature of the aortic annulus during the cardiac cycle, as measured by MSCT (Hamdan et al., 2012), contrast with the cylindrical shape of the prostheses and can lead to an incongruent articulation between the prosthetic valve and the aortic complex and promote post procedural incidence of PVR (Gotzmann, Lindstaedt, & Mugge, 2012).

The angle of the aortic annulus to the ascending aorta has also been found to be an independent predictor of PVR, after CoreValve implantation. A greater angle could affect the valve's ability to seal properly due to a change in the radial expansion force the stent is exerting (Sherif et al., 2010).

Aortic valve calcium (AVC) is a third anatomical factor that needs to be considered when TAVR is considered for patients with AS. The complex cellular responses which lead to the formation of microcalcifications and later nodules on the leaflet and surrounding anatomy has been the topic of many investigations. The disease process has been attributed to different cell responses including resident, circulating and bone marrow derived cells (Leopold, 2012).

Since the unpredictable calcification of the aortic complex leads to irregular surfaces and possible paravalvular voids forming after prostheses deployment, a calcification scoring system is deemed important and can act as a predictor for PVR. The calcified leaflets and annulus can create atypical and irregular multiple PVR jets that are difficult to quantify (see Figure 10). Relating the amounts of calcification present in the aortic complex to the post-procedural PVR needs some form of quantification or graduation of the calcium.

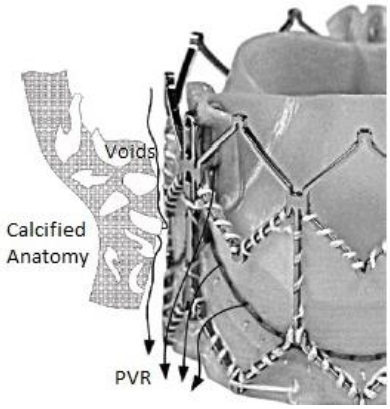

Figure 10: Schematic representation of PVR voids formed due to apposition caused by calcified anatomy

A system that was originally meant for coronary artery calcium (CAC) load determination has been adapted for use in grading the severity of aortic valve calcium by CT. In short, for the CAC score, the tomographic density measured in Hounsfield units (if bigger than 130units), coupled with a calcific lesion size of ≥1mm^2 is converted to a score for that particular lesion and a total coronary calcium score was obtained by adding all the scores for the lesions in the different slices taken by CT (Agatston et al., 1990). This is then adapted for the aortic valve and other structures within the heart to help clinicians diagnose the severity of calcification and potential adverse outcomes. Other scoring systems like the aortic volume and aortic mass scores have claimed better reproducibility than the Agatston score (AGs) because it is not multiplied by an abstract number (Callister et al., 1998; Hong et al., 2002).

TTE in the parasternal long and short axis view has been used to describe a semi-quantitative calcification scoring index (CSI) for total heart calcification which consists of the sum of the aortic root sclerosis, aortic valve sclerosis and mitral annulus calcification (Corciu et al., 2010). This CSI scoring index has been modified and expanded to include other relevant structures such as the STJ, aortic annulus and aortic valve commissures which are specifically relevant when looking at aortic regurgitation post-TAVR. The new system, called the TAVI echocardiographic calcification score (ECS) is the sum of the scores from the 3 aortic valve cusps and the commissures and has univariately been shown to be associated with the development of AR post-TAVR (Colli et al., 2011).

Studies investigating the effect of calcification on the incidence and severity of PVR, have however shown mixed results. Investigating device landing zone calcification, specifically for the CoreValve and its procedural success, a group has suggested a 4-step calcification scoring system called the device landing zone calcification score (DLZ-CS). It was measured against the Agatston score and both scoring systems showed to be positive correlations to PVR post TAVR. PVR was measured with angiography (John et al., 2010).

A study consisting of 152 patients correlated the annular eccentricity index as well as the cover index to the incidence of PVR post-TAVR. Patients underwent TTE after which post-procedural PVR was graded per the VARC-2 criteria. It was found that AV calcium score was the only independent predictor of mild or worse PVR (Fonseca et al., 2016).

Another study including 79 patients with severe aortic stenosis showed that the amounts and the locations of the calcification within the aortic valve are important, specifically the aortic wall calcium being the main determinant for PVR post-TAVR (Ewe et al., 2011). A CT study made to predict the effect of calcium on PVR after TAVR showed that protruding

annular calcium of greater than 4 mm was associated with moderate to severe PVL (Feuchtner et al., 2013).

To better understand the effect of calcification on the expansion of balloon expandable valve leaflets and stents, one should look at the calcification patterns that could lead to distortions of the prostheses due to increased stiffness of the native valve leaflets and surrounding anatomy (Sturla et al., 2016). In a finite element analysis (FEA) study, 3 differing calcification patterns along with their associated calcification levels were elucidated from explanted human leaflets and along with thickness measurements were converted into models. Even though the model was idealized with a circular annulus assumption, important results were obtained; showing that differing calcification patterns lead to varying local stent distortions after deployment of model valves. This, in turn, leads to imperfect stent apposition and the occurrence of voids that could potentially lead to paravalvular regurgitation.

Anatomical factors are important to consider for pre-procedural planning and accurate sizing, while procedural factors are important to ensure that the optimal results in terms of valve placement are obtained.

2.6. Procedural factors

The depth and angle of implantation play a key role in how well the valve coapts as well as the level of congruence between the prostheses and the wall of the aorta (see Figure 11). An FEA study, using the CT data from a clinical case of a CoreValve implantation, showed that depths and the angles at which the prostheses are placed has severe effects on the PVR that was predicted to occur (Morganti et al., 2016). The Snare technique, which utilizes a snare catheter, may be used to correct inferior or superior positioning of CoreValve prostheses. This technique, however, does not come without risk and should be seen as a bail-out option (Vavouranakis, Vrachatis, Toutouzas, Chrysohoou, & Stefanadis, 2010).

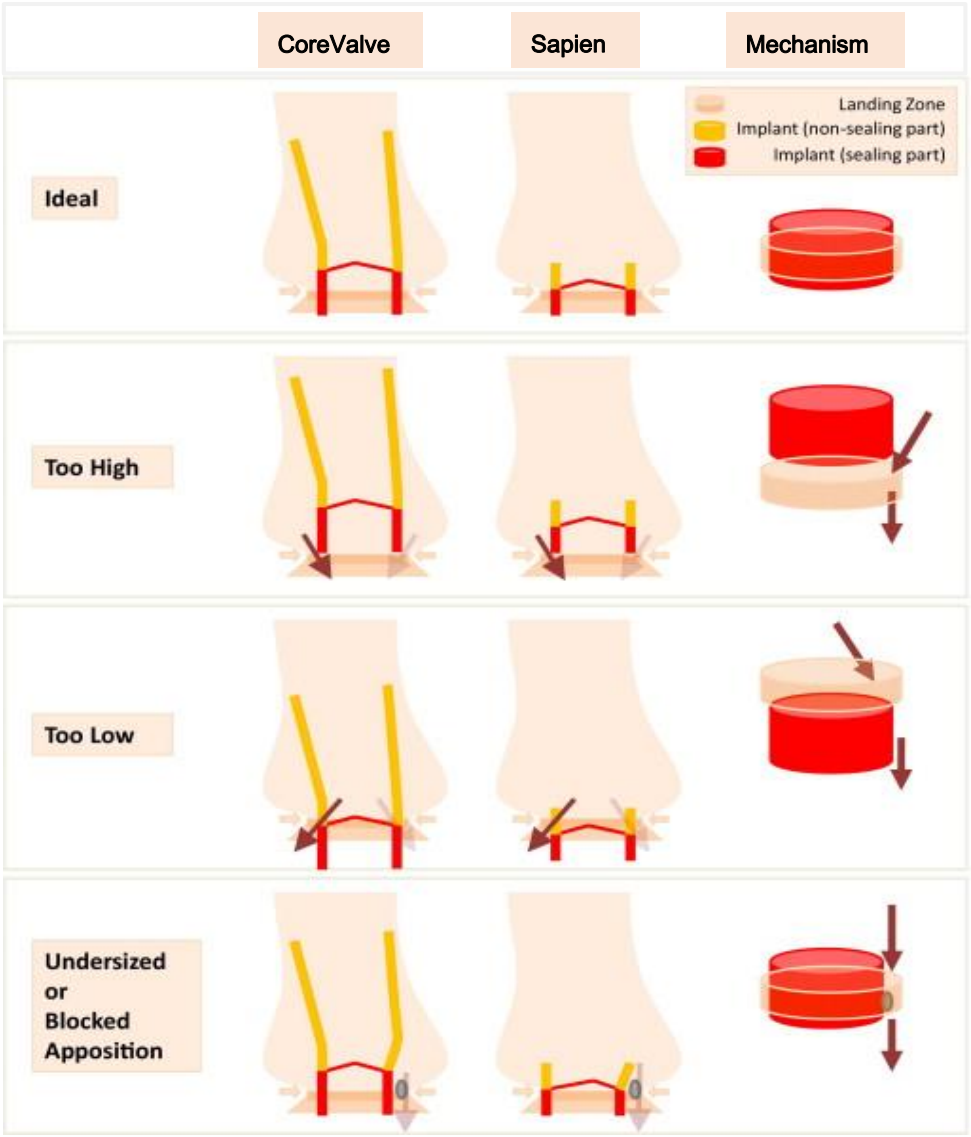

Figure 11: Different mechanism by which PVR can occur after placement of a THV

Furthermore, valve design and stent material influence the likelihood of post-TAVR AR from occurring. Most valves make use of a layer of PET fabric or treated pericardium sutured to the inside of the stent to function as a sealing skirt. The sealing efficacy of any sealing skirt relies on positioning of the prostheses and amount of calcium present around the valvular complex. From the French registry it was shown in a study which included 2769 patients who underwent TAVR and post-procedural TTE, that self-expanding (compared to balloon-expandable) devices, as well as the femoral delivery (compared to non-femoral) approaches were independent correlates of post-TAVR AR ≥ grade 2 (Van Belle et al., 2014). The multiparametric European and American guidelines and recommendations were followed when evaluating the severity of post-TAVR AR.

To assess the congruence between annulus and prosthesis, a cover index has been defined and is expressed as:

$$\left(\frac{Prosthesis\ diameter - TEE\ annulus\ diameter}{Prosthesis\ diameter}\right) x100 \quad (3)$$

A study with 74 patients showed a correlation between the cover index and the incidence of PVR graded ≥2 on a 4-class color Doppler grading system (Detaint et al., 2009). This finding suggests that a certain amount of oversizing might be needed to ensure good congruence between the prosthesis and the annulus.

Although there is always a percentage oversizing involved when choosing the correct valve for the size annulus under question, it could lead to dramatic and adverse outcomes such as annulus rupture. The opposite is also of course true where under-sizing can lead to valve embolization or severe paravalvular leaks forming (Messika-Zeitoun et al., 2010).

CMR can be used to more accurately and reproducibly quantify AR compared to the mostly qualitative nature of echocardiography (Myerson et al., 2012). In a comparative study, including 87 patients which underwent either TAVR or SAVR the semi-quantitative TTE underestimates post-procedural PVR when compared to quantitative CMR where there is no difference when looking at pre-procedural AR. In the TAVR group, TTE grading of PVR was different to CMR graded values in 52% of patients, and of these, 93% showed that TTE graded PVR at a lesser value than CMR. Ribeiro et al also showed that echocardiography underestimates the severity of PVR after TAVR as compared to CMR. (Ribeiro et al., 2014)

Moderate or severe PVR (grades 3 and 4) have clearly been shown to lead to an increase in morbidity and mortality rates, post-TAVR. Trace or mild PVR (grades 1 and 2) however have not received the same amount of attention. While investigating the thrombogenic potential of TAVR valves it was found that smaller simulated leakages (trivial PVR), led to higher shear rate damage of formed blood which is a governing factor when looking at TAVR thrombogenesis (Scotten & Siegel, 2014).

2.7. Incidence and prevention of PVR

Some valves minimize the occurrence of PVR by innovative stent and sealing skirt designs. Second generation valves can be defined as valves that have addressed the issue of PVR by having stent designs that better conform to the native anatomy with the help of orientating support arms or feelers, or being repositionable, which makes it possible to correct malpositioning of the prostheses if it occurred.

The St Jude Portico valve which is fully repositionable is believed to minimize PVR by the more open configuration of the stent. By having fewer incidences of struts resting against

calcific nodules, the valve better conforms to the native annulus and thus reduces the incidence of PVR (Tzikas, Chrissoheris, Halapas, & Spargias, 2014).

The Symetis Acurate TA valve (see Figure 12), which has CE-Mark since September 2011, consists of a porcine valve mounted within a self-expanding Nitinol frame with 3 stabilizing arms at the distal end of the device, which is meant for implantation in an intra-annular but sub-coronary position. A PET skirt sutured to the outer and inner part of the device, together with the hourglass shape of the stent helps to safely anchor the valve and seal against PVR (Huber, Wenaweser, Windecker, & Carrel, 2014). In a trial consisting of 40 patients from November 2009, it was seen that 59.0% of patients showed no or minimal paravalvular leakage while none exhibited severe PVR (Kempfert et al., 2011).

The Boston Scientific Lotus valve (see Figure 12) consists of three treated bovine pericardial leaflets which are mounted within a braided Nitinol stent and has an outer polyurethane skirt on the lower part of the device to prevent PVR. This adaptive sealing skirt (see Figure 13 **A**) is designed to occlude the interstices between the prosthesis and the calcified anatomy it is placed in by the puckering action of the skirt (Ian T. Meredith Am et al., 2014). At the 30-day follow-up of the REPRISE II study, it showed no or minimal PVR in 83.6% of the patients, mild in 15.5%, moderate in 1.0% of the patients and severe PVR in no patients (I. T. Meredith Am et al., 2014). This valve is also designed to be repositionable.

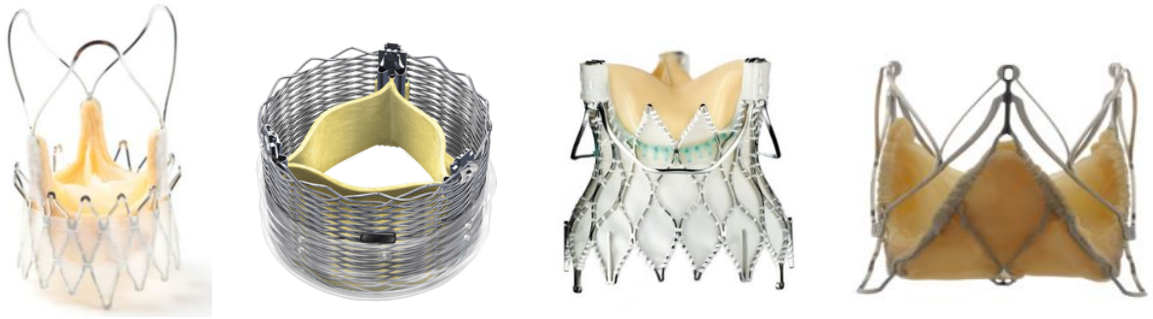

Figure 12: From left to right - Symetis Acurate TA, Boston Scientific Lotus Valve, Medtronic Engager, JenaValve

The Medtronic Engager™ aortic valve (see Figure 12) consists of three chemically treated bovine pericardial leaflets which are sewn to a polyester sleeve, which act as a sealing skirt. The leaflet-skirt combination is sutured inside a self-expanding Nitinol stent. The stent consists of a main stent body and a supporting frame. The valve is designed to be seated in the sinuses of Valsalva using the support arms which then leads to an anatomically orientated positioning and together with the shaped lower part of the stent (see Figure 13 **B**) gives the valve potential for better paravalvular sealing (Holzhey et al., 2013). In a 10-patient feasibility study, the valve showed no or minimal PVR in 90% of the patients while 10%

showed mild-to-moderate PVR (Sundermann et al., 2012). After the promising results of the feasibility study, a pivotal study was undertaken where 61 patients received the Engager. At the 6 month follow-up where 34 patients were successfully assessed it was shown that mild paravalvular leakage was present in 5% of the patients and none to trace was present in 82% (Sundermann et al., 2014). The Medtronic Engager bioprosthesis has however been discontinued.

The JenaValve (see Figure 12) consists of a chemically fixed porcine root attached to a self-expanding Nitinol stent with an outer pericardial skirt which is designed for sub-coronary implantation. The stent has a double bowed stent design and three feelers meant to be placed behind the native leaflets, anatomically aligning the prosthesis and securing a good seal. This is different from the radial force approach used by the previous generation Edwards Sapien XT and Medtronic CoreValve. The stent design also allows for repositioning and in a single cohort study has shown no device embolization (Nijenhuis et al., 2015). 86.4% of patients who were part of the multicenter CE-mark study in Germany showed no or minimal post procedural PVR, while no patients showed severe PVR (Treede et al., 2012). This ability to correctly align using extending arms and feelers combined with the native anatomy, have made JenaValve a candidate for use in patients with non-calcific natural aortic regurgitation. Even though the aortic root might be dilated, making the etiologies of PVR completely different from stenotic patients, the lesser amounts of calcium could lead to a decrease in PVR (Roy, Sharma, & Brecker, 2013).

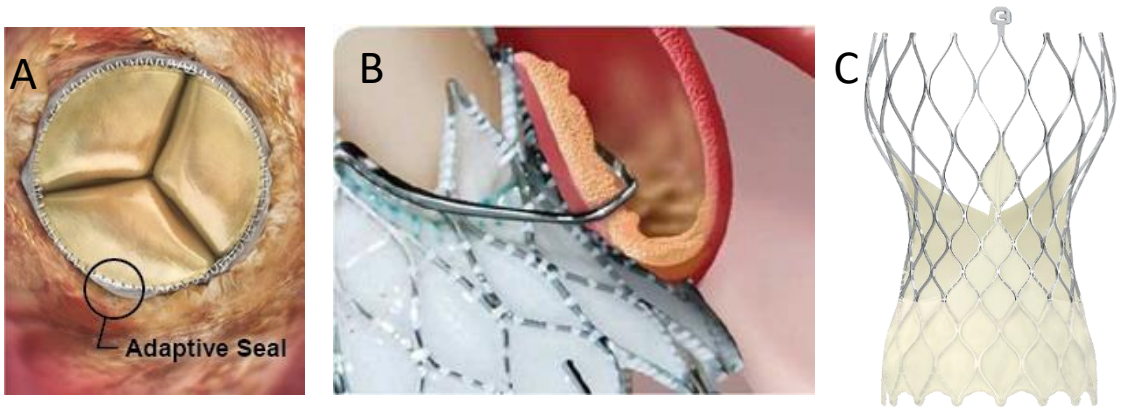

*Figure 13: Images of (**A**) Boston Scientific Lotus Valves' Adaptive seal as seen from the ventricle (**B**) Medtronic Engager – showing positioning arm and stent shape and (**C**) CoreValve Evolut Pro having a second wrap of pericardium on the outside of the stent.*

The Edwards Sapien 3 valve has an improved outer PET skirt design (see Figure 6) which acts as a parachute and bulges outward, thereby, closing the paravalvular voids that might have formed (Binder et al., 2013). This new concept can reduce the occurrence and severity of PVR if positioned under the annulus (Schymik et al., 2015).

Recently, Medtronic has developed the CoreValve Evolut Pro which also has an improved dual-layered sealing skirt similar to the concept of the Sapien 3. It now has a second wrap of porcine pericardium which is attached to the outside of the stent from the bottom up, halfway to the commissures (see Figure 13 **C**). The Evolut Pro's new skirt design is slightly above the nadir of the leaflets, increasing the surface area contact between the valve and the anatomy, improving the sealing performance of the valve.

Most retrospective studies investigating PVR incidence focused at the Edwards Sapien XT and the Medtronic CoreValve, which is to be expected since they have been on the market the longest. Many groups use the well-known 4-tiered graduation system to define the severity of the post procedural PVR (see Table 3). Severe PVR is mostly reported as being uncommon, except in one study by *Anger et al* where it is reported as 19%. This group, however, has no graduation for none/trace, indicating different interpretations of the graduation scale. As can be seen from *Kempfert et al,* some groups combined graduations of PVR when reporting.

Table 3: Incidence of PVR post-TAVR

			Paravalvular regurgitation			
Valve	**Author & year**	**Number of patients**	**None/trace**	**Mild**	**Moderate**	**Severe**
Edwards Sapien XT	Yang et al (2016)	92	45.7%	41.3%	13%	0%
	Bocksch et al (2016)	102	58.8%	35.3%	5.9%	0%
Edwards Sapien 3	Yang et al (2016)	61	80.3%	16.4%	3.3%	0%
	Pibarot (2017)	1592	55.7%	32.6%	8.2%	0.5%
	Bocksch et al (2016)	107	50.5%	37.4%	12.1%	0%
	Wendt et al (2015)	46	71.7%	26.1%	2.2%	0%
CoreValve	Oh et al (2015)	409	69.7%	26.4%	3.7%	0.20%
	De Carlo et al (2013)	821	18%	60.8%	19.6%	1.6%
	Anger et al (2014)	100		63%	18%	19%
	Toggweiler et al (2015)	50	52%	38%	10%	0%
CoreValve Evolut R	Popma et al (2017)	227	62.6%	32.2%	5.3%	0%
Engager	Holzhey et al (2013)	39	82%	5%	0%	0%
JenaValve	Treede et al (2011)	73	47.4%	39%	13.6%	0%
	Seiffert et al (2014)	23	78.3%	22%	0%	0%
Lotus Valve	Meredith et al (2016)	120	80.9%	18%	1.1%	0%
	Rampat et al (2016)	228	75.8%	23%	0.4%	0%
Accurate TA	Kempfert et al (2011)	40	59%	33.3%	7.7%	0%
	Kempfert et al (2012)	40	96.7%		3.3%	0%

In 2013 the experimental TRISKELE polymer THV was described by University College London (UCL) and implanted into a sheep model. The valve is supported on a retrievable Nitinol wire stent with an expanded height of 30 mm at a diameter of 23 mm. The leaflets consist of dip-coated polyhedral oligomeric silsesquioxanes polycarbonate urethane (POSS-

PCU) nanocomposite, which has proved to have good mechanical and blood contact properties (Ghanbari, de Mel, & Seifalian, 2011). The skirt also consists of POSS-PCU film and can be divided into an inner and outer layer. The outer layer covers about two-thirds of the stent and can again be divided into a flat region and a chalice-shaped cuff region surrounding the entire stent. It is said that the chalice-shaped cuff having a peripheral free edge can adapt to the native anatomy and help with sealing. The flat portion of the sealing skirt, located on the inflow of the valve has diamond shaped fenestrations to minimize stress on the film during crimping and to aid with potential cell ingrowth (see Figure 14). The valve was hydrodynamically tested in a compliant root model with anatomically sized rubber leaflets against a CoreValve and an Edwards Sapien XT, showing reduced leakage volumes in most root sizes (Rahmani et al., 2016).

Figure 14: UCL TRISKELE polymer valve

Post-dilatation of the implanted valve (directly or after the procedure) using a dilatation balloon catheter is often used and was shown to reduce the PVR area by 70% (Daneault et al., 2013). Some concerns arise with the use of post-dilatation, since it increases the risk of transvalvular regurgitation, damage to the leaflets and atrioventricular block (Webb & Binder, 2012). An additional option to reduce PVR is to use cardiac pacing to decrease the effect of the insufficiency by shortening diastole. Temporary pacing, followed by permanent pacing seems to be a successful way to manage the effect of regurgitation in the short term (Ali, Salinger, Levisay, & Feldman, 2014).

Since most of the population that undergo TAVR procedures are already deemed inoperable, transcatheter PVR closure becomes an attractive option (Ruiz et al., 2011). Single or multiple vascular plugs, such as the Amplatzer™ range, which is the most widely used device of its sort in the USA and Europe, can be used to reduce the symptoms of PVR (see Figure 15). Even though these occluding devices were not initially invented for PVR closure, it was shown that the use of the Amplatzer Vascular Plug III has a 100% procedural

success rate in aortic PVR closure (Smolka et al., 2016). An in-vitro method to measure the hemodynamic efficiency and efficacy of the PVR sealing has been developed and makes use of a pulse duplicator and a silicone valve holder which has a semi-elliptical lumen cast into it, to simulate a paravalvular leak to be closed using the plugs (Burriesci, Peruzzo, Susin, Tarantini, & Colli, 2016). It was shown that the efficacy of the plugs may be dependent on the physiological conditions chosen for the tests, but it is one of the few studies that offer a model that simulates paravalvular regurgitation.

Figure 15: From left to right: Amplatzer Vascular Plug, Amplatzer Vascular Plug II, Amplatzer Vascular Plug III, Amplatzer Vascular Plug 4

2.8. In-vitro simulation of PVR

Prosthetic heart valves undergo extensive testing by valve manufacturers prior to validation and focus mainly on long term device durability, transvalvular leakage and hemodynamic flow characteristics. The long-term effects of PVR on patients appear to be associated with a negative clinical outcome and hence there is an unmet need for standardized in-vitro evaluation of PVR.

The sizes of paravalvular holes are estimated from the effective regurgitant orifice area. Hole sizes used to simulate paravalvular voids and different testing environments can be seen in Table 4. One reported method used to simulate paravalvular leaks in an in-vitro testing environment was to place a surgical (in this case a St Jude Medical prosthesis) valve in a mounting with an adjustable mechanism to set various leakage areas. And testing at pressures ranging from 80-120mmHg in a closed state system. Calibrations were done using a disk with 36 equally sized and spaced holes (Scotten & Siegel, 2014).

Another study, aiming to predict patient-specific outcomes prior to the operation, simulated the occurrence of paravalvular voids using FEA. Patient CT data, together with echocardiographic measurements for the anatomy, were used to predict the outcome of a TAVR procedure. Stent and calcium interactions, together with different scenarios for valve

placements lead to voids forming which could be measured (Morganti et al., 2016; Morganti et al., 2014).

Table 4: Reported sizes of simulated paravalvular voids

Author	Leak dimensions	Leak Geometry	Comment
Burriesci et al (2016)	12 mm^2	Semielliptical	Simulated with silicone ring
Scotten et al (2014)	9.05 mm^2 36x (0.55 x 0.457 mm)	Circular	Calibration apparatus
Morganti et al (2014)	4.1 mm^2 36.9 mm^2	Patient specific (natural)	FEA predicted (CT based)
Morganti et al (2016)	5.3, 6.8, 8.7, 12.9, 18.6 mm^2	Patient specific (natural)	FEA predicted (CT based)

The variety of methods used to quantify and predict the severity of PVR together with the timing of follow-ups with patients have made it difficult to grasp the true overall prevalence and effect of PVR. However, with the help of advanced imaging modalities, standardized graduation scales, various quantitative scoring systems, and simulated test environments, clinicians are starting to understand better the impact PVR has on patients.

2.9. Polyurethane as skirt material

The major material choices for sealing skirts and sewing cuffs of bio-prosthetic heart valves are (i) treated pericardial tissue, (ii) PET fabrics, (iii) polyurethane (PU) and (iv) expanded polytetrafluoroethylene (ePTFE), all of which have proven clinical success. With long term implants, the material requirements are stringent, and toughness, durability and fatigue resistance are deemed important properties.

Segmented PU's (SPU's), with their good mechanical and biocompatibility properties, have found applications in many devices such as pacemakers (Stokes & Cobian, 1982), drug-eluting stents (Seo & Na, 2014), and total artificial hearts and are often the preferred choice for use as a biomaterial.

SPU's consist of two distinct microphases, namely a crystalline hard segment (HS) and the other an elastomeric soft segment (SS). The HS is formed by a reaction of diisocyanate and short chain diols or diamines, in a process called chain extension, and acts as physical crosslinks between the elastomeric SS. The soft segment is formed by the reaction of

diisocyante with longer chain polyols, usually with molecular weights of 1000-3000 Daltons. Considerable research has gone into finding the correct balance between good mechanical properties and biostability. Broad ranges in properties are possible by changing the chemistry and molecular weight of soft segments as well as the composition ratios of HS to SS (Martin, Meijs, Gunatillake, McCarthy, & Renwick, 1997; Martin, Meijs, Gunatillake, Yozghatlian, & Renwick, 1999; Martin, Meijs, Renwick, Gunatillake, & McCarthy, 1996). A determining factor for biostability of SPU's is the choice of monomers used, but more specifically the soft segment.

Poly(ester)urethanes, for example, have excellent mechanical properties but were found to be susceptible to hydrolysis of the SS when used for long-term implants (Stokes, McVenes, & Anderson, 1995). This low hydrolytic stability was overcome to a large degree by using ether soft segments. Biomer®, a commercial poly(ether)urethane-urea from the 1960s with a composition based on Lycra® from Du Pont, was one of the first SPU's to have been used in blood-contacting applications. Several studies investigating the blood compatibility (Lelah, Lambrecht, Young, & Cooper, 1983) and surface modification (Okkema, Yu, & Cooper, 1991) of this material group was launched. It was however found after several years in use that these materials undergo degradation due to oxidation when implanted under stress (Limited, 1999). Other poly(ether)urethanes (PEU) including the well-known Pellethane® family has improved on the susceptibility to hydrolysis of its predecessor but was later found to be oxidatively unstable - degrading due to metal-ion oxidation (MIO) and environmental stress cracking (ESC) (Santerre, Woodhouse, Laroche, & Labow, 2005), the former being of considerable concern since most medical devices, especially TAVR valves, contain metal in some way. MIO can be defined as degradation that occurs due to the breakdown of hydrogen peroxide facilitated by metal ions such as cobalt which are released due to corrosion of metal parts (Stokes, Coury, & Urbanski, 1987; Stokes, Urbanski, & Upton, 1990) while ESC can be defined as degradation that occurs due to oxygen species produced in the body that interact with stressed (or unstressed) materials (Lysaght & Webster, 2010).

Continuing with soft segment variations, poly(carbonate)urethanes (PCU) were more recently designed and introduced to improve on the oxidative stability by replacing the susceptible ether linkages which were found to be where degradation occurred. PCU's were synthesized and showed to have better oxidative stability than PEU (Khan, Smith, Jones, Finch, & Cameron, 2005). Simulated in vitro test environments have been developed to test clinical feasibility of these materials under different conditions and chemical environments. ESC of PEU's and PCU's have been tested in a system comprising of glass wool and a solution of $H_2O_2/CoCl_2$ where strained samples were incubated at 37°C for periods of 7 - 98

days. This method was shown to be a reliable test to simulate in-vivo environmental stress cracking (Zhao, Casas-Bejar, Urbanski, & Stokes, 1995).

To improve the long term biostability of polyurethanes, polydimethylsiloxane (PDMS) was included either as a surface or bulk modification. Polysiloxanes were used until the 1960s as pacemaker lead insulation but were later replaced by the mechanically superior polyurethanes. The appropriate level of biocompatibility, the low modulus, high flexibility, and low toxicity made the incorporation of PDMS into a polyurethane backbone very attractive. The full replacement of the SS with PDMS however, could distort the balance between biocompatibility and mechanical properties. Incorporating low levels of PDMS has been found to increase the biostability of polyurethanes (Pinchuk, Martin, Esquivel, & Macgregor, 1988). Adding such a non-polar molecule into a polar urethane structure, however, showed microphase separation. It was found that by addition of a compatiblising macro-diol such as poly(hexamethylene)oxide (PHMO) helped to increase adhesion between microphases (Gunatillake, Meijs, McCarthy, & Adhikari, 2000). The partial replacement of the susceptible ether segments with silicone moieties have been shown to improve resistance to MIO. A study using a cobalt mandrel implanted into the dorsal subcutis of rabbits showed that 35 wt% of siloxane within the structure greatly improved resistance to MIO (Ward, Anderson, Ebert, McVenes, & Stokes, 2006).

CarboSil TSPCU is synthesized of methylene diphenyl diisocyanate and butanediol (MDI/BDO) as HS and a polycarbonate glycol and silicone diol as soft segment (SS). Specifically, in polycarbonate urethanes, hydrogen bonds can form between the amide group (-NH, urethane) as donor and the carbonyl groups (-C=O, urethane, carbonate) in the urethane and SS as proton acceptors (Yang et al., 2013). Hydrogen bonds form between hydrogen atoms and atoms which are highly electron negative (such as nitrogen, oxygen, and fluorine) and can be defined as a special case of dipole forces (Zhang, Hu, Chen, & Ji, 2010). Polyurethanes with their micro phase-segregated nature are known to form hydrogen bonds between hard segments as well as between the HS and the SS.

Many studies make use of accelerated testing at elevated temperatures to isolate certain degradation mechanisms of segmented polyurethanes. However, this method of predicting performance has been brought under scrutiny because at elevated temperatures some changes to the microstructure occur which does not happen *in-vivo* which could skew the results. The amount of water taken up at elevated temperatures has also been investigated and it was shown that water absorption increases with temperature. (Padsalgikar et al., 2015) This led to the revaluation of some current test methodologies and encouraged a

different approach when planning in-vitro experiments to test long term effects certain environments might have on the material and its properties.

A variety of *in-vitro* and *in-vivo* tests have been proposed to test the potential application of polyurethanes as a long-term implantable load bearing material. In summary, biomedical SPU's have seen great advances in terms of biostability in the past years. Iteratively changing the soft segments from polyester to polyether, through to polycarbonate with the inclusion of silicone, has yielded materials with improved biostability.

2.10. Electrospinning

Textile production techniques such as weaving and knitting are used to manufacture fabric structures from melt-drawn PET fibers that have found application in a myriad of medical devices including stent-grafts and heart valves. The crosslinking of collagenous tissue by chemical treatment with glutaraldehyde is used to produce pericardium for use as valve leaflets and sealing skirts. These materials structures are however limited to being attached to stents via a labor-intensive suturing process. Electrospinning is a well-established process by which micro- to nano-sized fibers are drawn from a polymer solution or melt with the help of an electrostatic field. Scaffolds produced via electrospinning have application potential in filtration, food, ultrasensitive sensors ,and tissue engineering industries (Ding, Wang, Wang, Yu, & Sun, 2010; Kriegel, Arecchi, Kit, McClements, & Weiss, 2008; Qin & Wang, 2006; Sill & von Recum, 2008). Within the cardiovascular field, electrospinning has many possible potential applications such as tissue engineering scaffolds for heart valves (Del Gaudio, Bianco, & Grigioni, 2008), small diameter vascular grafts (Bergmeister et al., 2013) and covered drug-eluting stents (C. H. Lee et al., 2014).

Since it is possible to spin thermoplastic materials such as polyurethanes, other methods of attachment to a stent become possible. Other advantages of these fibrous scaffolds are their large surface to volume ratio, good mechanical properties and inherent porosity and pore interconnectivity.

Electrospinning is performed by feeding polymer solution or melt through a needle in a controlled manner, usually using a syringe pump, while a charge is applied to the needle, charging the solution running through it. At a critical voltage, the surface tension of the solution is overcome and due to the potential gradient between the charged fluid and the collector, a continuous jet is ejected from a Taylor cone which then deposits as layers, forming a fibrous scaffold (see Figure 16). Parameters such as applied voltage, solution flow rate, and various solution properties all influence the resulting fibers and scaffold properties

(Feng, Meng, Xiao, Zhao, & Guo, 2011). Relative humidity and temperature also play a key role in the electrospinning process and can have unexpected effects on scaffold properties.

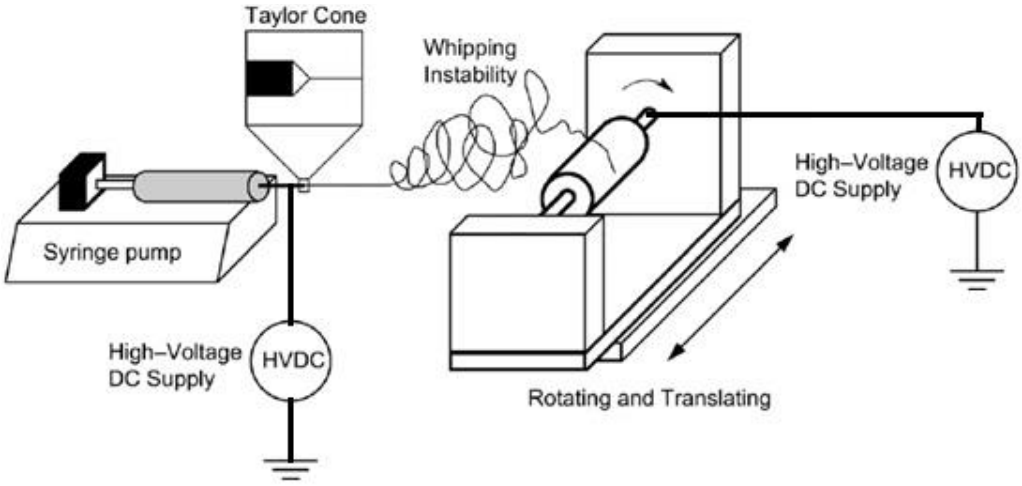

Figure 16: Schematic representation of an electrospinning setup to produce tubular scaffolds.

Critical voltages to overcome surface tension vary between polymers and solutions. Generally, it has been observed that with increased applied voltage, fiber diameter decreases due to increased jet elongation or multiple jets forming (Wang et al., 2013). Conversely, it has also been reported that initially, fiber diameter increases with applied voltage because of a reduced flight time of the fibers, where after further increase of voltage fiber diameters decrease (Mazoochi, Ahmadi, hamadnian, & Jabbari, 2012).

A balance should exist between the amount of solution present at the tip of the needle and the amount of solution being drawn due to electrospinning. Solution feed flow rate within a certain range has been seen to not affect fiber diameter to a great extent (Beachley & Wen, 2009). Various other groups, however, have reported that with increased flow rates, fiber diameter increases or ribbon-like (wet) fibers are observed due to incomplete solvent evaporation (Chowdhury & Stylios, 2010; Milleret, Simona, Neuenschwander, & Hall, 2011).

2.10.1. Solution parameters

Solution parameters such as conductivity, viscosity and solvent volatility all influence the resulting scaffold. Increasing the conductivity of the solution by using solvents with high dielectric constants may lower the required voltage needed to initiate electrospinning. In conjunction with this, using solvents with low volatility (high boiling point) may result in fibers landing wet (Mit-uppatham, Nithitanakul, & Supaphol, 2004) while using solvents with high volatility may results in irregular spinning due to the solution drying out at the tip of the needle. Investigating the effects of solution ratios on the electrospinning of polyurethane from N, N-dimethyl formamide (DMF) and tetrahydrofuran (THF) showed that increased THF

concentration leads to bigger fiber diameters compared to solutions where DMF is the most abundant solvent (Feng et al., 2011). Molecular weight and solution concentration greatly influence solution viscosity and the resultant fiber morphology. The molecular weight is an indication of chain entanglement and the general trend is that fiber diameter increases with increasing molecular weight (solution viscosity). Increased viscosity, however, can lead to the charge that initiates the process to be insufficient for successful fiber drawing or stretching. Tensile properties of electrospun polyvinyl alcohol scaffolds have been seen to increase with molecular weight (Ngadiman, Noordin, Idris, Shakir, & Kurniawan, 2015).

2.10.2. Environmental conditions

Environmental conditions can also have a profound effect on the outcome of fiber morphology and mechanical properties. Too high (>60%) or too low (<20%) relative humidity, per a study spinning with PEO/Alginate, can lead to a loss of 3-dimensionality and fluffiness in the scaffold (Bonino et al., 2012). Another effect that relative humidity can have is that fiber diameter can increase with increasing humidity as seen in a study using polyetherimide spun from NMP (Oğulata & İçoğlu, 2015). Fiber breakage, surface porosity and decreased fiber collection can also be a result of varying relative humidity's (5 - 75%) when spinning PEG, PCL, and PCU (Nezarati, Eifert, & Cosgriff-Hernandez, 2013a). These phenomena are dependent on the solvent choice and chemical nature of the polymers. The interaction between the environmental water in the air and the spinning process can have an influence on the solidification of fibers as they fly to the collector.

2.10.3. Throughput

One drawback of the single nozzle electrospinning process is low throughput. Initial attempts to increase the fiber throughput was done by using multiple nozzles, which works to a certain degree but has some limitations. Electric field disturbances and interference of the neighboring nozzles (Theron, Yarin, Zussman, & Kroll, 2005) can have effects on fiber and thickness uniformity of the scaffold which could lead to decreased effectivity within the application. Another method of increasing fiber throughput is by free surface electrospinning, which does not make use of nozzles, but rather by rotating drum-, disk- and ball fiber-generators within a polymer solution which leads to multiple jets forming when a high voltage is applied and so increases the amount of fibers deposited on the collector (Niu & Lin, 2012).

2.10.4. ECM resemblance

The resemblance of conventional electrospinning to the extracellular matrix (ECM) makes it an attractive candidate to be used in tissue engineering and regeneration applications. It does however only resemble the ECM in its fibrillary structure and not in the spatial characteristics (J. Wu & Hong, 2016). Collagen, taking up 30% of total protein weight within the ECM, is the most abundant protein and provides the tensile strength of the matrix and also helps regulate cell adhesion (Frantz, Stewart, & Weaver, 2010). Collagen fibrils with diameters of 30 - 100nm are packed together in cord shapes with diameters of 1 - 20um in the ordinary tissue of mammals (Ushiki, 2002). This introduces the drawback of traditionally (randomly) collected electrospun scaffolds having inherent pore-sizes that are too small and obstruct cell migration. Rounded cell sizes range from 5 - 20um and the pore dimensions within the scaffold will not allow proliferation or waste and nutrient diffusion (Sun et al., 2015). A statistical theory has been presented to correlate the specific surface area of a scaffold to the dimensions of the pores/voids found within the network. It was found that fiber geometries are a primary determinant for maximal pore dimensions and surface area. (i.e. pore sizes varies with fiber diameter) (Eichhorn & Sampson, 2010)

2.10.5. Pore size optimization

Initial attempts to solve the problem of the inherently small pores within the network was by altering the parameters of the spinning process to obtain larger fibers. Several studies show larger pores can be achieved with increased fiber diameters (Rnjak, Li, Maitz, Wise, & Weiss, 2009; Sisson, Zhang, Farach-Carson, Chase, & Rabolt, 2010). A further study shows that larger pore sizes obtained by larger fiber diameters, combined with lower packing density, have a positive influence on cell ingrowth and proliferation (Soliman et al., 2011). Work done on parameter optimization to increase porosity has shown that there exists a directly proportional relationship between solution concentration and fiber diameter. As fiber diameter increased from 0.18 – 1.4 µm the pore size also increased from 0.5 - 24.5 µm (Boland et al., 2005). Microfibers create large enough pores within the scaffold to allow for cell migration, proliferation, and waste and food management.

When considering fiber diameter and the enlarging effect it has on pore-sizes, increasing microfiber diameters from 3.4 - 12.1 µm led to incrementally increased cell (human venous myofibroblasts) infiltration within scaffolds as determined by fluorescent staining, microscopy, and image analysis (Balguid et al., 2009). Combining both micro and nanofibers in a bi-layered scaffold to make use of the increased pore-sizes produced by the microfibers as well as the resemblance of nanofibers to the ECM geometry, showed that pore sizes of

up to 45 μm^2 are attainable and that too thick nanofiber layers within the bi-layered structured showed reduced cellular infiltration (Pham, Sharma, & Mikos, 2006). Evidence has been provided that shows reduced cell adhesion and no proliferation in larger fiber diameters (7 µm) compared to smaller diameter fibers (0.3 um, 1.2 um) (Kwon, Kidoaki, & Matsuda, 2005).

An investigation into the effect of fiber diameter and surface roughness on blood activation of vascular grafts concluded that smaller fibers (<1 µm) lead to lower coagulation as compared to larger fibers (5um) (Milleret, Hefti, Hall, Vogel, & Eberli, 2012). In another experiment, stainless steel stents (3 mm x 12 mm) covered with polyurethane fibers were prepared by electrospinning, and it was shown that very little (0.2 mg/stent) urethane is needed to successfully prevent water leakage in a test apparatus with a water pressure of 44mmHg (Kuraishi et al., 2009).

Other methods to modify the porosity after electrospinning include, salt leaching (Nam, Huang, Agarwal, & Lannutti, 2007), co-electrospinning of sacrificial fibers or particles (Lavielle et al., 2013; Voorneveld, Oosthuysen, Franz, Zilla, & Bezuidenhout, 2016), addition of blowing agents (Kim & Kim, 2007), cryogenic electrospinning (Simonet, Schneider, Neuenschwander, & Stark, 2007) and ultra-sonication (J. B. Lee et al., 2011).

2.11. Project proposal

This project forms part of an ongoing research project on the development of TAVR valves. In particular, it is aimed at developing an improved sealing method for TAVR valves using electrospun polyurethane.

2.11.1. Aims

The object of this study was to design, manufacture, characterize and test the efficacy of an electrospun sealing skirt for a balloon expandable transcatheter heart valve. After considering the literature survey on the incidence and quantification of paravalvular regurgitation and other available sealing options, the following is proposed:

- Identify possible material for use in a sealing skirt.
- Determine suitable conditions for electrospinning CarboSil for use in skirt attachment and PVR studies.
    - Thoroughly characterize scaffolds with regards to fiber diameter, porosity, pore size, permeability, and mechanical properties.
- Develop and compare potential methods of attaching an electrospun scaffold to a balloon expandable TAVR stent.
    - Solvent bonding, heat bonding, laser bonding, ultrasonic bonding
    - Optimize polymer pre-coating for bond strength.
- Automize a successful bonding method.
- Quantify attachment strength.
    - Develop a mechanical test method using a tensile tester.
    - Use finite element analysis to support quantification.
    - Perform long term fatigue study.
- Manufacture different skirt designs with suitable bonding patterns for sealing against paravalvular regurgitation.
- Evaluate said designs in an in-vitro pulse duplicator model against a control to test sealing efficacy.

Potential novelty of this project includes a forward flow filling concept for use in heart valves specifically, as well as the use of electrospinning as a material for a sealing skirt for a transcatheter heart valve.

3. Electrospinning of scaffolds

This chapter describes the materials and methods used in the electrospinning of polyurethane scaffolds that are utilized in several sealing skirt concepts for use in TAVR valves. It will describe the iterative optimization steps followed to obtain usable scaffolds as well as investigate the effect certain parameters have on the resulting scaffolds. This will be followed by morphological and mechanical characterization of the scaffolds.

3.1. Experimental

3.1.1. Materials

Scaffolds were manufactured from CarboSil™ 20 80A, a biocompatible Thermoplastic-Silicone-Polycarbonate-urethane (TSPCU) copolymer with a 20% silicone content (DSM Biomedical, Heerlen, The Netherlands). The different batches evaluated in this study were labeled batch 1, batch 2 and batch 3 (see Table 5) and had weight average molecular weights (MW) of 295 509 Da, 340 997 Da and 449 147 Da respectively, as per the certificate of analysis (COA). The given range for the MW was 275 kDa – 500 kDa as per specifications.

Table 5: Weight average molecular weight and polydispersity of three batches of CarboSil 80A as per COA.

Batch	Weight average molecular weight (MW)	Polydispersity Index (PDI) (Mw/Mn)
1 (E059712)	296 kDa	1.8 Mw/Mn
2 (15030182)	341 kDa	2.3 Mw/Mn
3 (A010815)	449 kDa	2.2 Mw/Mn

Tetrahydrofuran (THF) and N, N Dimethylformamide (DMF) were purchased from Kimix chemicals (Cape Town, South Africa) and N, N Dimethylacetamide (DMAc) from Merck (Sigma-Aldrich) (Darmstadt, Germany).

3.1.2. Scaffold production

3.1.2.1. Preparation of spinning solutions

All solution concentrations used in the electrospinning of this project are expressed as mass-per-mass (wt%) concentrations. For example, a 16 wt% solution was made by adding 16 g CarboSil 80A to 42 g DMF and 42 g THF (1:1 ratio) and agitating in a roller oven at 40°C until fully dissolved (16 - 48 hours).

Prior to dissolution in some embodiments, the as-received virgin pellets were heat pressed (HP) between two PTFE coated Armalon sheets (Hi-Performance Products Inc., San Clemente, USA) at 200 °C and 20 MPa for 2 minutes by using a 10-ton hydraulic press. HP films were removed and left in air to cool to ambient conditions and were kept in a dry compartment to equilibrate for at least 24 hours prior to solution preparation. The compartment consisted of an aluminium frame with glass walls and drawers to house desiccant.

The viscosity of the solutions was measured using a RVDV-I Prime viscometer (Brookfield Engineering, Middleboro, USA), the Small Sample Adapter (16 ml) and the SC4-21 spindle. All viscosity measurements were done at 23.5°C ±0.5°C and 51.5% ±0.5% relative humidity.

3.1.2.2. Electrospinning

The electrospinning equipment (see Figure 17) was designed in-house and consists mainly of 3D printed parts, a Fusion 100 high precision syringe pump (Chemyx Inc. Stafford, USA – not indicated) and (**1**) two high voltage ES30P-5W (+) & ES30N-5W (-) power supplies (Gamma High Voltage Research, Ormond Beach, USA). (**2**) An aluminium collecting mandrel was inserted into (**3**) a rotational stage, mounted on (**4**) a XY-stage. Stepper motors used for rotation of the mandrel and translational movement in two perpendicular directions were controlled using an Arduino Mega 2560 (Arduino.cc), A4988 stepper motor controllers (Polulu Corporation, Las Vegas, USA) and the open source Arduino IDE software. An 18-gauge hypodermic needle with a blunt tip was placed through (**5**) a stainless-steel base plate (30 x 30 x 3 mm) connected to the positive high voltage power supply. For some control of environmental variations, the setup was placed inside (**6**) a melamine veneer coated wooden cabinet with glass doors equipped with (**7**) a humidifying/dehumidifying loop system.

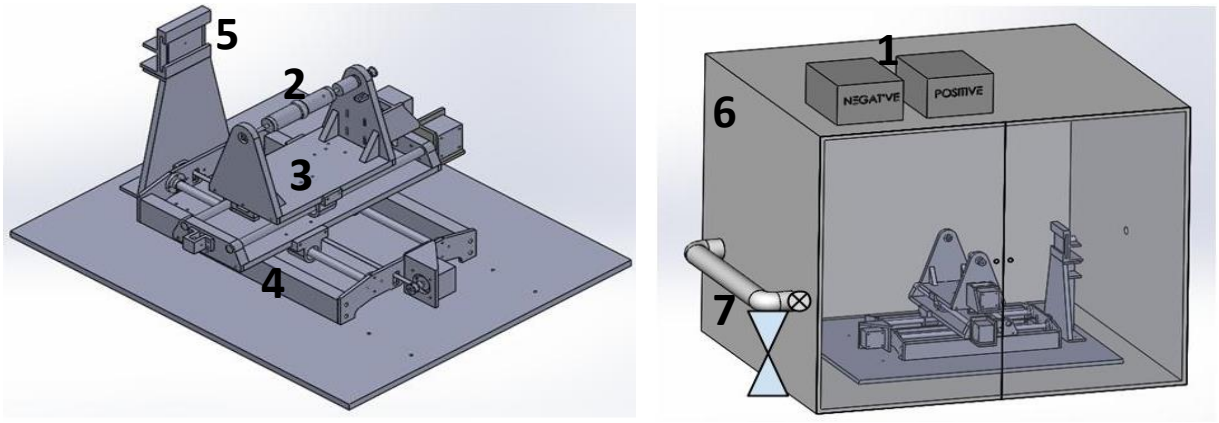

Figure 17: Electrospinning Setup

For dehumidification, the loop system (see Figure 18) contained desiccating silica gel crystals (water indicating) and a fan for air circulation. For humidification, an ultrasonic humidifier was attached to the loop. A relative humidity sensor allowed for the system to automatically be switched on and off to regulate conditions if humidity was too high (>45%) or too low (<35%).

Figure 18: Photograph of humidifying/dehumidifying loop attached to side of electrospinning enclosure

Two collecting mandrels were used in this study. An aluminium cylinder (see Figure 19 **A**), 23 mm in diameter was used to prepare samples for tensile and porosity measurements, FLAT skirts and flaps for the H-FFF skirt design (see Ch. 4). A cylinder with the same diameter of 23mm, including a pre-defined hump (see Figure 19 **B**) in the center, was used to prepare the material for the dual layered sealing skirts.

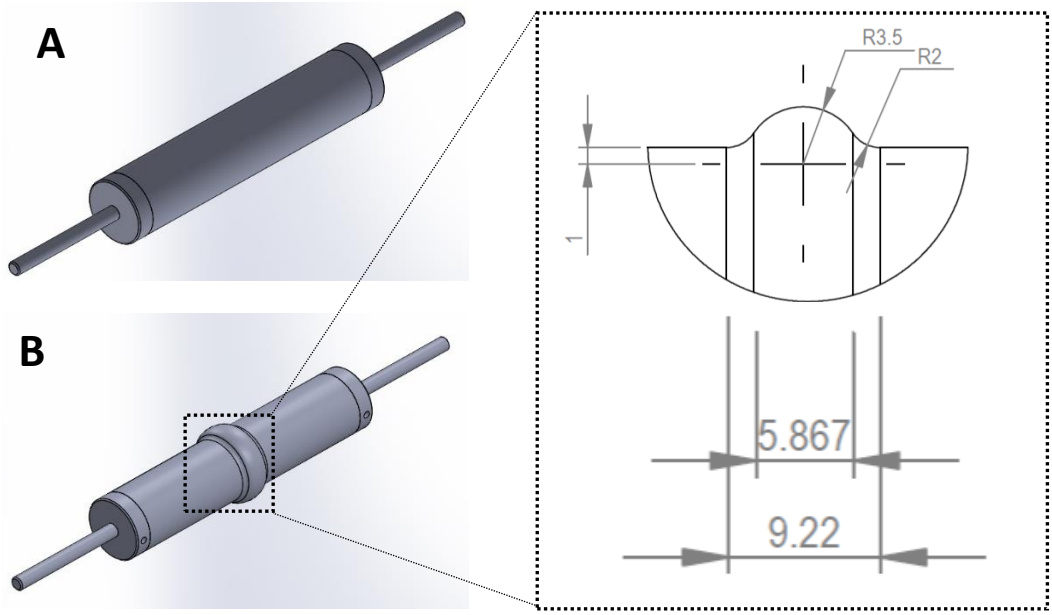

*Figure 19: Renderings of 23mm Electrospinning Mandrels: Flat (**A, top left**) and Humped (**B, bottom left**) with an engineer drawing showing the cross-sectional view of the hump and defining geometry (**right**)*

i. General spinning conditions

Scaffolds were fabricated at relative humidity's (RH) of 35 – 45%, unless stated differently. The rotational stage underwent a 74 mm oscillating motion at 3 mm/sec with a 3 second pause at the ends of the oscillating motion to allow for more even fiber deposition thickness across the collection mandrel.

After 50 minutes of spinning, final drying of the scaffold was achieved by placing the mandrel in a regular laboratory oven at 45°C for 90 minutes. The scaffold was trimmed on the mandrel (using a scalpel blade) and removed by rolling off with gloved hands.

The effect of feed flow rate, solution concentration and mandrel rotation speed on the resulting fiber diameter and scaffold tensile properties were evaluated.

ii. Effect of solution feed flow rate and concentration

Scaffolds were spun from 15, 20 and 25 wt% solutions (batch 1) at 2.5 and 4 ml/h (the 25 wt% solution was only spun at 2.5 ml/h) with 1500 rpm mandrel rotation speed. An applied voltage of +9 kV (base plate) and -1 kV (mandrel) were used together with a tip-to-collector distance of 230 mm.

iii. Effect of mandrel rotation speed

Scaffolds were spun from 15 wt% CarboSil 80A (batch 1) at rotation speeds of 600, 1500 and 3000 rpm. An applied voltage of +14 kV (base plate) and -1 kV (mandrel) were used together with 230 mm tip-to-collector distance and 2 ml/h solution feed flow rate. The experimental concept was repeated using CarboSil 80A (batch 3) to spin scaffolds from 16 wt% solution at 500, 1000 and 1500 rpm. Scaffolds were spun at an applied voltage of +13 kV (base plate) and -1kV (mandrel), 260 mm tip-to-collector distance and 2 ml/h feed flow rate.

Table 6: Summary table of parameters used in the optimization of electrospinning process, HP = Heat pressed

	Solution Conc. (wt%)	Feed flow (ml/h)	Rotation (rpm)	Tip-to-collector (mm)	Applied voltage (kV)	
					+	-
ii (Feed flow and Solution concentration)	15,20,25	2.5, 4	1500	230	9	1
iii (Rotation speed)	15	2	600, 1500, 3000	230	14	1
	16 (HP)	2	500, 1000, 1500	260	13	1

3.1.3. Material and scaffold characterization

3.1.3.1. FTIR - ATR of pre- and post- heat pressing

Infra-red (IR) spectra were obtained (pellets and HP films) using an Alpha FTIR spectrometer (Bruker, Billerica, USA) equipped with an attenuated total reflectance (ATR) module. After routine background scans, 16 scans were obtained from 400 – 4000 cm^{-1} per sample and the values averaged and displayed as transmission spectra.

3.1.3.2. Differential scanning calorimetry

Differential scanning calorimetry (DSC) was performed using a PerkinElmer DSC 4000 (PerkinElmer, Waltham, USA). Samples (pellets and HP film) weighing 15-20 mg were

heated from 30°C – 210°C at 10°C/min under a constant flow of dried nitrogen. Thermograms were analyzed using the Pyris software supplied with the instrument.

3.1.3.3. Scanning Electron Microscopy (SEM)

SEM samples fixed onto stub holders were sputter coated with gold for 120 seconds using a Polaron SC7640 sputtering unit (Quorom Technologies, East Grinstead, England). For fiber morphology visualization, a LEO 1450EP SEM (Zeiss, Oberkochen, Germany) was used at an operating voltage of 10 keV using the secondary electron detector.

3.1.3.4. Fiber diameter, alignment and pore sizes

Fiber diameter and alignment as well as pore sizes were quantified using FIJI (Schindelin et al., 2012) image analysis software. For fiber diameter analysis, a line was drawn across the diagonal of a SEM image and 10 intersecting fibers were manually measured (see Figure 20) to obtain the mean fiber diameter. Both luminal and abluminal sides were measured.

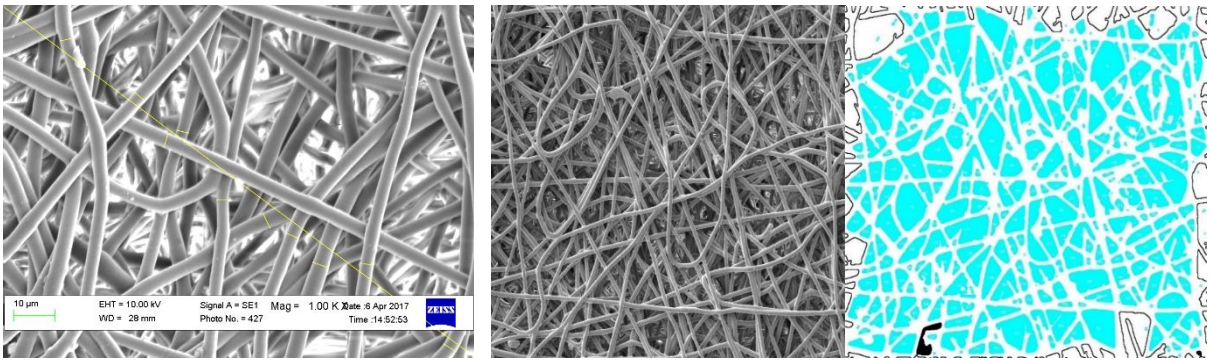

*Figure 20: SEM images used for scaffold morphology determination: 1000x magnification of scaffold, showing diagonal line and measured fibers (**left**), 500x magnification of scaffold with accompanying analyzed image showing identified pores in cyan (**right**)*

A FIJI macro was used to determine the pore sizes of the scaffold (both sides). Briefly, after thresholding of the image, the edges were identified and removed, after which pores were identified as areas between fibers (see Figure 20). This was a semi quantitative method of measuring and depended on the contrast of the image and how thresholding was done. Using the formula for the area of a circle, the equivalent pore diameter was calculated using the following formula:

$$Equavalent\ pore\ diameter = \sqrt{\frac{4\ Area}{\pi}} \qquad (1)$$

where $Area$ is calculated per identified pore by the macro.

Fiber alignment was determined by the Orientation J Measure plugin on FIJI (Fonck et al., 2009). It yielded a quantitative coherency value which corresponds to the amount of isotropy or anisotropy within a region of interest (see Figure 21). Coherency values range from 0 – 1 representing full isotropy and anisotropy. Briefly, to obtain an average coherency value for a sample, three images (200x magnification) per side of scaffold were analyzed using the entire image as the region of interest.

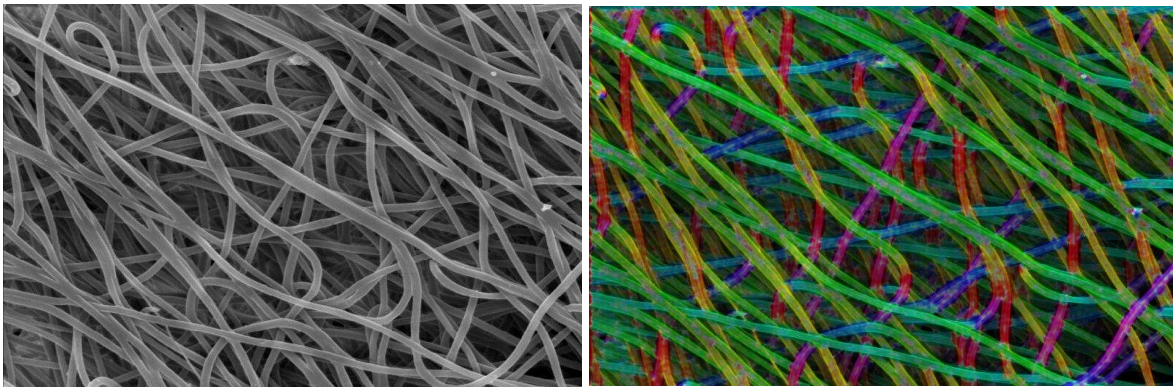

*Figure 21: SEM image (**left**) at 500x magnification with corresponding color survey (**right**) of the same image indicating orientation (hue) and coherency (saturation)*

We followed the optimization of the feed flow rate by determining the orientation of the fibers, or coherency, as influenced by solution concentration. Coherency is expressed by the terms isotropic and anisotropic. If the fiber orientation is evenly distributed in all directions the scaffold is said to be isotropic. In contrast, if the fiber orientation is not evenly distributed the scaffold is classified as anisotropic.

3.1.3.5. Thickness distribution

Scaffold thickness was measured using a Quick Mini digital thickness gauge (Mitutoyo Corporation, Kanagawa, Japan) with a resolution of 0.01 µm, at 5 points along the translational axis, to obtain a mean scaffold thickness (see Figure 22).

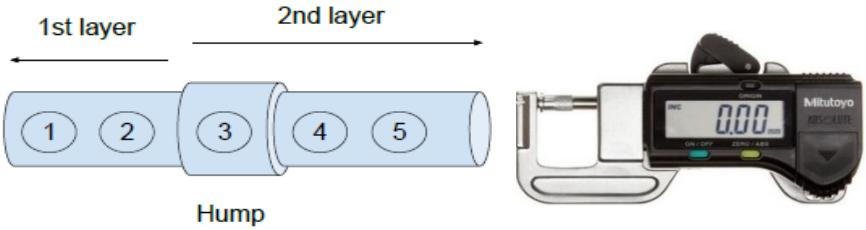

*Figure 22: Schematic of scaffold with representative points where thickness measurements were taken (**left**), image of Mititoyu Clip Gauge used for all thickness measurements (**right**)*

3.1.3.6. Mechanical properties of scaffolds

Uniaxial extension test to break was performed on 30 x 5 mm die cut samples (n =5) using an Instron 5544 (Instron, Norwood, MA) equipped with a 500 N load cell. Specimens were cut parallel (PARA) and perpendicular (PERP) to rotation direction (see Figure 23). Thickness was measured on 3 areas along the length of the specimen and recorded.

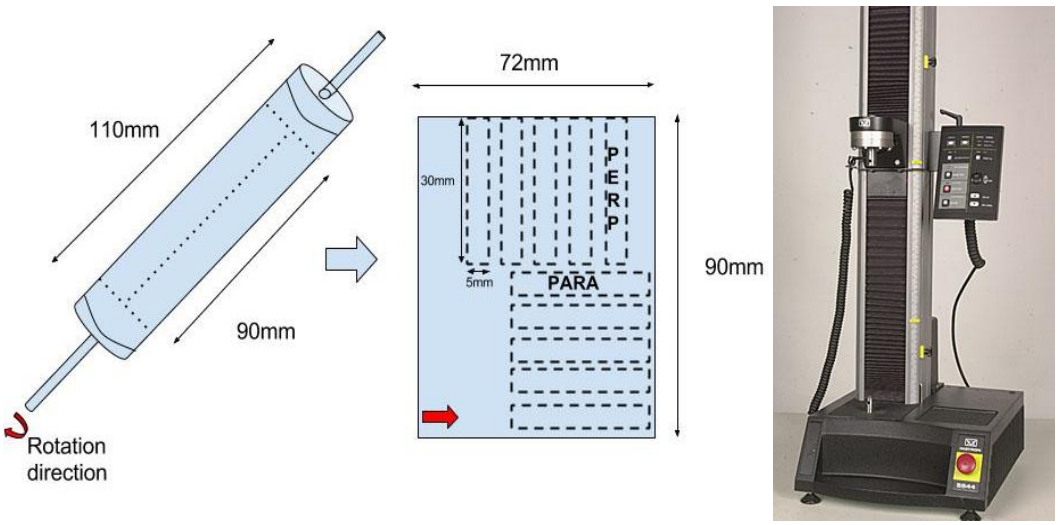

Figure 23: Representation of how scaffold is removed and die cut to obtain PARA and PERP tensile samples, Instron 5544 (right)

Ultimate tensile strength (UTS), ultimate elongation and 10% secant modulus were calculated from the data and reported in MPa and percentage.

3.1.3.7. Porosity

Porosity of a material is defined as the percentage of void spaces relative to the total volume and was determined by gravimetric and densitometric means. Porosity was defined as:

$$P = \left(1 - \frac{V_f}{V_b}\right) \times 100 \quad (2)$$

where P is porosity as a percentage, V_b is the bulk volume of the scaffold and V_f is the volume of the fibers. A rectangular scaffold specimen of known dimensions was die punched from the as-spun scaffold using a die and toggle press. The bulk volume (V_b) of the scaffold was calculated by the known width and length dimensions, multiplied by the thickness, measured with a digital thickness gauge.

In the densitometric method, the fiber volume (V_f) was calculated as:

$$V_f = V_{EtOH} = \frac{m_{EtOH}}{\rho_{EtOH}} = \frac{m_{Air} - m_{Sub}}{\rho_{EtOH}} \quad (3)$$

where the mass of ethanol (m_{EtOH}) was calculated by weighing the sample in air (m_{Air}) and submersed (m_{Sub}) in 100% ethanol (EtOH, ρ = 0.789 g/ml) on a 5-decimal balance (Mettler-Toledo, Columus, OH) fitted with a densitometric kit. Densitometric porosity was determined by substituting the value for V_f into equation (2).

In the gravimetric method, the fiber volume was calculated as the weight of the sample divided by the manufacturer stated density of polymer (ρ = 1.16 g/ml) (eq. 4). This value was then used in equation (2) to determine gravimetric porosity.

$$V_f = \frac{m_{Sample}}{\rho_{PU}} \qquad (4)$$

3.1.3.8. Permeability

Permeability can be defined as the ability of a substance to allow for other substances, be it gas, liquid or solid, to pass through its inherent pores (Zilla & Greisler, 1999). Determining blood permeability of a fabric structure is challenging and hence water permeability was taken as an estimated correlation (Ratner, Hoffman, Schoen, & Lemons, 2012). To calculate permeability of electrospun samples, (**1**) die cut specimens were fixed firmly in (**2**) a PVC flange with (**3**) a 1 cm^2 orifice which was connected to a reservoir of water with a one-way valve. (**4**) Pressure was applied to the reservoir using compressed air, a gas regulator and a digital M2 series manometer (Meriam, Cleveland, USA) (see Figure 24). When pressure readings stabilized, the valve was opened, and the amount of water collected in 1 minute was measured using a graduated measuring cylinder and reported as permeability in $ml/cm^2/min$.

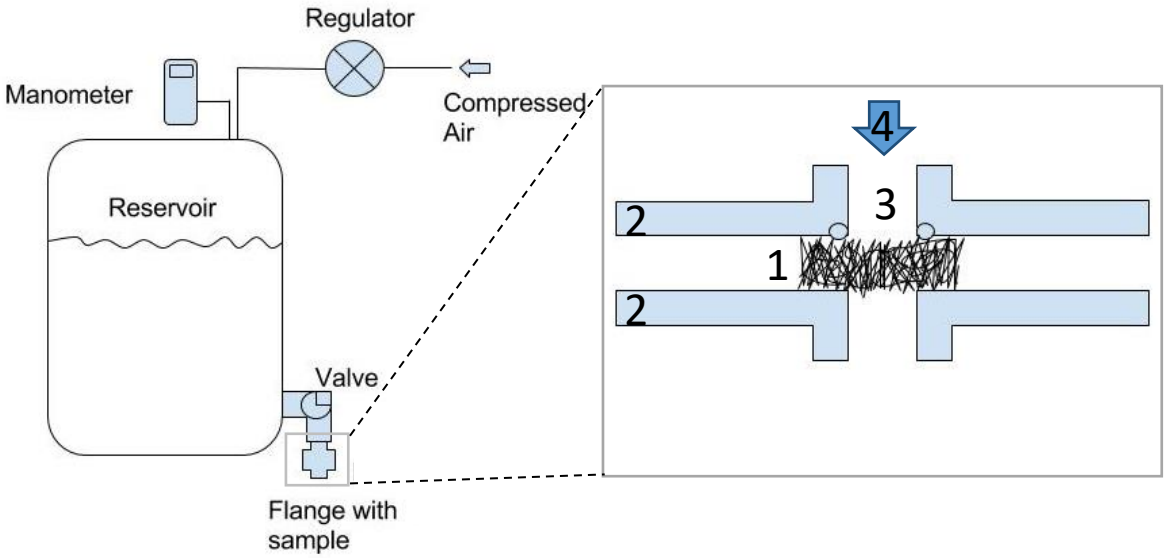

Figure 24: Schematic representation of permeability testing

3.1.3.9. Residual solvent determination

Ensuring no residual solvents are present after manufacturing is crucial for scaffolds that are to be used for biomedical applications, since organic solvents, even at low concentrations can be toxic to cells. (Xie, Li, & Xia, 2008). Although most of the solvent evaporates during the spinning process, residual solvents that may have remained were removed by drying in a regular laboratory oven at 45 °C for 90 minutes. Solvent removal was confirmed using gas chromatography (GC) headspace analysis. (Roediger Agencies, Stellenbosch, South Africa).

Briefly, sealed vials with septa containing the as-spun (n = 1) and oven dried (n = 1) samples were heated to 150 °C for 1 hour while being agitated every 10-20 seconds. Using a syringe, 1 mL of headspace was injected into a gas chromatograph equipped with a mass spectrometer (detection limit = 0.001 µg). Retention peaks were observed on the spectrograph and matched to a library database with known substances and the area under the peak was calculated and correlated to solvent mass, expressed in µg. The detection method used in the mass spectrometer was electron impact ionization (EI). EI is a hard ionization technique, which produces extensive fragmentation of the ionized parent molecule. Amount of residual solvents are reported as µg/g sample.

3.2. Results & Discussion

3.2.1. Effect of feed flow rate and solution concentration

Initial process optimization (15 wt% solution; batch 1, virgin pellets) was focused on spinning scaffolds with repeatable fiber diameters by evaluating the solution concentration and solution feed flow rate. Increasing the flow rate from 2.5 to 4 ml/hour yielded an increase in fiber diameter of 0.72 µm ($p=0.051$) while changing solution concentration from 15 to 20 wt% (constant 2.5 ml/hour flow rate) yielded a fiber diameter increase of 2.11 µm ($p < 0.0001$) (see Figure 25). With regards to feed flow rate, the effect of increasing fiber diameter could be the result of decreased charge density due to increased flow rate which would create a longer stable jet (thus a shorter distance the fibers are drawn during the whipping region) resulting in increased fiber diameter (Cadafalch Gazquez et al., 2017). Considering the effect due to solution concentration it can be argued that the higher viscosity due to the increase in solution concentration presents a counter force to the electrostatic repulsion responsible for the thinning and stretching of the solution jet explaining the observed thicker fibers (see Figure 26). All though a similar trend of increasing fiber diameters can be seen when spinning at 4 ml/hour flow rate, no fibers were obtained when spinning from 25 wt% solution concentrations. This is due to wet bonding of fibers on the mandrel and coagulation to form a film rather than the desired fibrous structure. The increase in the standard deviation at higher solution concentrations and feed flow rates could indicated the loss of uniformity of the fibers produced.

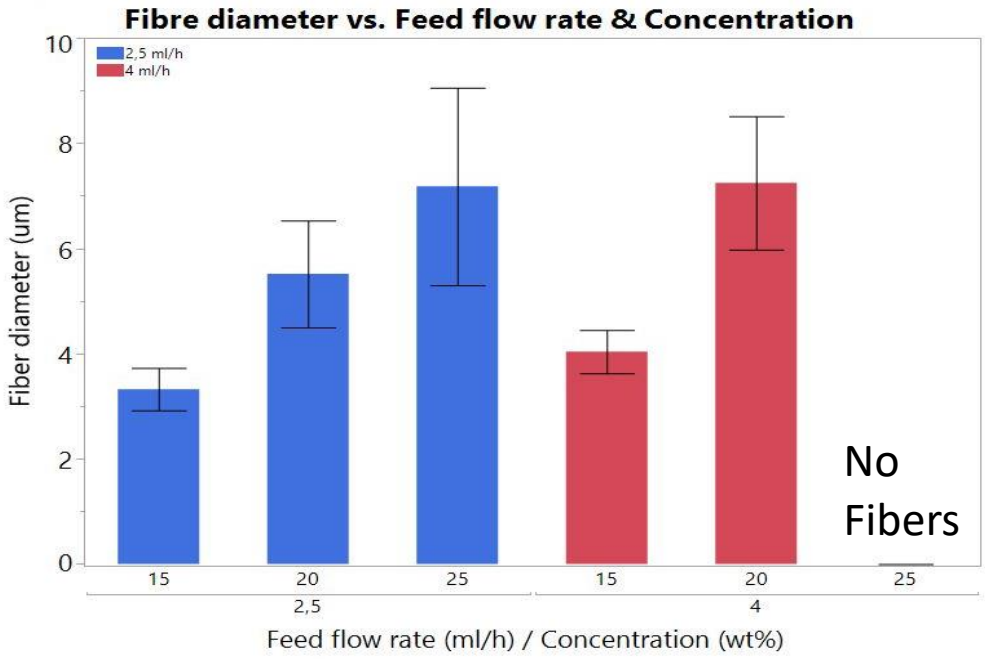

Figure 25: Bar graph of fiber diameter vs solution concentration at two different feed flow rates

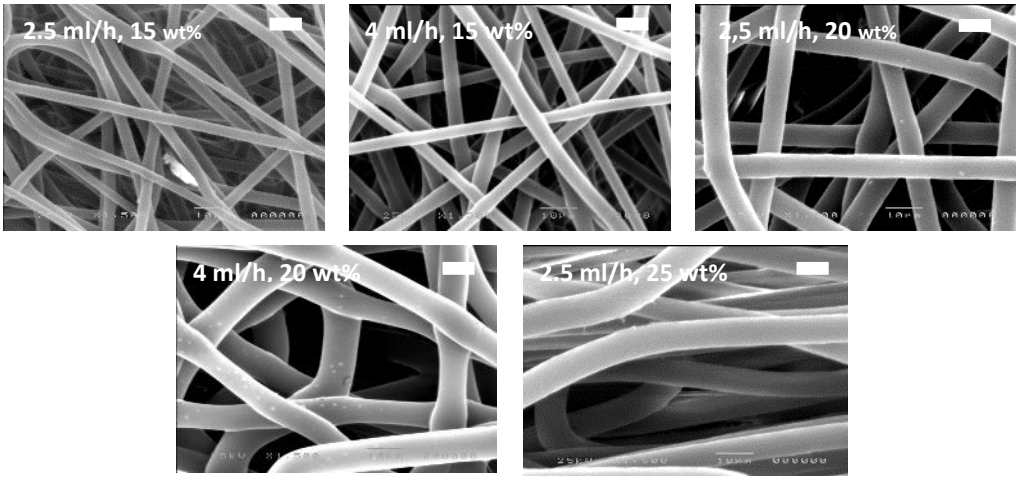

Figure 26: SEM images of fiber morphology at increasing feed flow rates and solution concentrations, white bar represents 10 µm

After process standardization, overall average fiber diameter, irrespective of scaffold side was 3.17 ± 0.64 µm (n=15) (Luminal = 3.16 ± 0.68 µm, Abluminal = 3.17 ± 0.59 µm). The fiber diameter was seen to remain relatively consistent throughout the period and number of scaffolds tested, as illustrated by the boxplot (see Figure 27 **A**).

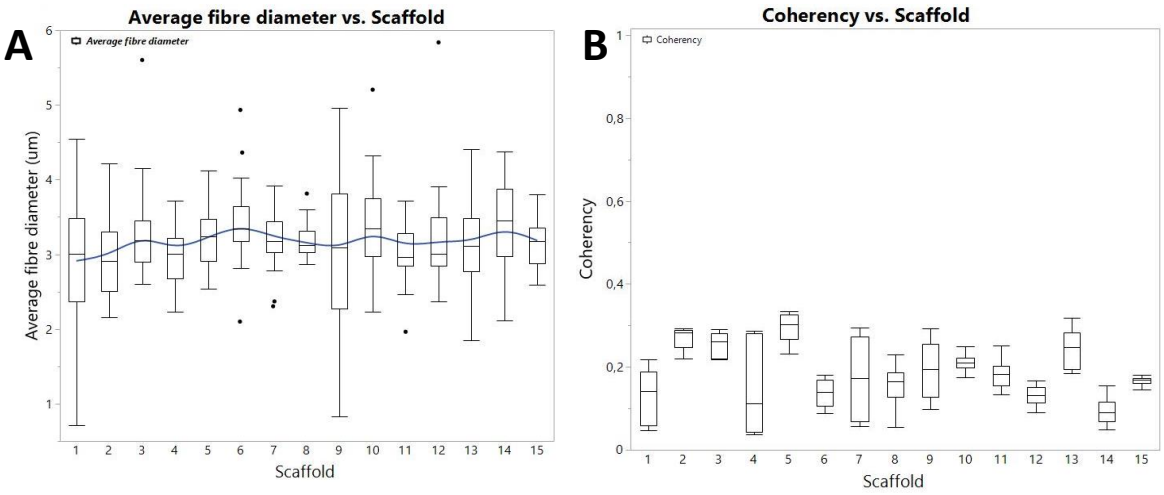

*Figure 27: Boxplots of average fiber diameter (**A**) and coherency (**B**) across 15 scaffolds after process standardization. The blue line is for display purposes only.*

Scaffolds were spun from three solution concentrations at a constant feed flow rate (see Table 7) and the coherency evaluated as describe in the methods section. Coherency of the scaffold spun from the 15 wt% is 0.414 which indicates that the fibers are orientated in all directions to some degree, but slightly more in one direction. This is ascribed to increased whipping due to the lower solution concentration leading to preferential orientation in the direction perpendicular to rotation as evident. From the SEM image, the top layers of fibers are orientated more in one direction, explaining the coherency value of 0.414. The scaffold spun from 20 wt% with a 0.305 coherency value, indicates the highest isotropy.

Table 7: Coherency values of scaffolds spun from different solution concentrations

Solution concentration (wt%)	Feed flow rate (ml/hour)	Coherency (0 = full isotropic, 1 = anisotropic)
25	2.5	0.853
20		0.305
15		0.414

In contrast, the higher concentration solution had a coherency value of 0.853, indicating that the fibers are orientated predominantly in one direction. It was noted that at higher concentrations, the stable region before whipping increased in length leading to a smaller deposition area of the fibers on the collector. At 25 wt% concentration and 2.5 ml/h flow rate, minimal whipping of the fiber was observed, leading to a definitive increase in fiber orientation in one direction (see Figure 28,Table 7) and a physically wetter scaffold compared to lower solution concentrations. From the data it seems that the 20wt% solution has the ideal whipping and drying behavior that results in a scaffold with fibers evenly orientated in all directions.

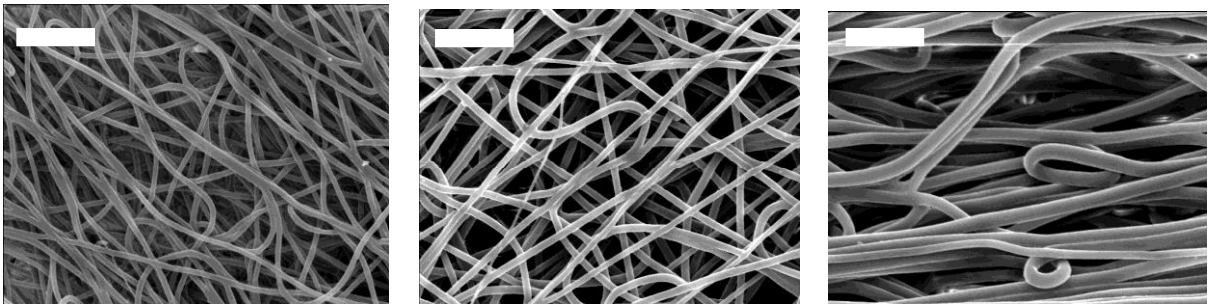

Figure 28: SEM images of scaffold spun at a feed flow rate of 2.5 ml/h and a solution concentration of 15, 20 and 25wt%. White bar represents 50 µm

The average coherency value across 15 tested scaffolds after process standardization were 0.18 ± 0.07, indicating that scaffolds were predominantly isotropic (see Figure 27 **B**). The optimization we performed with solution concentration and feed flow rate as described above provided us with reasonably reproducible scaffolds on which we initiated further characterization tests.

3.2.2. Viscosity variations with molecular weights

Variations in the MW of received CarboSil 80A batches (1 – 3, see Table 5) resulted in solutions with different viscosities at identical concentrations. Initially, the process was optimized to a solution concentration of 15 wt% using batch 1 in the virgin pellet form. Batch

2 in the virgin pellet form was found to have increased viscosity. We then decreased the concentration to 13 wt% to get similar spinning to the previous batch. Similar adjustments have been seen in literature; According to a study investigating the effects of molecular weight on solution viscosity, a 20% difference in viscosity between 241 kDa and 217 kDa Carbothane 75A solutions (17 wt% solutions) were observed. (Cadafalch Gazquez et al., 2017). This 20% change in viscosity resulted in beaded fibers when attempting electrospinning from the lower viscosity solution (Nezarati, Eifert, & Cosgriff-Hernandez, 2013b). The difference in MW between batch 1 and 2 was minor when compared to the MW of batch 3. Fully dissolving batch 3 pellets was not possible, (gel particles remained even after 12 hours @ 60° C) which was likely due to the higher MW of this lot. Thus, pellets of batch 3 were heat pressed to reduce crystallinity and facilitate complete dissolution.

H-bonding present in the polymer could lead to stronger intermolecular forces between the hard segments and resist full dissolution by a THF/DMF solvent system. A study investigating the effect of H-bonding on chemical and physical properties of polyurethanes showed a decrease in viscosity between H-bonded and non H-bonded polyurethanes (C. Prisacariu, Scortanu, & Prisacariu, 2010). Fewer H-bonds leads to less association in solution between polymer chains, resulting in lowered viscosity. Additionally, after heat pressing, microphase mixing (which is inversely related to H-bonding) is increased, therefore reducing H-bonding. (Cristina Prisacariu, 2011).

Table 8: Different solution viscosities of CarboSil 80A at 16wt% in THF:DMF (Pellet) used in this study compared to similar findings with a different polymer (Carbothane 75A, blue shading, n=1)

Polymer (as received)	Molecular weight (kDa)	Solution concentration (wt%)	Viscosity (cP)
CarboSil 80A	295	16	2458
	340		10467
	449		67000
Carbothane 75A (Nezarati et al., 2013b)	217	17	8000
	241		10000
	217	18	10000

As such, the difficulty of the higher molecular weight CarboSil 80A (batch 3) to fully dissolve can be attributed to increased H-bonds that were formed between the higher molecular weight hard segments (HS) of the polymer. It is hypothesized that after heat pressing,

crystallinity decreases, and these hydrogen bonds are partly dissociated, allowing for full dissolution. Lastly, thermally labile allophonate bonds, present as chemical crosslinks due to the side reaction of unreacted isocyanate groups with urethane groups, may also have influences on processing of the polymer which is negated with heat pressing (Bhowmick & Stephens, 2000).

To ensure repeatable electrospinning and to account for the variations in MW of different batches of CarboSil 80A, solution viscosity was deemed as a more useful parameter than solution concentration. Viscosities of 2000 – 3000 cP were found to be most suitable for the current study, resulting in an ideal Taylor cone (see Figure 29). However, the resultant change in solution concentration leads to different solvent to polymer ratios, influencing the conductivity of the solution and hence indirectly the resulting scaffold.

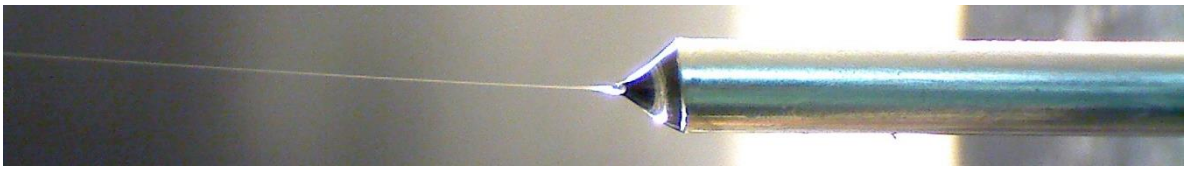

Figure 29: Macro photograph of an ideal Taylor cone, showing the jet ejecting from the tip

Solutions made from heat pressed polymer were observed to have lower viscosities than solutions from the virgin pellet counter parts (see Figure 30). Solutions from batch 1, 2 and 3, respectively showed 88%, 87% and 96% reduction in viscosity when prepared from heat pressed polymer instead of the virgin pellets. Viscosity of polymer solutions (i.e. resistance to flow) decreases with decreasing MW (see Figure 30) in both the virgin pellet and heat pressed forms. For example, at the same solution concentration there is a 96% difference in the viscosity between solutions prepared from the pellets of batch 3 and batch 1, with batch 3 having the higher MW and thus viscosity. The same trend is observed even after heat pressing the pellets to lower the solution viscosity. Even though the viscosity of batch 3 decreased by 96% after heat pressing, there is still an 88% difference in viscosity between solutions prepared from the heat pressed films of batch 3 and batch 1.

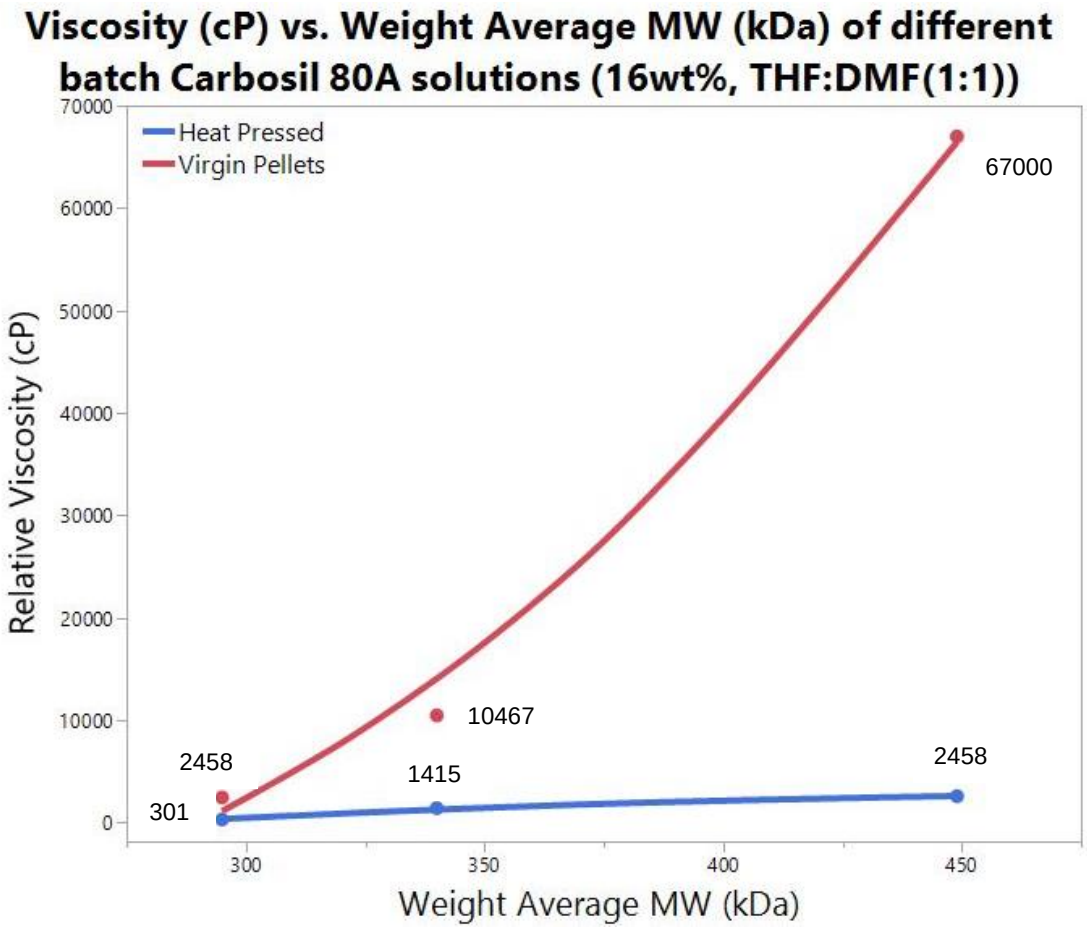

Figure 30: Viscosity vs weight average molecular weight of CarboSil 80A solutions from virgin pellet and heat pressed polymer at 16 wt% in THF:DMF(1:1) (batch 1, 2 and 3)

However, when considering the relative viscosities of solutions prepared from batch 1 – 3 (after heat pressing) it was observed that they all have values within a much smaller range, from 301 – 2479 cP. Thus, heat pressing allowed us to standardize the preparation of the electrospinning solution from different batches by using the relative viscosity as the parameter by which to prepare solutions.

To analyze the effect of the MW on solution viscosity, we performed FTIR and DSC measurements of the virgin pellets and heat pressed films from the different polymer batches.

3.2.3. FT-IR

FTIR spectra of the virgin pellet (RED) and heat pressed (BLUE) forms of CarboSil 80A (batch 3) are shown in Figure 31 & 28, from which it is clear, that differences exist between the two forms. Both show absorption peaks at 3331 cm^{-1} corresponding to a hydrogen bonded amino group in a urethane (Yang et al., 2013). After heat pressing, the peak shows

a slight decrease in area (BLUE line) that could be attributed to dissociation of amino H-bonds, mostly between hard segments.

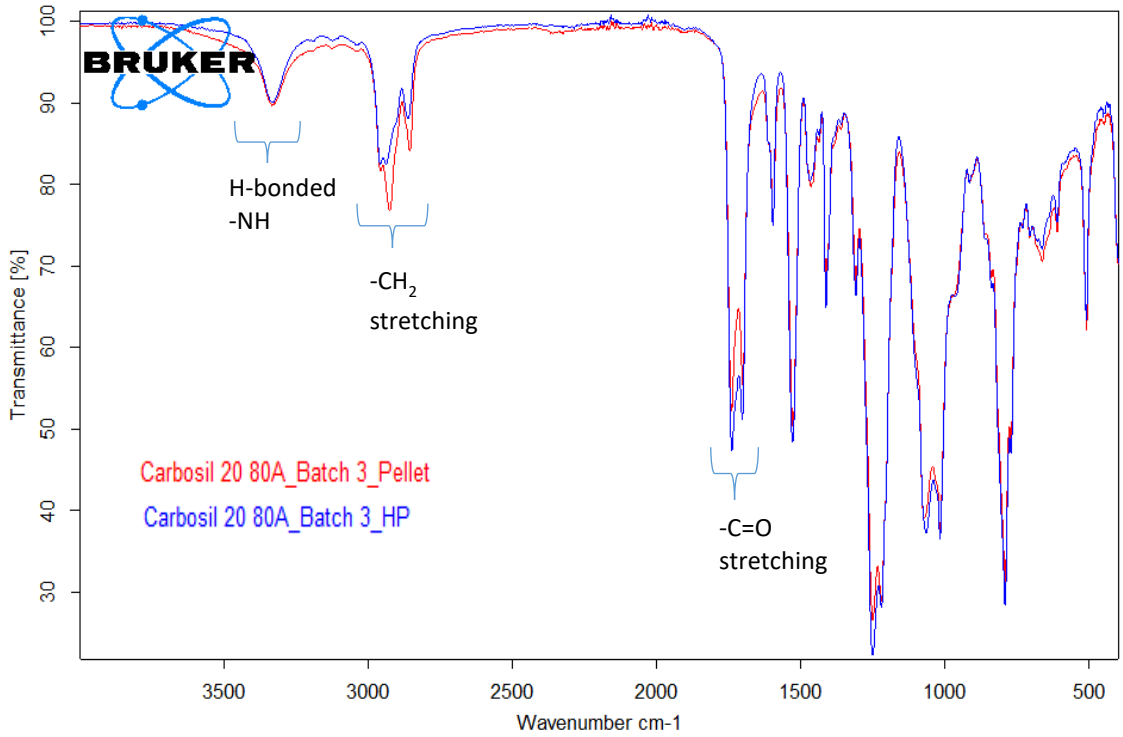

Figure 31: FTIR-ATR spectra of CarboSil 80A (batch 3) in the heat pressed and pellet forms

Peaks between 2850 and 2960 cm^{-1} are assigned to symmetrical and asymmetrical stretching of CH_2-groups in the polycarbonate diol (Zhu, Wang, Zhang, Ma, & Wang, 2016) (see Figure 31). The salient feature in this area is the reduction of one peak of the bimodal band at 2924 cm^{-1} after heat pressing. Possibly the reduction in peak intensity can be explained by the -CH_2 groups undergoing different vibrational modes due to decreased crystallinity caused by the quick cooling rate after heat pressing.

Table 9: FTIR peak assignment

Wavenumber (cm^{-1})	**Assignment**
3331	N-H stretching
2957	CH_2 asymmetric stretching
2855	CH_2 symmetric stretching
1738	C=O stretching (carbonate, free)
1700	C=O stretching (urethane, H-bonded)

Peaks at 1738 and 1700 cm^{-1} are assigned to absorption of the two types of carbonyl groups found in PCU's, namely the SS carbonate- and HS urethane carbonyls respectively (Figure 32). Due to both groups ability to form H-bonds, this area can be associated with as much as 5 overlapping peaks (E. Cipriani, Bracco, Kurtz, Costa, & Zanetti, 2013).

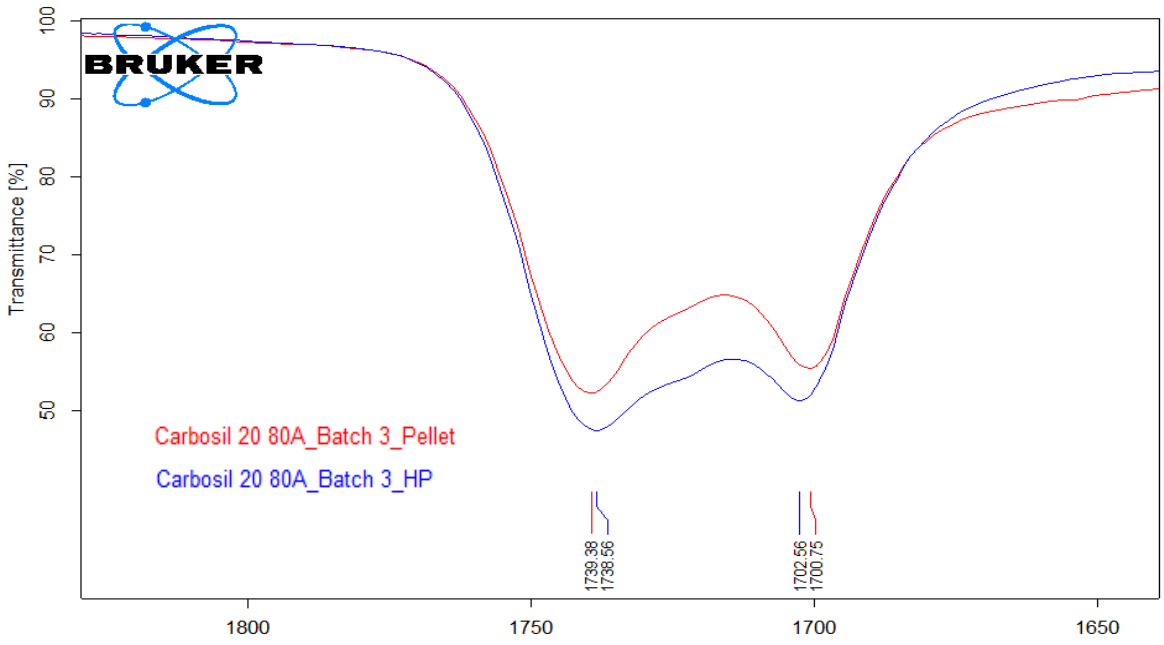

Figure 32: Zoomed in FTIR_ATR spectra of CarboSil 80A (batch 3) in the heat pressed and pellet form: 1800 – 1600 cm^{-1}, carbonyl (diol and urethane) stretching

The peak at 1738 cm^{-1} is assigned to the carbonyl which is not involved in H-bonding, while the peak at 1700 cm^{-1} is assigned to the H-bonded hard segment carbonyl group in the urethane. The increase in area can possibly be attributed to overlapping peaks of groups that after heat pressing are no longer involved in H-bonding.

The feint shoulder seen forming at around 1720 cm^{-1} can be attributed to the disruption of the short- range order and hydrogen bonding of both the hard and soft segment carbonyls in the amorphous phase (Bracco, Zanetti, Cipriani, & Costa, 2010). It is also said that this peak corresponds to the loosely H-bonded carbonyl groups in the soft segment.

The subtle changes observed in the infrared vibrational modes of the virgin pellet and heat pressed forms are consistent with changes in crystallinity and H-bonding density, as is expected when a polymer is heat pressed. The results are also in good correlation with changes seen in viscosity as described in the previous section.

3.2.4. DSC

Upon analysis of the melting properties of CarboSil 80A (see Figure 33), the virgin pellet and heat pressed form show distinct differences. The DSC thermogram of the as-received pellet shows one broad endotherm at 135°C (120 – 155°C) while the thermogram of the heat pressed form shows 2 distinct endotherms at 69°C (57 – 83°C) and 163°C (122 – 186°C). This multi-endothermic behavior is characteristic of thermoplastic polyurethanes and the position and size of the endotherms depend among other things on the composition ratio of the material as well as annealing and processing temperatures. (Martin et al., 1997).

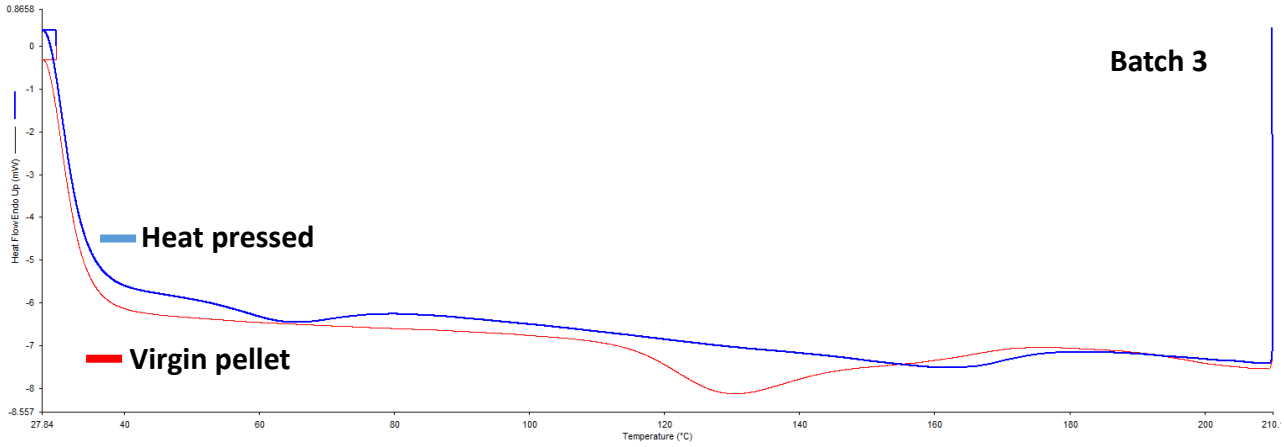

Figure 33: DSC thermogram of heat pressed (BLUE) and pellet (RED) form of CarboSil 80A (batch 3)

The broad thermal transition (115 – 150 °C) in the pellet thermogram corresponds to the crystalline melting point (T_m) of the polymer, indicating a high level of crystallinity in the as manufactured state. A study examining the effect of differing annealing temperatures on Bionate 80A, a biomedical polycarbonate urethane similar to CarboSil 80A, shows similar thermal transitions of the as-received form vs a sample annealed at 180°C (Bracco et al., 2010).

The observation that the heat pressed form has two endotherms shows a decrease in crystallinity and some shorter-range ordering may be indicated by the lower temperature endotherm. This short-range ordering is dependent on the thermal history of the material (Elisa Cipriani, Zanetti, Brunella, Costa, & Bracco, 2012).

The restructuring of the two phases into their preferred energy states is a time dependent process and could be different depending on how long after heat pressing (annealing), the analysis is performed.

From these experiments, CarboSil 80A is very sensitive to processing temperatures and this should be considered when the material is manufactured since it may have undesirable

effects on the processing properties. Also, the higher crystallinity observed by DSC together with H-bonding agrees with the previous data obtained on relative viscosity and FTIR spectra as the probable cause of the gel particles observed during dissolution of the virgin pellets of batch 3.

In conclusion, from the data presented using solution concentration as a parameter to obtain consistent scaffold spinning is not reliable, due to the inherent variation of polymer batches as obtained from the supplier. We have however shown that by heat pressing the virgin pellets we obtain a polymer of relative consistent crystallinity which allows us to use relative viscosity as parameter to make up solutions from which to spin consistent scaffolds. Being able to spin reproducible scaffolds we then proceeded to further characterized the scaffolds in full.

3.2.5. Scaffold characterization

3.2.5.1. Effect of rotation speed on UTS

As expected, during process optimization it was observed empirically that the rotation of the collecting mandrel has an influence on the UTS of the scaffold. The speed of mandrel rotation influences the rotational alignment of the scaffold and hence the mechanical properties in 2 directions, perpendicular ($UTS_{\perp}$) and parallel ($UTS_{//}$) to the direction of rotation (as described in section 3.1.3.6), were tested using different batches of CarboSil 80A (batch 1 and 3).

In both batches, the $UTS_{//}$ increased with rotation speed. The increased $UTS_{//}$ is expected since with an increase in rotation speed, more of the fibers should align in the direction of rotation resulting in more fibers deposited in the parallel direction. The magnitude of $UTS_{//}$ is seen to be similar over the 500 – 1500 rpm range. The increase in the $UTS_{//}$ component is supported by the $UTS_{\perp}$ component decreasing with increasing rotational speeds. An analogous decrease with increasing rotational speed in $UTS_{\perp}$ is seen in both experiments (see Figure 34). In experiment 1, $UTS_{\perp}$ was overall 18% less than $UTS_{//}$, while in experiment 2 the opposite was seen with $UTS_{\perp}$ being 106% higher than $UTS_{//}$. This could possibly be attributed to the different spinning (whipping) characteristics of the higher molecular weight (batch 3) CarboSil leading to increased alignment perpendicular to the rotation.

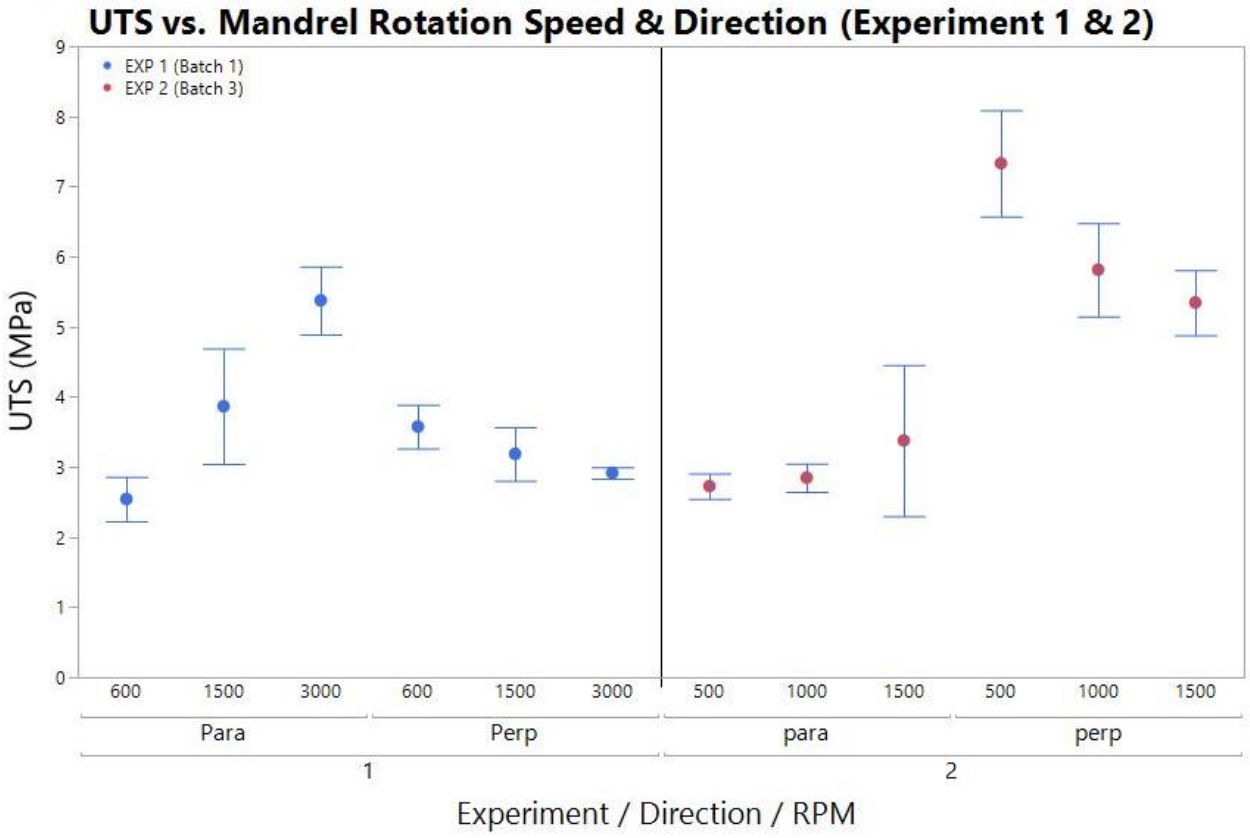

Figure 34: Graph of UTS vs rotation speed (RPM) in the two perpendicular directions of scaffolds spun from batch 1 and batch 3 (excluding batch 2).

Furthermore, in experiment 1, a 52 % increase in $UTS_{\perp}$ existed between rotation speeds of 600 – 1500 rpm while in contrast, only a 24 % increase in experiment 2 between rotation speeds of 500 – 1500 rpm (see Table 10). This observation is further support to indicate that the difference in molecular weights affect the whipping behavior during the spinning process, which affects the alignment of the fibers in the scaffold and hence the strength of the scaffold.

Between experiments, independent of rotation speed and direction, the scaffolds spun from batch 3 were overall 28% stronger than those spun from batch 1 (Experiment 1, n = 3), (Experiment 2, n = 5).

Table 10: UTS results of Experiment 1 and 2 with % difference of relevant categorical groups. Green indicates increase, orange indicates decrease.

Experiment	Direction	RPM	Mean (UTS (MPa))	Std Dev (UTS (MPa))	% difference in UTS relative to:		
					RPM	Direction	Experiment
1	PARA	600	2,54	0,32			
		1500	3,87	0,82	52		
		3000	5,38	0,49			
	PERP	600	3,58	0,31		18	
		1500	3,19	0,38	11		
		3000	2,92	0,08			
2	PARA	500	2,73	0,18			28
		1000	2,85	0,20			
		1500	3,38	1,08	24		
	PERP	500	7,33	0,76		106	
		1000	5,81	0,67			
		1500	5,35	0,46	27		

These variations between similar experimental setups using different batches polymer shows the sensitivity of the electrospinning process to molecular weight of the polymer.

3.2.5.2. Mechanical properties

After optimization of feed flow rate, solution concentration (viscosity) and mandrel rotation speed, the mean UTS per scaffold (spun from batch 3), regardless of direction, was 5.70 ± 2.5 MPa. This was calculated across 15 different scaffolds over a period of 6 months. Mean $UTS_{\perp}$ was predominantly higher than the $UTS_{//}$. This variation (see Figure 35 **B**) may be explained by the molecular weight of the polymer (see sections 3.2.5.2 above) and additionally by the inability to precisely control temperature successfully, leading to different solvent evaporation rates, which in turn would lead to variable amounts of fusion between fibers, so influencing the UTS.

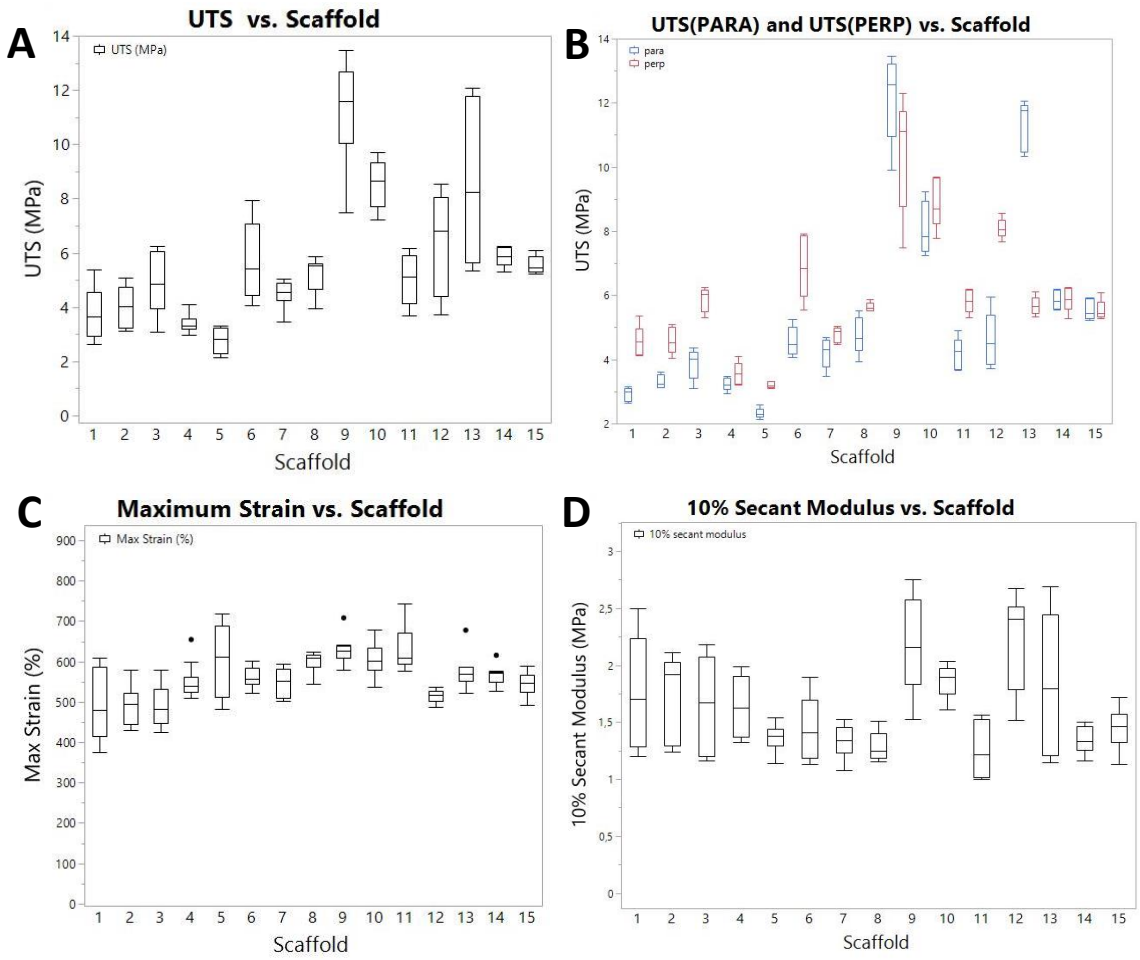

*Figure 35: Mechanical Properties of 15 scaffolds spun from batch 3. UTS (**A**), UTS per direction, PARA (BLUE), PERP (RED) (**B**), Max. Strain (**C**), 10% secant modulus (**D**)*

The mean maximum strain at break was 527 ± 80 % and remained relatively constant throughout the study. The modulus at 10% strain was 1.62 ± 0.43 MPa showing similar variations at scaffold 9 and 10 than with the UTS.

3.2.5.3. Effect of relative humidity on scaffold integrity

Observation of the direct effects of relative humidity and temperature on the scaffolds produced were of interest. It was observed that if all parameters except RH and temperature were kept constant (see Table 11) significant differences in workability of the resulting scaffold were evident. Workability is subjectively defined as the ease by which the scaffold can be handled and used in further processing. Relative humidity (RH) was found to have a profound effect on the resulting scaffold and its integrity. Traditionally, solvent free fibers are desired with electrospinning, which usually results (solvent dependent) from spinning in as dry as possible conditions (low RH). On the contrary, spinning at higher RH's can lead to wet landing and film formation.

Table 11: Effect on workability due to variation in environmental parameters of sequentially spun scaffolds

Parameters	Scaffold #1	Scaffold #2
Relative Humidity (%)	44	34
Temperature (°C)	18.4	19.2
Workability	Elastic & retains shape. No snagging	Non-elastic & deforms after use. Easily snags
Appearance	Smooth	Fibrous

Spinning below 35% RH with CarboSil (batch 1, low MW), the scaffold integrity differs greatly from when spinning at a RH of 44%. The scaffold spun at the higher RH had a more elastic handling characteristic after removal from the mandrel (see Figure 36 A). This can be correlated to the inter-fiber fusion (see Figure 36 B) that occurred as the fibers landed, which is partly due to the fibers not being fully dried when landing on the mandrel. The loss of integrity and the elastomeric nature of the scaffold at a humidity below 35% can possibly be attributed to little or no inter fiber fusion, allowing the fibers to slide over each other as individual fibers rather than the scaffold deforming as a whole. When the RH was below 35%, the scaffold delaminated and did not retain its shape resulting in scaffolds unsuitable for use as a sealing skirts. When handling a scaffold after spinning, a certain degree of elasticity and integrity is required to make it workable.

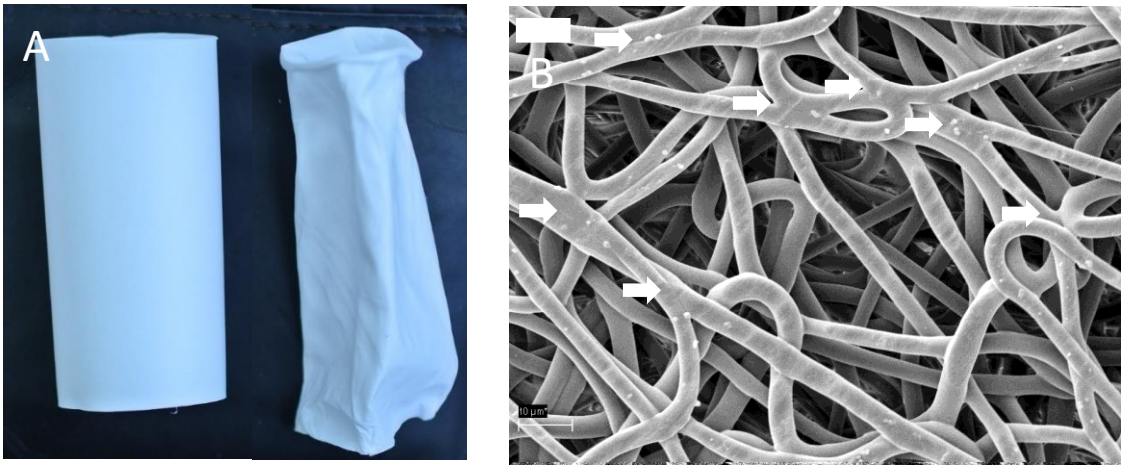

Figure 36: Macro photograph (A) of the difference in gross scaffold morphology with %RH changing from 44% (left) to 34% (right) and SEM image (A) of inter-fiber fusion indicated by white arrows. White bar represents 10 µm

3.2.5.4. Undulation anomalies

During the spinning of some humped scaffolds lines were observed exclusively on the hump area of the scaffold (see Figure 37).

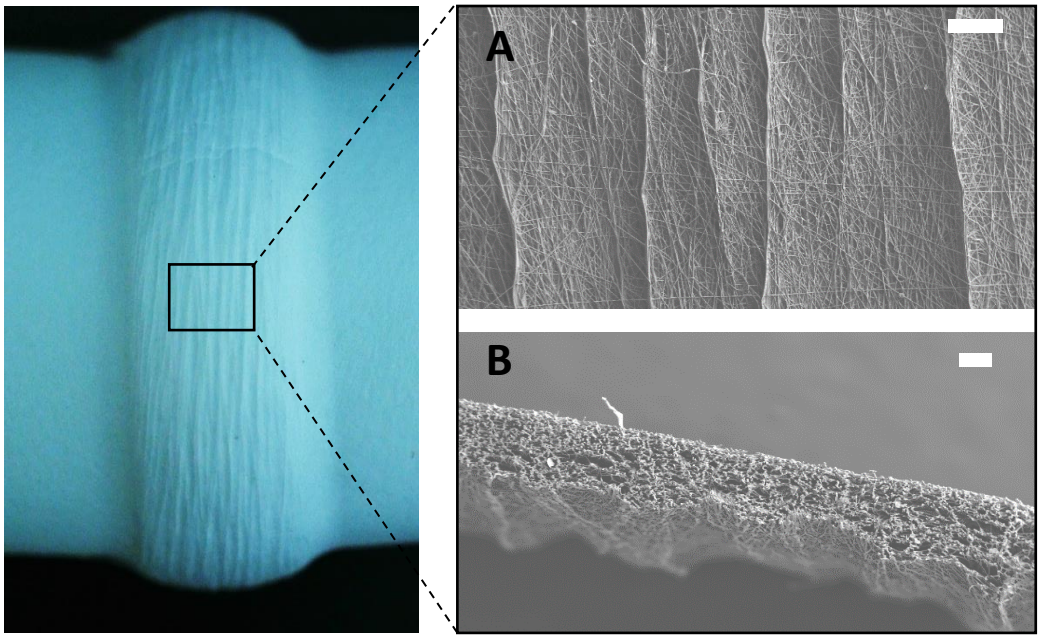

Figure 37: Macro image of undulations on hump area of scaffold (left) with SEM images from top (A), and the side-on view of the hump section with the lines on (B). White bars represent 200 and 100 µm respectively.

SEM images of the side-on and top view showed that these anomalies were surface phenomena and the undulations were not present throughout the bulk of the scaffold. (see Figure 37). At this point, we have not been able to explain this observed phenomenon but is likely linked to environmental conditions combined with the charge concentration on the hump area of the mandrel.

3.2.5.5. Permeability

A measure of water permeability through the scaffold may help in understanding the leakage mechanism as observed during *in-vitro* testing. Mean water permeability was 1616 ± 1344 ml/cm^2/min across all samples tested (n=8). As expected, the intra-sample trend was that with increasing thickness of the scaffold, permeability decreased. On the other hand, inter-sample variations exist for similar thickness groups (see Figure 38). These variations in permeability were due to different morphologies because of slight changes in the environmental conditions. However, the intra sample changes can possibly be ascribed to which parts of the scaffold were used to prepare the sample. A sample taken from the thicker center of a scaffold will obtain or retain a higher amount of solvent for longer and subsequent

inter-fiber fusion may be more. Similarly, the opposite is true for thinner scaffold sections, less inter-fiber fusion is expected.

Correlating water permeability of arterial prosthetic materials to porosity has been shown by linear regression to only be weakly related (Guidoin et al., 1987). Commercially available PET fabrics used within cardiovascular applications are reported to have water permeability's of 1800 – 4000 ml/cm^2/min and it is stated that water permeability values of < 300 ml/cm^2/min for arterial grafts does not require pre-clotting prior to implantation (Ratner et al., 2012). Even though most of the samples showed permeability's above this value, further optimization and control of the spinning process can lead to more tailored permeabilities.

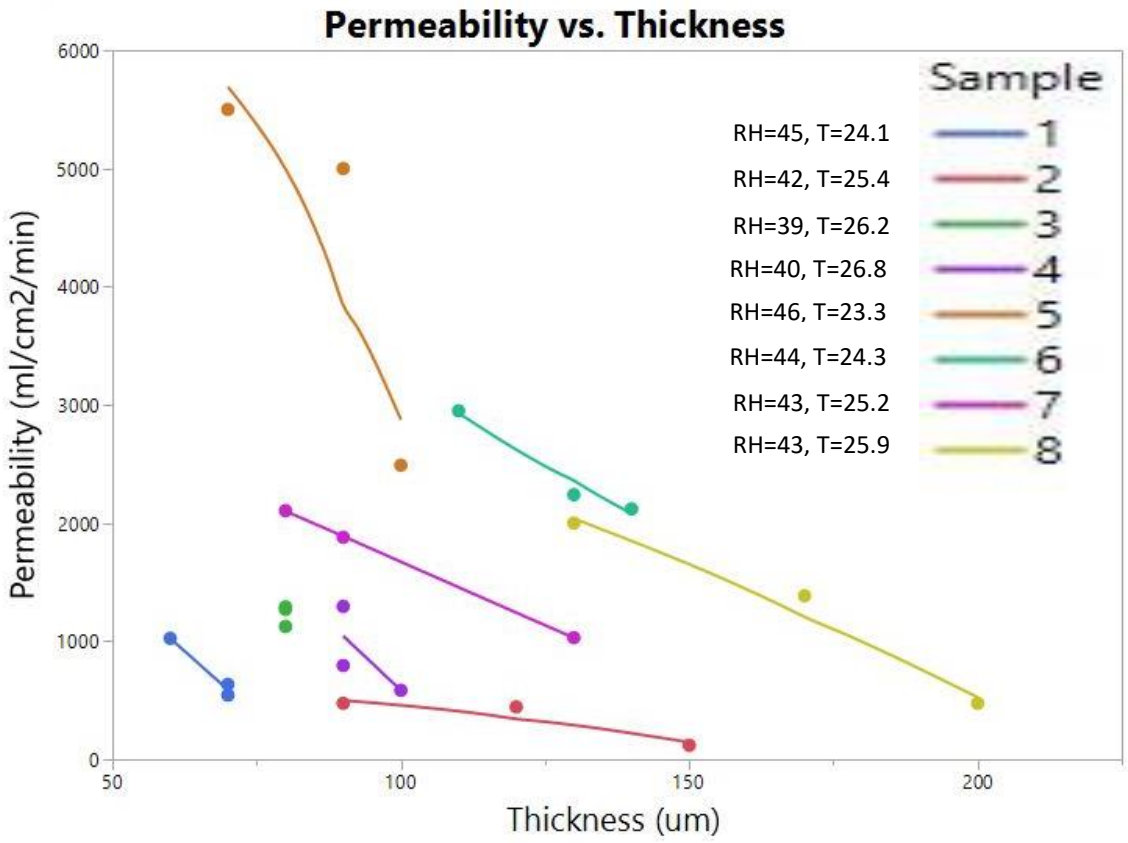

Figure 38: Correlation between scaffold permeability and thickness

This, together with the fact that highly permeable PET fabrics are used as biomedical implants make electrospun scaffolds of sufficient thickness a good option for sealing skirt materials.

3.2.5.6. Pore sizes and porosity

Average equivalent pore sizes, irrespective of scaffold side, were 9.52 ± 6.9 µm (Luminal = 9.25 ± 6.64 µm, Abluminal = 9.82 ± 7.17 µm). The large standard deviation was indicative of the variation in determination of the pore size, inherent in the analysis method. Additionally, a considerable number of outliers were identified (see Figure 39 **A**), showing that the identification and definition of pores using rudimentary image analysis methods to be imprecise and difficult.

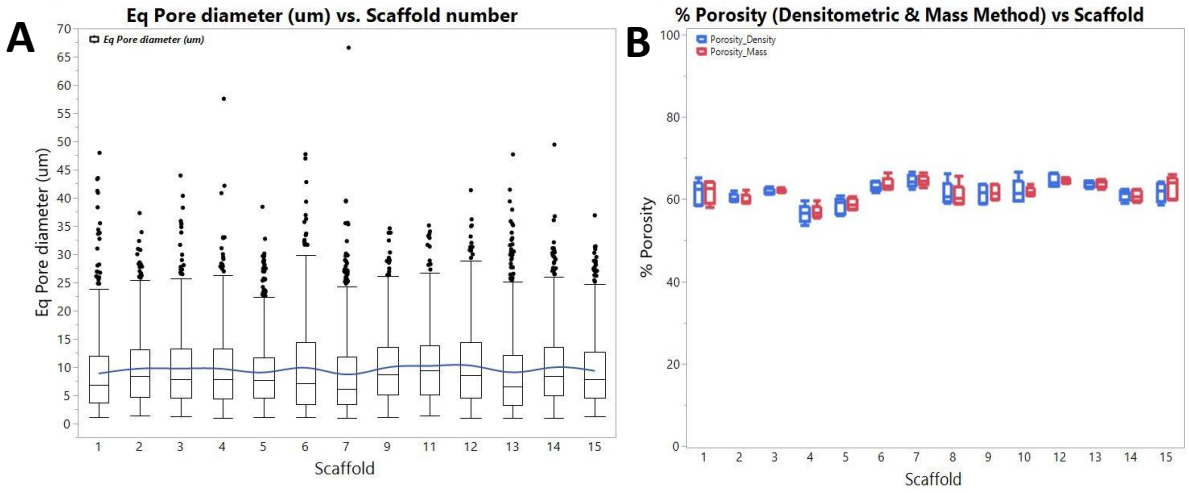

*Figure 39: Boxplots of average equivalent pore sizes (**A**) and porosity (**B**) values across 15 scaffolds. The blue line is for display purposes only*

The average porosity of the scaffolds was 61.5 ± 2.8 and 61.8 ± 2.6% as determined by the densitometric and mass method respectively. This shows good correlation between the two methods used. The porosity results remain relatively consistent throughout the testing period (see Figure 39 **D**).

3.2.5.7. Residual Solvent analysis

Certain organic solvents have a moderate toxic effect on cells and cell proliferation. In a comparative study it was shown that dimethyl formamide (DMF) has greater cytotoxicity than ethanol, acetone and dimethyl sulfoxide (Jamalzadeh et al., 2016). Head space analysis to determine any residual solvent present in the scaffold after spinning showed the higher boiling point DMF (153°C) to be present in the as-spun sample (1.02 µg/g sample). In our case, because of the hard ionization method, DMAc is possibly fragmented by removal of the methyl group as methane gas together with subsequent protonation of the carbonyl group producing DMF as product. After drying for 90 minutes at 45°C the peak representing DMF was absent (see Figure 40), strongly suggesting that all the solvent evaporated from the scaffold. Since peaks corresponding to THF were absent in the as-spun sample, it was

assumed the lower boiling point (66°C) solvent evaporated completely during the electrospinning process. No other compounds were detected (< 0.184 µg/g sample) and the possible presence of such compounds was deemed negligible.

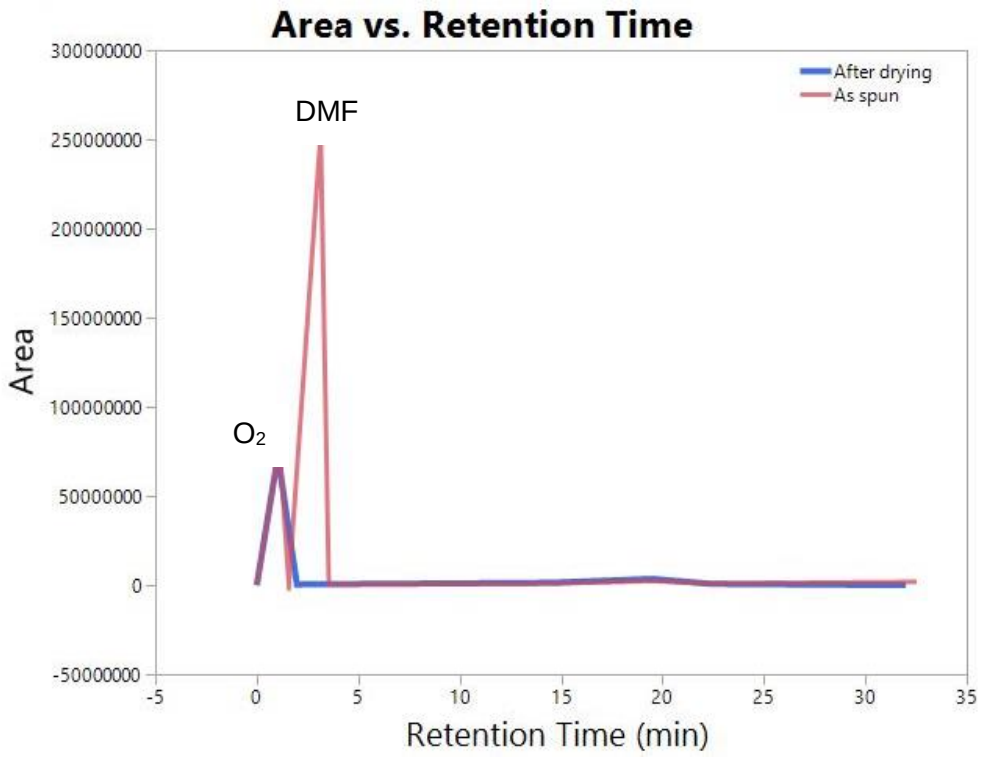

Figure 40: Graph off Area vs Retention time of samples before (red) and after drying (blue)

3.3. Conclusion

In this chapter CarboSil 80A was electrospun into scaffolds that are to be used as sealing skirts for a TAVR valve. Material batch molecular weight was shown to have a substantial effect on the solution viscosity and hence the spinning process and resulting scaffolds. From the many process parameters of the electrospinning process, solution viscosity, relative humidity and mandrel rotation speed was identified as the most important. Using heat pressed CarboSil 80A (batch 3) at 16 wt% the solution properties were found to be suitable and applied to all further work. An applied voltage of +13 kV (and -1 kV) in conjunction with 260 mm tip to collector distance, 1500 rpm mandrel rotation speed and 2 ml/h feed flow rate were chosen as process parameters for spinning scaffolds. Further improvements to temperature control during spinning are required to obtain more reproducible and tailored scaffold properties.

4. Skirt bonding

This chapter describes the materials and methods that were used in the bonding of electrospun scaffolds (Ch. 3) to pre-coated stents for evaluation in a sealing study (Ch. 5). Stent preparation and pre-coating will be explained first, followed by several bonding techniques that were investigated. Bonding patterns and sealing mechanisms for four skirt types will be described, after which test methods to quantify attachment strength are introduced. Bonding and attachment strength results will then be presented, followed by discussion of the outcomes.

4.1. Experimental

4.1.1. Materials

The Cobalt-Chromium alloy (MP35N) chosen as stent material is a well-known medical-grade alloy and was obtained as high precision (± 2 µm) tubes with an outside diameter of 23 mm and an inside diameter of 22.1 mm (Minitubes, Grenoble, France). Hydrochloric acid (HCℓ, 32%), sulphuric acid (H_2SO_4, 98%), nitric acid (HNO_3, 55%), ammonium bifluoride (NH_4HF_2), ethylene glycol ($(CH_2OH)_2$, 99%) and tetrahydrofuran (THF, 99%) were purchased from Kimix Chemicals (Cape Town, South Africa). Dimethylacetamide (DMAc, 99%) was purchased from Merck (Sigma-Aldrich).

4.1.2. Stent preparation

4.1.2.1. Laser cutting

Scalloped stents were cut from MP35N tubes using a StarCut Tube laser cutting machine (ROFIN-BAASEL Lasertech, Gilching, Germany) The process gas was oxygen (10 bars) and cutting speed was 10 mm/s with an offset of 0.04 mm. Laser power was set to 200 W, pulse width to 35 µm and frequency to 4500 Hz. Stents form the basis of TAVR valves and act as the support frame to which the leaflets were sutured and the skirt attached.

Notable features on the stents used in this study are the arch shaped scallop (**1**), having inherent suture holes and act as the attachment line to which leaflets can be sutured, which joins at the commissures (**2**). The various diamond shaped structures (**3**) below the scallop were used for skirt attachment while the circular marker (**4**) indicated the intended landing

zone of the valve. Above the scallop, arms responsible for anchoring mechanisms (**5**) can be seen (see Figure 41).

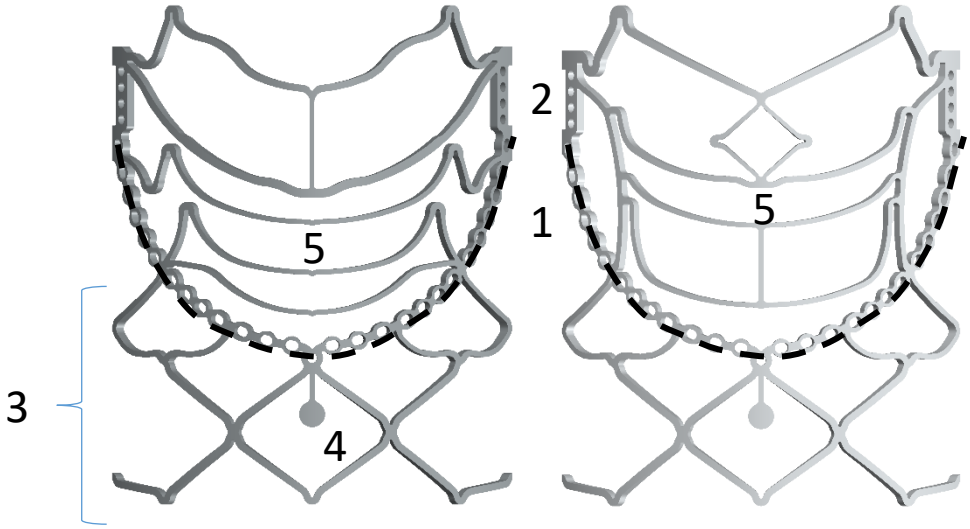

Figure 41: Renderings of stent design 1 (left) and 2 (right) used in this study with marketed areas of interest.

The anchoring mechanism above the scallop improved during the study from design 1 to 2 but this did not influence the skirt attachment areas.

4.1.2.2. Pickling and electropolishing

After cutting, the stents were chemically deburred (pickled) by sonicating at 75 °C in a pickling solution consisting of 6% HNO_3, 12% NH_4HF_2, 15% H_2SO_4 and 67% deionized water. Pickled stents were then electropolished at 6A and 70°C for 5 minutes in a solution of 62% H_2SO_4, 20% HCℓ and 18% $(CH_2OH)_2$.

4.1.2.3. Pre-Coating

The electropolished stents were pre-coated using an in-house designed spraying rig (Strait Access Technologies, South Africa) to successively deposit thin layers of polymer. This pre-coating layer is important since it acted as the substrate to which the skirt was bonded. Briefly, as the stent rotates at a constant speed, 5 wt% CarboSil solution in DMAc was atomized (1 bar) and then deposited onto the stent. Between deposited layers the stent was dried at 60 °C for 2 minutes. Coating thickness was measured using a SMZ800 microscope (Nikon, Tokyo, Japan) and IC Measure image analysis software (Imagine Source, Germany).

4.1.3. Bonding

Four bonding techniques to attach electrospun scaffolds to pre-coated stents were investigated. Varying the tip-to-collector distance during electrospinning attempted to exploit wet landing and encourage adhesion between the scaffold and the stent via solvent bonding. Laser and ultrasonic bonding were investigated since they present attractive possibilities for upscaling the bonding process. Lastly, conductive heat bonding was investigated in several embodiments and semi-automation of the process was evaluated.

4.1.3.1. Direct spinning, wet landing and solvent bonding

Bonding of an electrospun skirt to a valve stent was attempted by spinning directly onto a pre-coated stent and relying on spontaneous adhesion between scaffold and said stent. It must be noted that during manufacturing of these coated stents, a film is inherently added, creating a skirt below the scallop. During electrospinning, to concentrate the landing of fibers onto the (**1**) pre-coated stent, (**2**) insulating tape was placed on opposite sides of the valve to cover the exposed areas of the (**3**) electrospinning mandrel, effectively focusing the landing zone of the fibers.

Wet landing of fibers was achieved by decreasing the (**4**) tip-to-collector distance from 230 mm to 130 mm (See Figure 42). Other parameters used during electrospinning include applied voltages of +13 (base plate) and -1 kV (mandrel), a feed-flow rate of 2 ml/hour and a mandrel rotation speed of 1500 rpm.

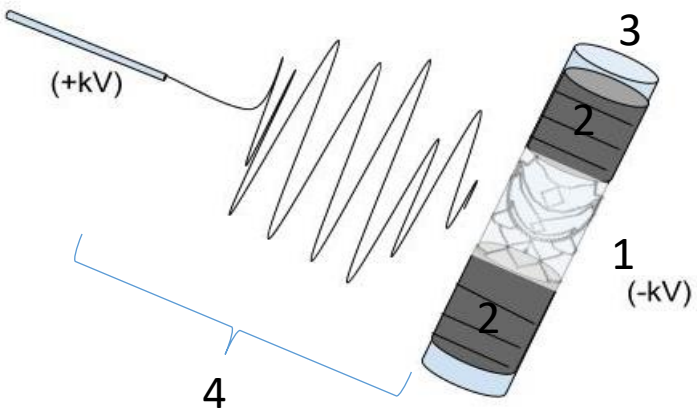

Figure 42: Schematic drawing of electrospinning done with insulating tape and variable distances to achieve concentrated wet landing

For comparison, direct solvent bonding was performed by applying THF to a scaffold on a flat sheet of heat pressed CarboSil 80A and applying the required pressure with the back of a scalpel blade.

4.1.3.2. Laser bonding

To evaluate laser bonding, an electrospun scaffold was placed over 1) a CarboSil 80A coated mandrel and 2) a pre-coated stent and mounted separately in a Type 1410 laser welding machine (BW-Tec, Hori, Switzerland) (see Figure 43). A clear polyolefin heat-shrink tube (d = 25 mm) was shrunk over the coated rod (valve) and scaffold combination. Focal distances between 10-15 mm together with laser power between 7-10 W were used. Bonding times between 10-15 seconds with a constant rotational speed of 200 rpm was applied. The instrument allows for axial and rotational manipulation during the process but not for complex bonding paths to be followed.

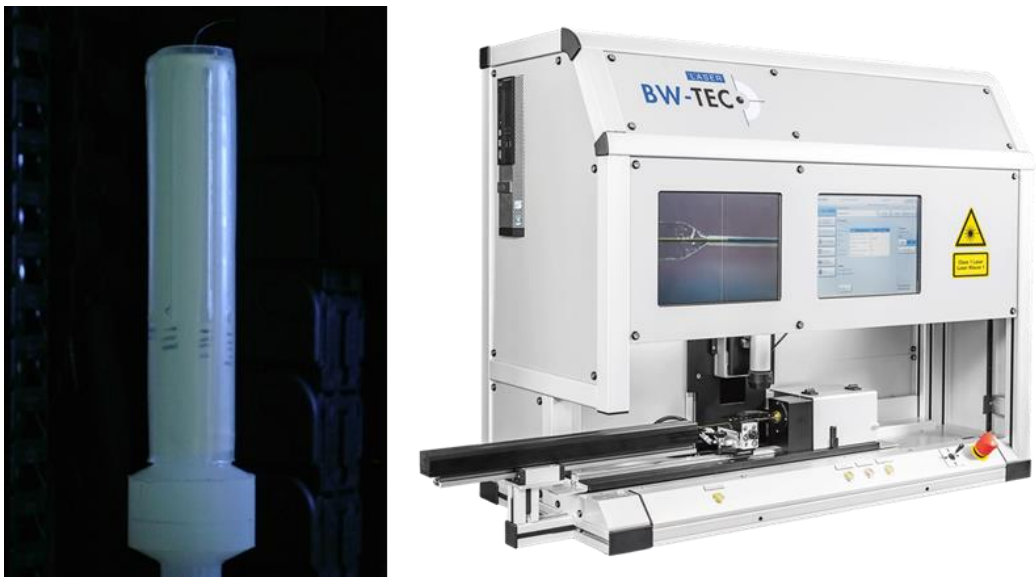

*Figure 43: Delrin mandrel with scaffold and heat shrink on used for laser bonding experiments (**left**), BW-Tec CO_2 bonding laser (Type 1410) used to test laser bonding (**right**)*

4.1.3.3. Ultrasonic welding

Ultrasonic welding makes use of locally applied ultrasonic vibrations to create a joint between two materials and can be used to join dissimilar materials. Feasibility of ultrasonic welding was tested using a Branson LPX ultrasonic platform (Ultraplast, Johannesburg, South Africa) with a PT-350 hand-held welder. The operating frequency was 20 kHz while the output power was 0.15 kW. Pressure, using the welder, was manually applied to 1) a scaffold placed on a flat CarboSil 80A film and 2) a scaffold placed around a pre-coated stent. The weld horn translates the amplitude of the frequency and by design focusses the vibrations, yielding the weld with the applied pressure (see Figure 44).

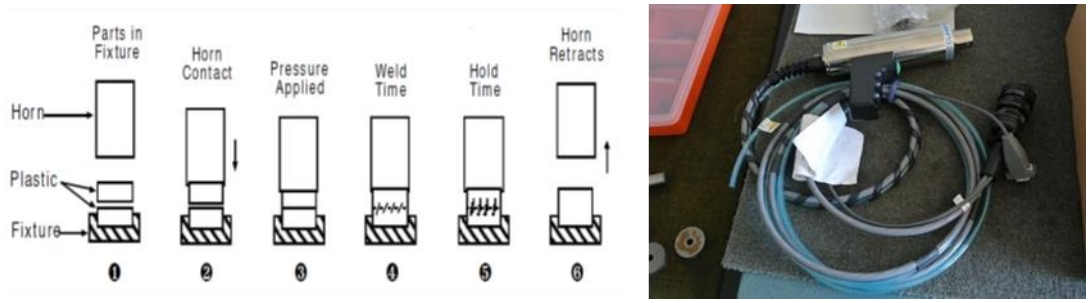

*Figure 44: Schematic representation of ultrasonic bonding process (**left**) and photograph of handheld PT-350 welder used to do ultrasonic bonding tests (**right**)*

4.1.3.4. Conductive Heat bonding

Conductive heat bonding is achieved by bringing two substrates (film and scaffold) into contact above their melting points and applying pressure to fuse the layers. Conductive heat bonding of the scaffold was utilized in several embodiments within this project.

i. Hotplate rolling

Initial heat bonding was done by placing a scaffold onto a coated stent and rolling the combination on a mandrel across a hotplate at 200 °C (see Figure 45 **A**).

ii. Localized welding

Alternatively, a temperature controllable Magnum 2004 soldering iron station (Communica, Cape Town, South Africa) (see Figure 45 **B**) was used to manually apply localized heat and pressure to bond the scaffold to the stent (after placing a scaffold onto a coated stent). A light source was placed behind the stent-scaffold combination while bonding, to make the struts visible behind the opaque scaffold. A chisel tip was used at a temperature ranging between 170 – 180 °C.

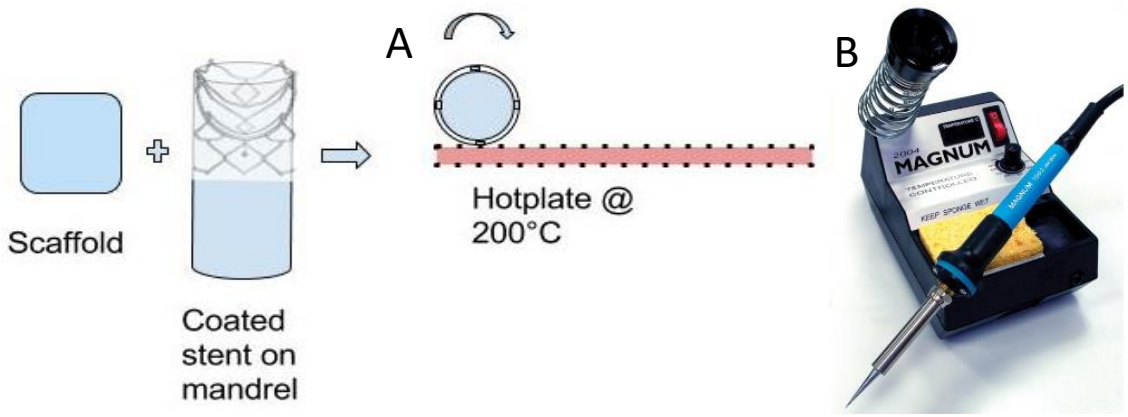

*Figure 45: Schematic representation of flat plate bonding (**A**) and image of Magnum 2004 soldering iron station used in manual bonding (**B**)*

iii. Semi-automation of conductive heat bonding

Semi-automation of the process was realized by designing and manufacturing bonding rigs based on two counter-rotating tubular mandrels rolling against each other. As a proof of concept, laser cut stent tools with additional support structures were placed over an aluminium mandrel to create a rolling pin (see Figure 46 **A**) with a raised surface. The required heat was applied using a Bunsen burner (see Figure 46 **B**) and feasibility was tested by rolling the heated pin over a scaffold-film assembly.

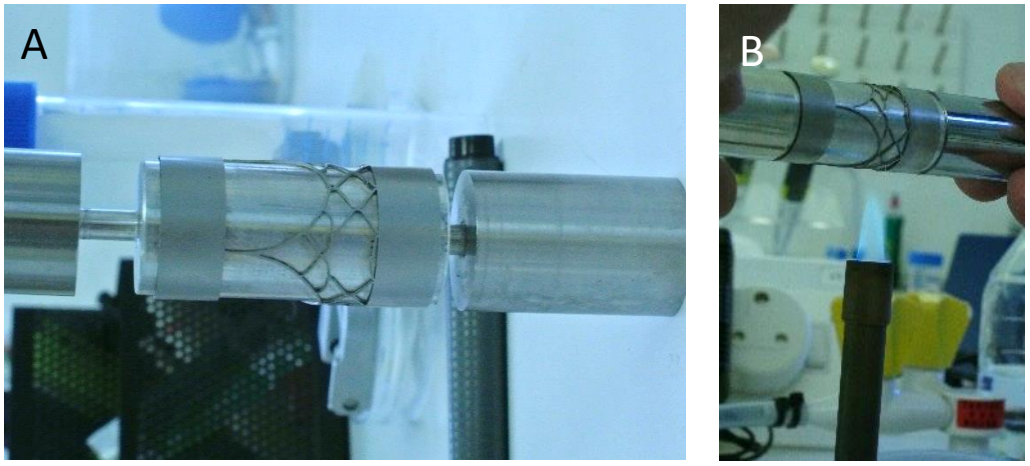

*Figure 46: Rolling pin with stent tool (**A**) and using a Bunsen burner to apply the required heat for bonding (**B**)*

From this initial experiment, the first bonding rig prototype consisted of (**1**) two tubular mandrels, one holding the stent-scaffold combination and the other mandrel the laser cut bonding tools, heated from the inside using a (**2**) 200 W cartridge heater (Thermon, South Africa) (see Figure 47). The base and support structures were manufactured from 10 mm thick (**3**) laser cut steel plates while the mandrels connected to shafts were rotated using (**4**) gears and a handle. The mechanism ensured that when the mandrels mate for the bonding

process they were only in contact for one full revolution, after which they automatically disengaged. The engagement/disengagement was controlled by a (**5**) drop shaped cam.

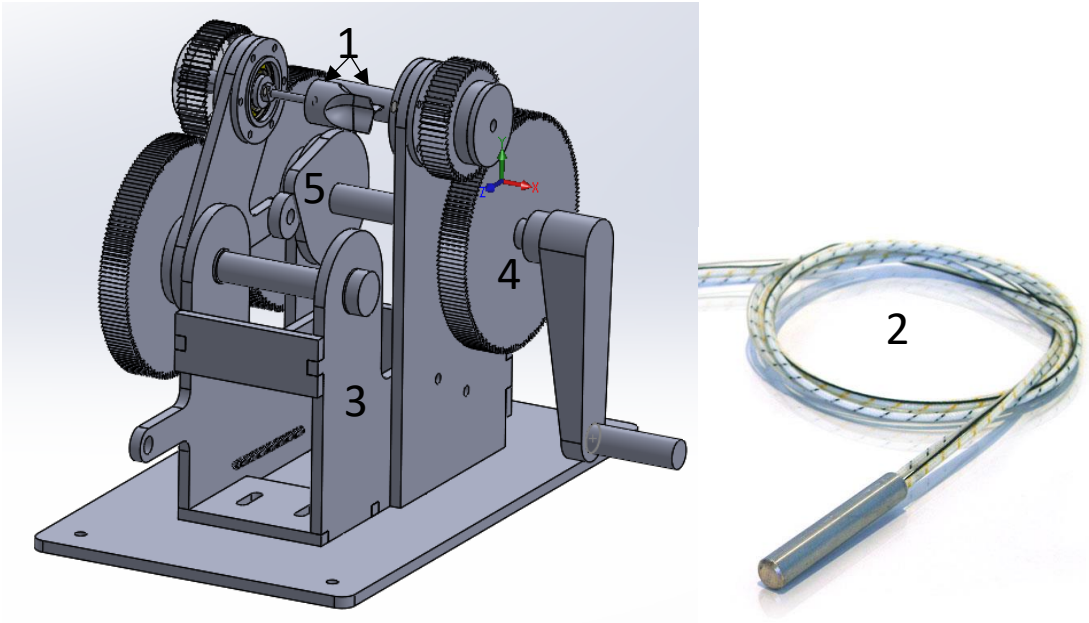

*Figure 47: Rendering of 1st prototype of bonding rig (**left**) and an image of the 8mm heater cartridge used in bonding rig (**right**)*

A second iteration was designed to improve on some of the aspects of the first prototype (see Figure 48). It functioned using the same concept of (**1**) two rollers mating via (**2**) gears. In this case the gears were mounted on (**3**) sliders within (**4**) vertical guiding columns.

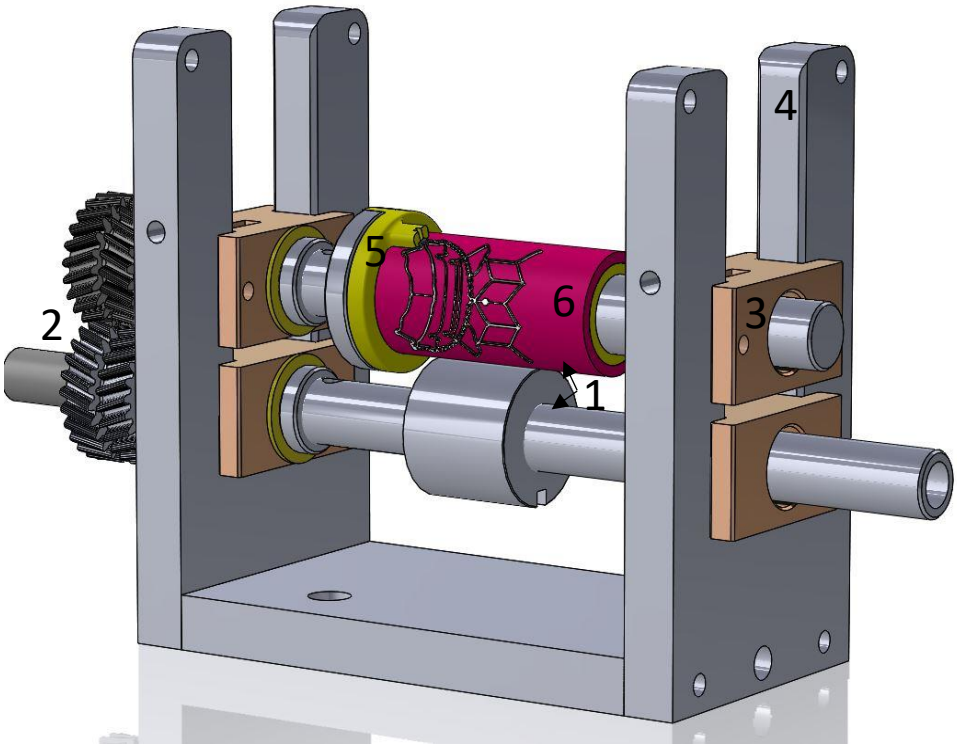

Figure 48: Rendering of 2nd iteration of bonding rig

A (**5**) 3D printed sheath with inherent keys were used to house the stent-skirt combination. The sheath had two keys, one that slots into the rig while the other correctly aligns the stent in an axial direction. For improved circumferential contact during the bonding cycle, a (**6**) silicone sleeve was added between the stent-skirt combination and the printed sheath. Temperatures were set to between 140 – 180 °C using a Gefran temperature controller (Thermon, South Africa).

4.1.4. Skirt bonding patterns and filling mechanisms

Four different skirt types (FLAT, H-FFF, H-NF and H-BFF) were manufactured by attaching scaffolds to pre-coated stents with localized conductive heat bonding using the soldering iron. All skirts were bonded to the abluminal side of the stent. The skirt designs can be categorized into single (FLAT) and double layered (H-FFF, H-NF, H-BFF) skirt.

The FLAT skirt comprised a flat tubular scaffold bonded to all struts below the scallop and the first arm above the scallop (see Table 12). After bonding, excess scaffold was trimmed away.

Both the first and second layer of the dual layered skirts consisted of a single spun tubular scaffold. The scaffold was inverted, and a flat area was bonded as the first layer. An optional flap layer was added in the case of the H-FFF skirt, before the scaffold is inverted to bond the second layer (see Figure 49).

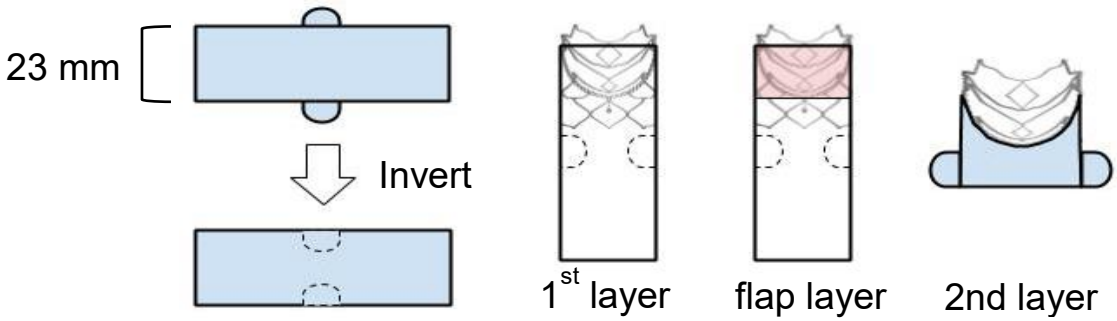

Figure 49: Schematic representation of dual layered skirt bonding

The HUMP FORWARD FLOW FILLING (H-FFF) skirt comprised of two layers which created a (**1**) bladder with an (**2**) opening on the luminal side of the skirt. This opening was covered by a (**3**) one-way flap that allowed blood to fill the bladder during systole (**4**) (see Figure 50). The first layer was bonded on all struts below the scallop as well as the first arm above the scallop, while the flap and second layer were only bonded along the scallop (see Table 12).

The HUMP NO FILLING (H-NF) skirt comprised two layers without any filling mechanism. The first layer was bonded along the scallop and the bottom row of the stent with the second layer bonded along the entire scallop (see Table 12).

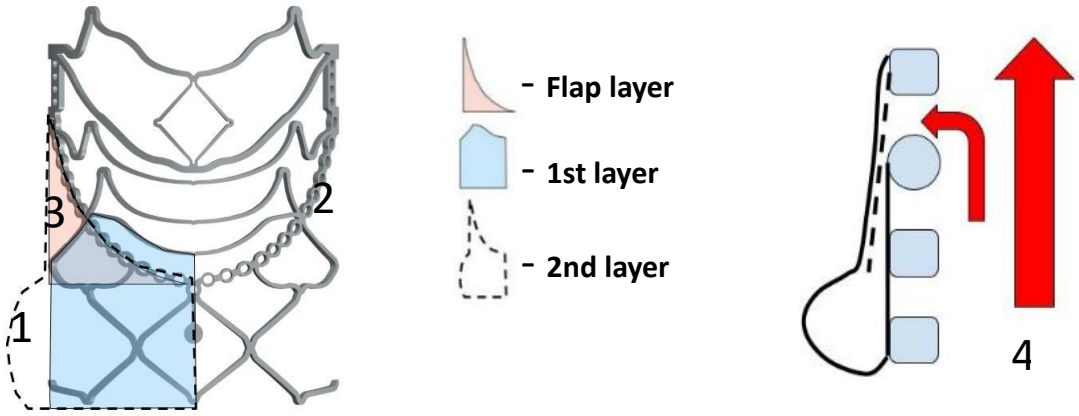

*Figure 50: Schematic illustration of H-FFF skirt, showing cross-sectional view of different layers (**left**) and representation of filling mechanism (**right**)*

The HUMP BACK FLOW FILLING (H-BFF) skirt comprised two layers which created a (**1**) bladder with an (**2**) opening on the abluminal side of the skirt, located between leaflets. The opening allows blood to enter the bladder during (**3**) diastole (see Figure 51). The skirt was bonded on the scallop and bottom row in the first layer, and partially on the scallop on the second layer. (See Table 12)

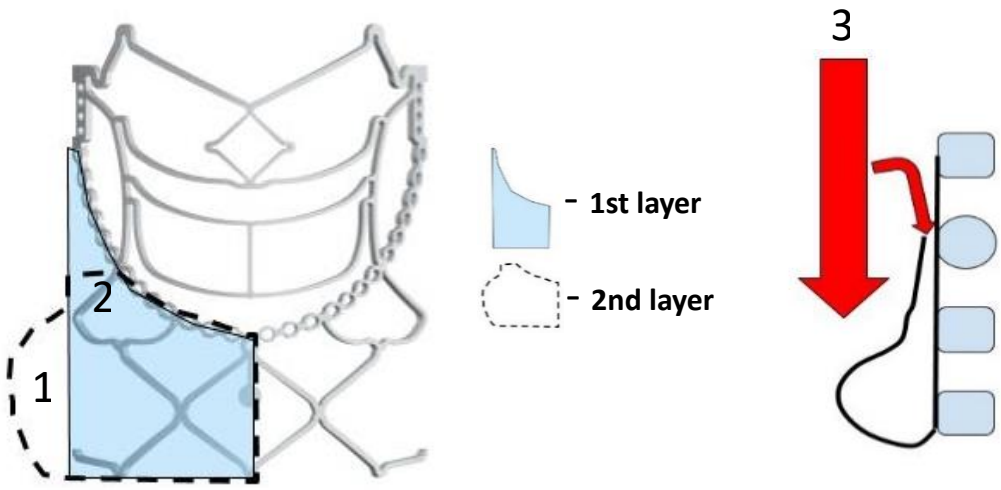

*Figure 51: Schematic illustration of H-BFF skirt, showing cross-sectional view of different layers (**left**) and representation of filling mechanism (**right**)*

Table 12: Bonding patterns of four skirts indicated by dashed red lines, showing individual layers

SKIRT	Layer 1	Flap layer	Layer 2
FLAT		**N/A**	**N/A**
H-FFF (Hump-forward flow filling)			
H-NF (Hump-no filling)		**N/A**	
H-BFF (Hump-back flow filling)		**N/A**	

4.1.5. Quantification of Attachment strength

4.1.5.1. Finite element analysis (FEA)

Crimping of the stent leads to overall lengthening, with sets of points (A – I) undergoing differing amounts of displacement (see Figure 52). The crimped profile of the stent was determined using a commercially available FEA package (ABAQUS, 2016, Dassault Systèmes, Providence, USA). The symmetry of the stent was exploited to minimize computational time and consequently only one third of the stent was modelled (see Figure 52) using an elasto-plastic material model based on uniaxial tensile tests.

A virtually modelled crimper consisting of 12 plates was used to radially reduce the diameter of the stent. From the 12 radially moving analytical rigid body plates, only 5 were used to model one third of the crimper. The stent was discretized with hexahedral elements that were found suitable as it focused on the deformation of the stent and not the stress analysis. Crimping mandrels used to provide stable controlled crimping were modelled as analytical rigid bodies.

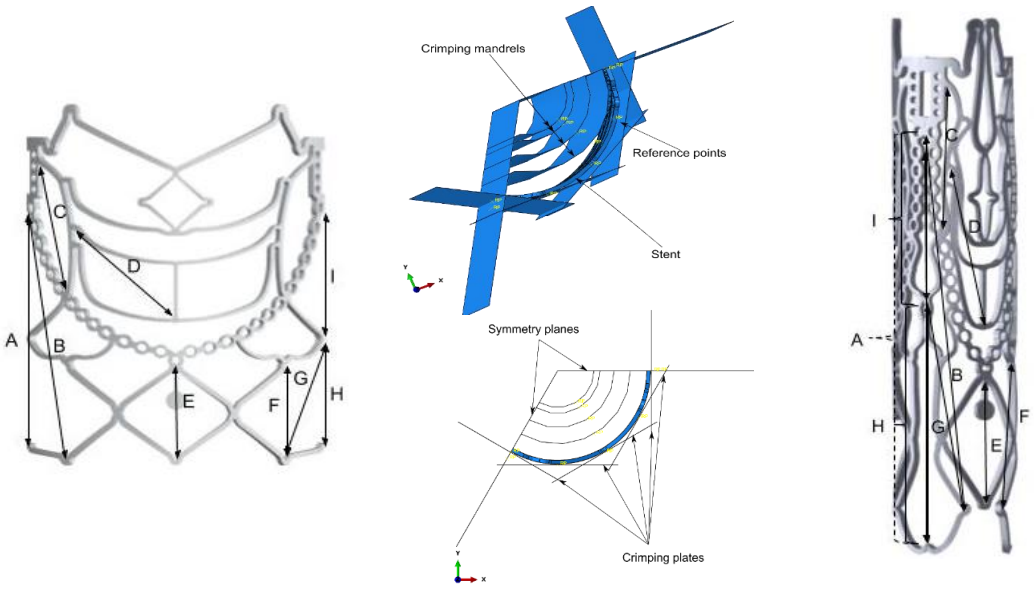

*Figure 52: Rendering of one third of the stent at the as-cut (**left**) and crimped (**right**) diameters, showing points A-I and their relative displacement, Schematic representation of crimper plates and crimping mandrels (**middle**)*

A general contact model (Abaqus Analysis User's Manual, Volume 5) was used to simulate contact between the virtual crimping plates and the stent as well as between the stent and other parts of the stent (self-contact). Based on the amount of deformation and the contact model, the ABAQUS explicit solver with a cylindrical coordinate system was used. The end faces of the stent were fixed in the circumferential direction but allowed to move radially. Furthermore, to prevent rigid body motion the stent was fixed axially at one node just below

the nadir of the stent. The stent was crimped from the as cut (23 mm) to crimped (8 mm) diameters. The model was validated by looking at the effect of the element type, by performing a mesh convergence study and by investigating the effect of mass scaling on the solution. The model was further validated with physical tests including dimensional verifications.

FEA was also used to investigate the effect of physiological pressure on two different critical areas of the stent (see Figure 53).

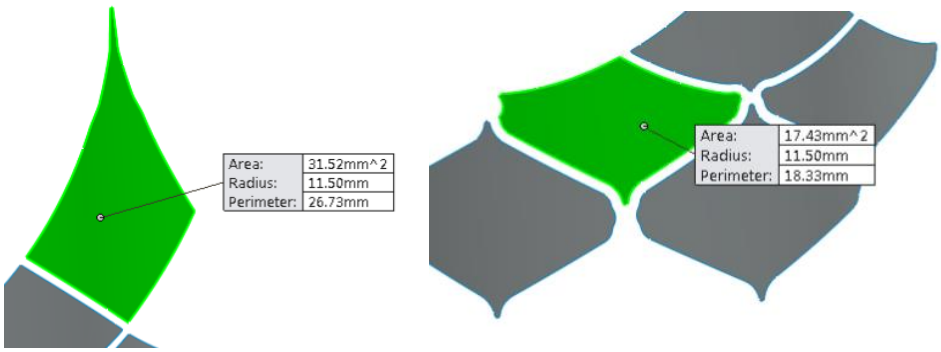

*Figure 53: Images of identified critical areas investigated by FEA: big (**left**) and small (**right**) diamond shaped elements with respective area and perimeter values*

The diamond shaped skirt sections (below) were modeled at a thickness of 94 µm, with shell elements for the identified diamond shaped elements (see Figure 54).

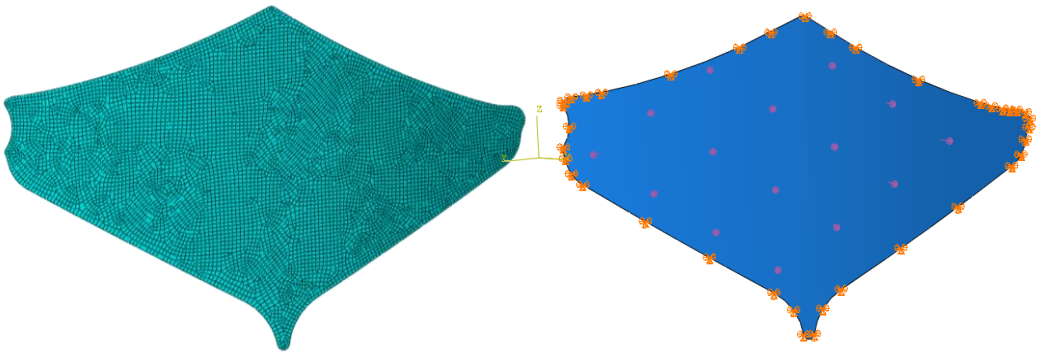

*Figure 54: Meshed geometry of small diamond with quadrilateral elements (**left**), Boundary conditions (orange highlights) and load applied (purple highlights) on small diamond (**right**)*

The attachment of the skirt to the stent was simulated by fixing the edges of the skirt in all directions (see Figure 54, orange highlights). A pressure of 140 mmHg, using a smooth function, was evenly applied across the element (see Figure 54, purple highlights). An Ogden model based on uniaxial tensile test was used for the skirt material model. Furthermore, the large deformation required the use of an explicit solver. For further explination of material properties, the contact model used, mesh topology, and boundary conditions, refer to the Appendix.

4.1.5.2. Debonding tests

i. Micro-tensile pull-off test

To experimentally quantify attachment strength, various pull-off tests were performed by attaching electrospun scaffolds by means of localized welding to either pre-coated stents or custom-made pull-off rings. By attaching half a micro-tensile specimen (ASTM D 1708) of scaffold (n=4) to a pre-coated stent, initial pull off tests were performed in a uniaxial tensile tester (12 mm/min). The stent-specimen combination was suspended on a bent metal rod and the scaffold was fastened in the grips (see Figure 55 **B**). Full micro-tensile specimens (n=2, PARA and PERP) were pulled to tensile failure as controls.

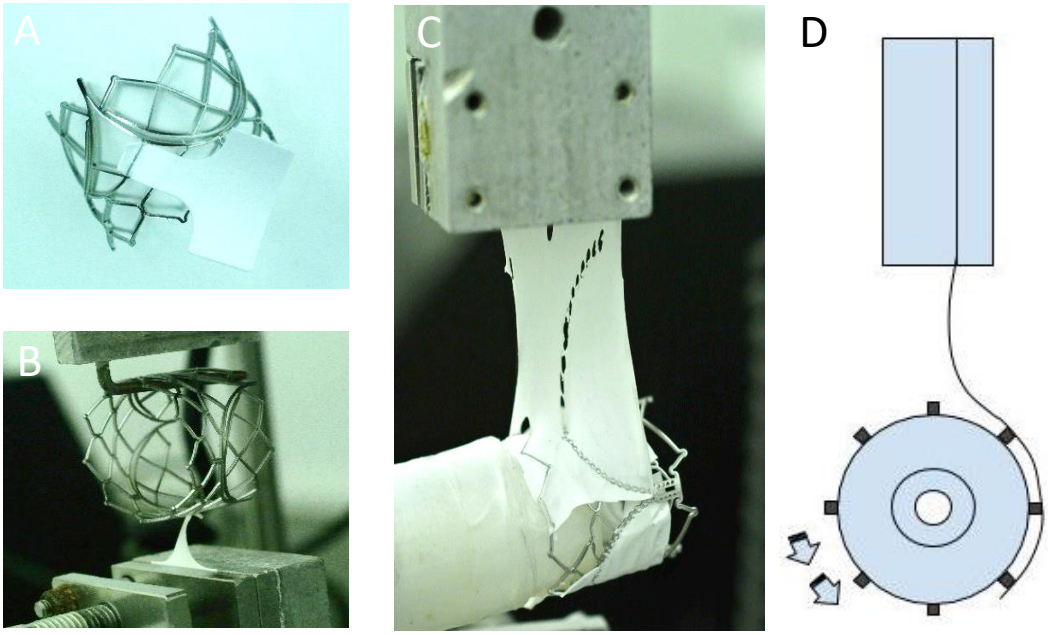

*Figure 55: Photographs and schematic of stent pull off tests; showing half a tensile specimen attached to a pre-coated stent (**A**) and the resultant test in an Instron (**B**). Also showing a rectangular specimen being pulled off a stent (**C**) and the schematic representation of the test (**D**)*

ii. Bonding pattern pull-off test

Further pull off tests were done by attaching rectangular electrospun scaffolds (n=2, PARA, *ca* 60 x 20 mm) to one third of a coated stent with 2 differing bonding patterns (layer 1 of H-NF and layer 1 of FLAT, see Table 12) and pulling it at 12 mm/min while the stent was mounted on a polyacetal mandrel on a bearing (see Figure 55 **C** and **D**). Both micro-tensile and bonding pattern pull off results are reported as force (N) versus extension (mm).

iii. Ring pull-off test

In a third method, specimens were attached to pre-coated MP35N rings (see Figure 56)(n=3) that could be clamped in the tensile tester. The rings had 5 mm long bonding struts, similar in thickness to stent struts (300 µm), to which flat tubular scaffolds (90 µm) were attached and excess scaffold was marked and cut to create 4 specimens per ring (see Figure 56). Three different pre-coating thicknesses (30, 120 and 180 µm) were evaluated and results are reported as stress (MPa) vs strain (%).

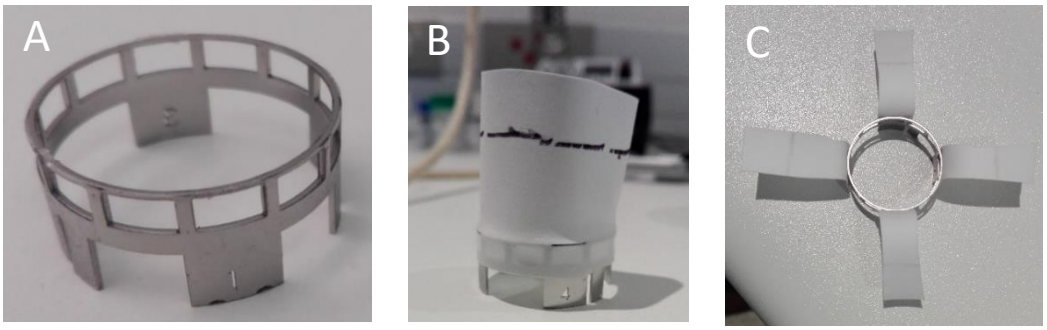

*Figure 56: Photographs of ring pull off tests showing the ring with bonding struts and gripping area (**A**), the marked tubular scaffold with 5 mm bonds (**B**) and after excess scaffold has been trimmed and sample is ready to be tested (**C**)*

4.1.5.3. Fatigue testing

The effect of constantly pulsating physiological pressures on the attachment of the scaffold to the stent was investigated by placing a valve with a FLAT skirt in a VDT-3600i Heart Valve Accelerated Wear Tester (BDC Laboratories, Wheat Ridge, CO). The valve experienced accelerated (15 Hz) opening and closing at a diastolic back pressure of 100 mmHg (see Figure 57).

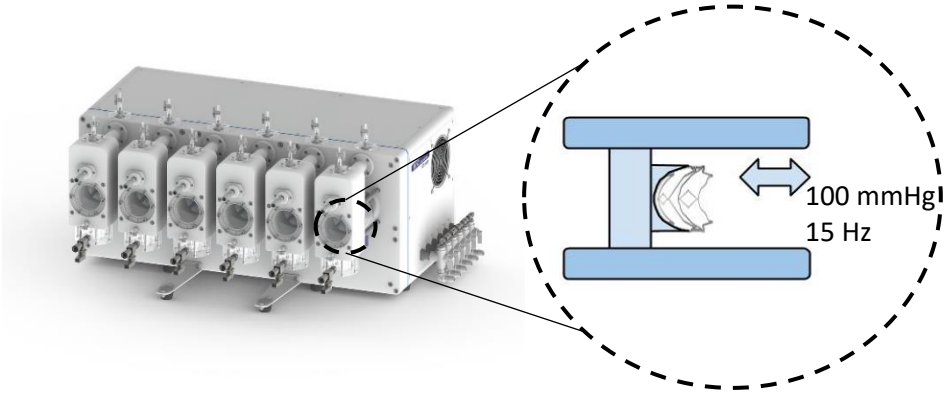

Figure 57: Image of BDC Laboratories VDT-3600i Heart Valve Accelerated Wear Tester with magnified schematic view of a single test compartment

4.2. Results & Discussion

4.2.1. Stent preparation

During laser cutting, considerable heat is generated and recast slag and heat affected zones lead to an unwanted surface finish of the stent. (Liu, Li, Tong, & Zhu, 2017) (see Figure 58 **A**). Successful pickling and electropolishing removed 14 – 20 wt% material from the stent, rounded the edges and yielded a smoother surface finish as can be seen by visual observation (see Figure 58).

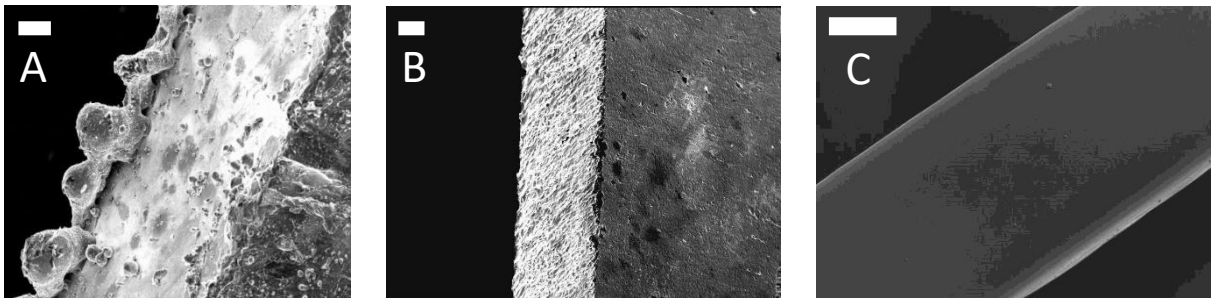

*Figure 58: SEM images of as cut (**A**), pickled (**B**) and electropolished (**C**) stent struts*

A smooth stent surface finish is desirable since irregularities can lead to coating imperfections and potential sites for crevice corrosion to initiate. Successful pre-coating yielded a stent fully encapsulated with polyurethane. The coating coalesced in a slightly thicker abluminal pre-coating layer compared to the luminal layer (see Figure 59). The phenomena of a thicker abluminal layer can be explained by a shielding effect the struts have while being pre-coated, resulting in less material reaching the inner stent surface.

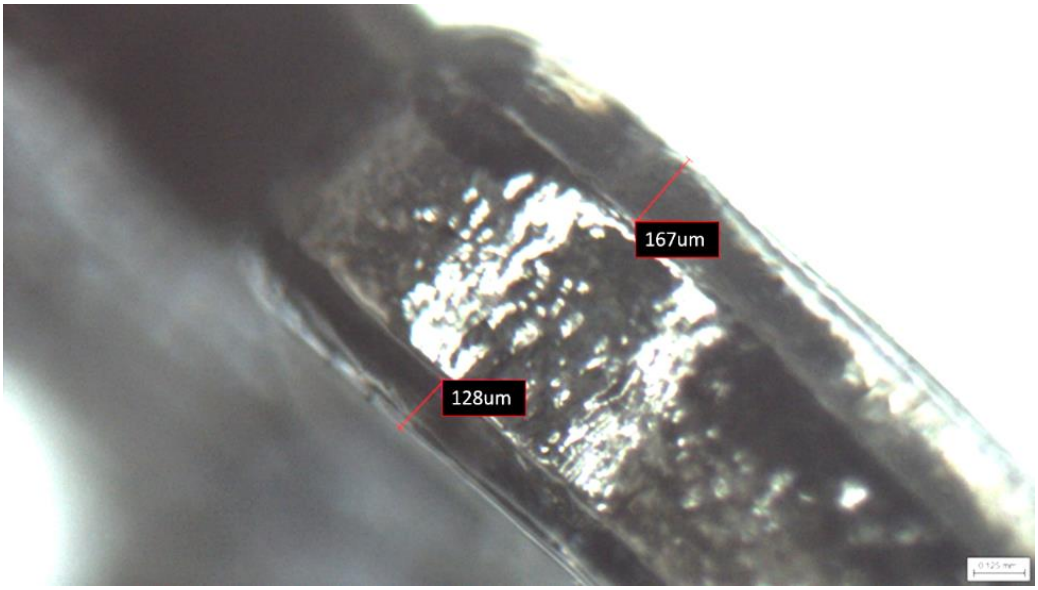

Figure 59: Microscope image of stent from above, showing coating thickness of the luminal and abluminal layers with measurements taken using IC Measure

4.2.2. Bonding

4.2.2.1. Direct spinning and solvent bonding

Direct spinning onto a completed polymer valve (inherent film skirt and stent) resulted in different scaffold morphologies in the space between the struts compared to on the struts. Scaffold fibers aligned along the struts while they were more randomly orientated in the windows (see Figure 60). This was attributed to the electroconductive nature of the stent struts, creating a template that directed the deposition of the electrospun fibers. Similar observations have been reported by groups investigating cell penetration into electrospun scaffolds and topological engineering of scaffolds for micro-manufacturing applications (Vaquette & Cooper-White, 2011; Y. Wu, Dong, Wilson, & Clark, 2010). The shielding of the electrostatic force by the inherent film skirt of the polymer valve may also have reinforced this preferential deposition.

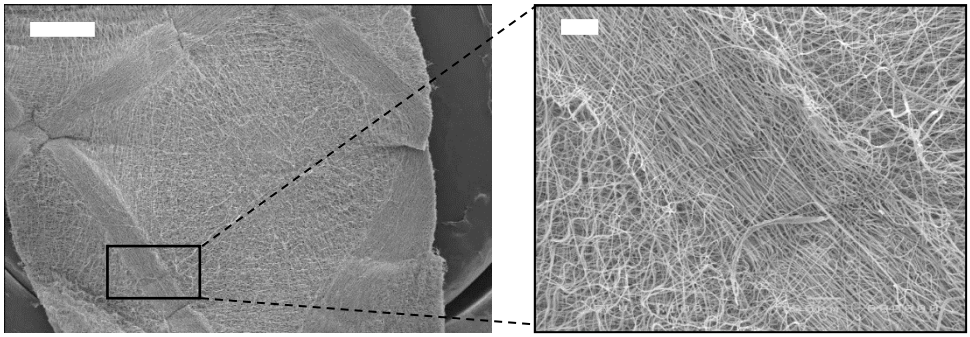

Figure 60: SEM images showing fibers preferentially aligning along struts. The white bars represent 1mm and 100 µm respectively

The lack of attachment observed when crimped to a final diameter of *ca* 8 mm can possibly be explained by fibers landing dry during the first attempts of spinning onto the valve (230 mm tip to collector distance, see Figure 61). Detachment did not occur between specific sets of points with low displacement relative to each other. Dry landing of fibers however, did not yield overall adequate attachment strength.

*Figure 61: Macro photographs showing resulting product of spinning onto finished valve (**left**), detachment of skirt when crimped onto balloon (**right**)*

Fibers landing wet on the valve resulted from the decreased tip-to-collector distance which led to slightly improved adhesion of the scaffold to the stent when fully dried. The application of pressure, required to further improve attachment was not possible on the rotating mandrel. In addition, when wet spinning is attempted, the porosity of the scaffold is lost due to the amalgamation of fibers. Although wet landing can increase adhesion, it also increases the modulus of the resulting film-like scaffold, thus requiring more force to elongate while crimping which could lead to stent deformation.

Direct solvent bonding using a scalpel blade to deposit the solvent and apply pressure resulted in successful bonding, however the low surface tension of the solvent in conjunction with the porous nature of the scaffold led to solvent leaching into the scaffold by capillary action (see Figure 62).

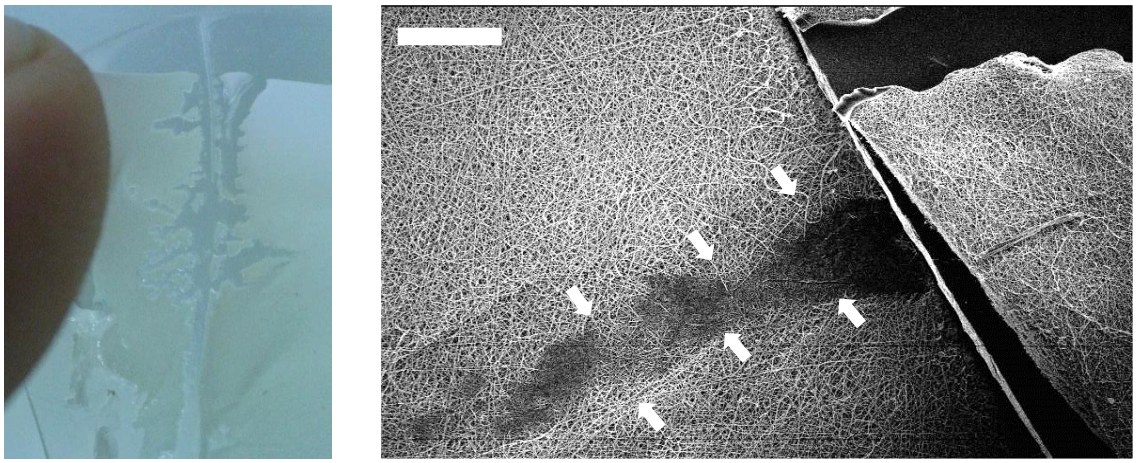

*Figure 62: Macro photograph of solvent leaching due to capillary action (**left**) and a SEM image showing successful solvent bonding (**right**). White arrows indicate bond area. The white bars represent 500 µm*

Stent struts are *ca* 300 µm wide and it was found that reproducibly applying solvent on the correct positions as well the required pressure to achieve adequate bonds was not of sufficient repeatability, and this method of bonding was abandoned.

4.2.2.2. Laser Bonding

By employing a laser to bond the scaffold, successful fusion between the electrospun material and a polymer film (cast and pre-coated) was achieved using laser power above 8W combined with focal distances between 10 -12 mm (see Figure 63 **A** and **C**). The range of bonding times were found to not have much influence on the resulting bonds. Upon closer inspection, the bonds of the scaffold to the film showed a partially fused area between the bond line and the scaffold (see Figure 63 **B**). This gradient is most likely due to the laser focus being less at the edges, which resulted in some fusion, but not full bonds. Attempting

to bond a scaffold directly onto a polymer valve using the same parameters as was used in the film sample, showed successful fusion onto the struts, i.e. between the polymer on the strut and the scaffold. However, scaffold between the struts in the same bond line was cut by the laser (see Figure 63 **C**).

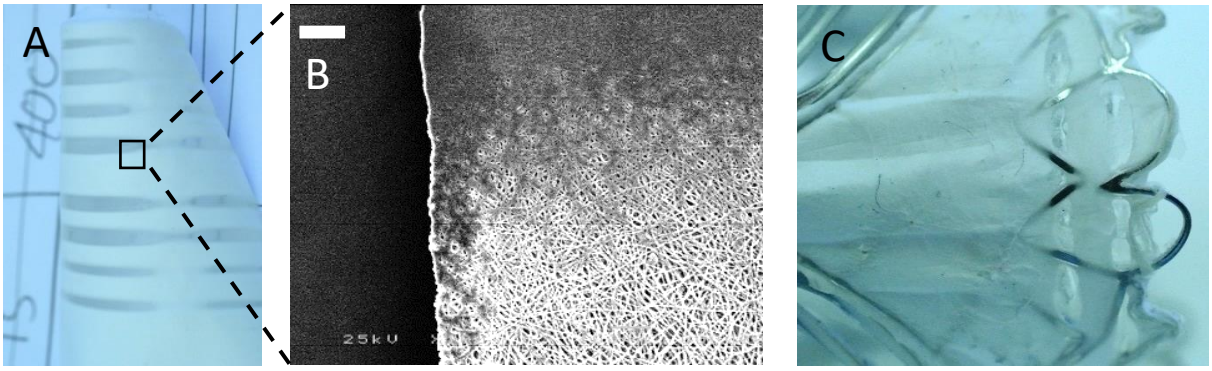

*Figure 63: Macro images of scaffold bonded to film (**A**) with corresponding SEM image showing gradient of fused fibers (**B**) and attempt to bond scaffold directly to stent (**C**). The white bar represents 100 µm*

Despite the encouraging initial results, removal of the heat-shrink tubing, used to apply the required pressure during bonding, often resulted in damage to the sample. This, together with the fact that another laser system would be needed for more complex bonding paths that the equipment was not designed for, laser bonding in its current form was abandoned.

The potential accuracy and reproducibility in combination with the possibility to upscale, make laser bonding an attractive possibility for bonding scaffolds to stents. This however would require machinery that allow z-axis (focal distance) manipulation during the bonding or further software optimization allowing more complex bonding paths to be programmed.

4.2.2.3. Ultrasonic Welding

Ultrasonic welding resulted in some bonded areas between the scaffold and struts and some lacerated areas on the scaffold due to the uneven nature by which pressure was applied (see Figure 64). The surrounding scaffold morphology was observed to be disrupted when compared to normal as-spun morphologies. Even though successful bonds were achieved using the ultrasonic welder, the amount of pressure needed to be applied for bonding was high. The handheld nature of the device in conjunction with the high frequency vibrations made keeping it in place over such a small surface area challenging.

Proposed bonding mechanisms for ultrasonic welding include plastic deformation, recrystallization and melting. Thermo-mechanical bonding is said to occur when the vibrating horn applies pressure and vibrates at ultrasonic frequencies, thereby creating frictional heat

which joins the substrates. Relevant inherent advantages of this bonding method include localized heat generation and not requiring organic solvents.

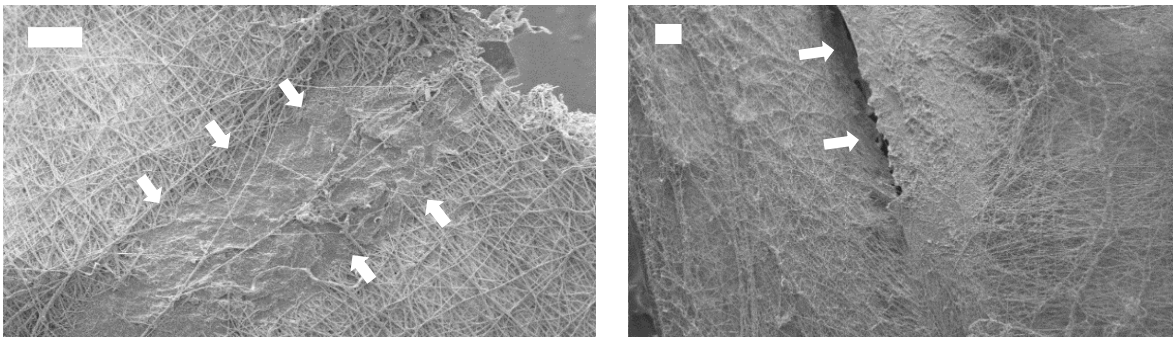

*Figure 64: SEM images of the bond and scaffold morphology after ultrasonic bonding (**left**) and tear formation (**right**). The white bars represent 100 µm respectively*

One option to ensure even application of pressure would be to use stationary benchtop units for bonding. However, irrespective of the ultrasonic unit, intricate weld horn designs would be needed together with an indexing stent fixture system built to accommodate the circular nature of the stent. Another major consideration is that low modulus materials (such as electrospun scaffolds) are difficult to bond via ultra-sonic bonding since they attenuate the vibrations. In general, ultrasonic bonding is more suited to bond rigid materials together.

4.2.2.4. Conductive heat bonding

i. Hotplate and localized welding

Bonding the scaffold to the stent by rolling it across a hotplate was partially successful, but the bonding was uneven due to differential pressure applied over the length and circumference of the valve. The uneven bonding contributes to the detachment of the skirt from the bottom of the stent when crimped (see Figure 65).

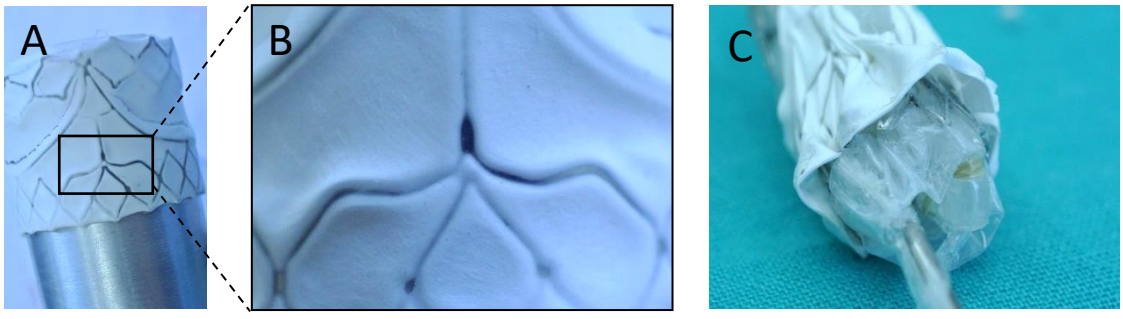

*Figure 65: Photograph of heat bonded scaffold after hot plate rolling (**A**), showing uneven application of pressure (**B**) and scaffold detachment after crimping (**C**)*

This proved the concept of heat bonding and led to further experimentation, specifically the need for more selective and localized application of heat and pressure. The effect of applied heat on strutless areas was a concern.

Applying heat with a soldering iron and bonding the scaffold to the stent yielded bonds that survived crimping and was used for most of the remainder of the study, unless otherwise indicated. Scaffold morphology adjacent to the bonds was mostly undisturbed (see Figure 66). This technique made it possible to bond more intricate patterns as well as the ability to add more than one layer. Limitations of bonding with the soldering iron is that the process is manual and user dependent, leading to variable pressure being applied and thus varied bond strength and uniformity. Although highly adaptable, the inherent user dependability and need for manual input made the process less attractive as a long-term solution.

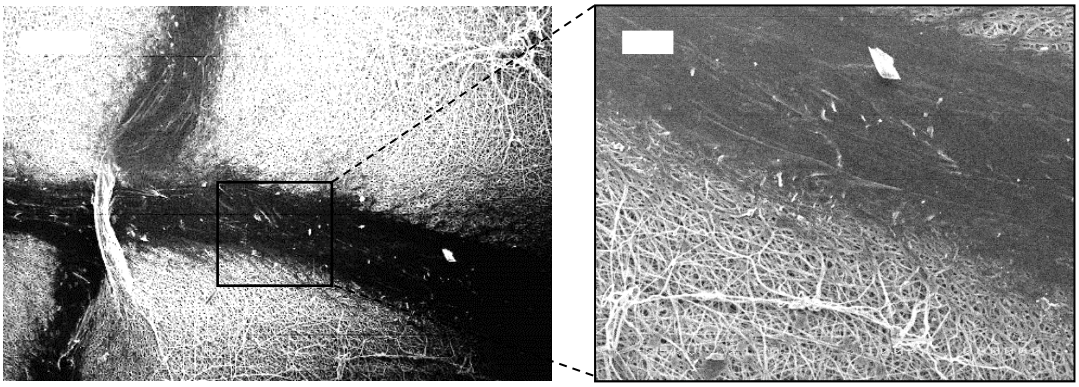

Figure 66: SEM images of bonded area after soldering iron boding. The white bars represent 500 µm and 100 µm respectively

The resulting bonds from using the manually heated rolling pin were adequate where the temperature, time and pressure applied were all ideal (see Figure 67). The uneven bonding could have been due to the heat on the rolling pin dissipating too quickly, unevenly applied pressure or too brief time spent on a certain area. The surrounding scaffold morphology seems undisturbed.

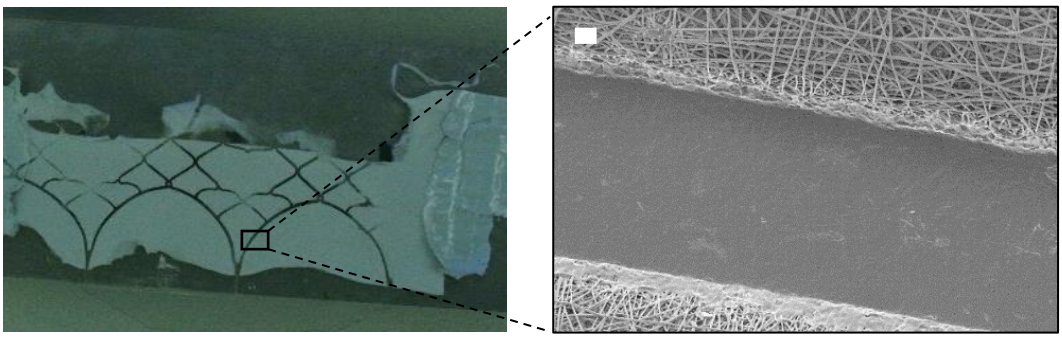

*Figure 67: Macro photograph of scaffold bonded to flat film after initial rolling pin test (**left**), SEM image of boned area (**right**). White bar represents 20 µm*

Positive initial results from conductive heat bonding experiments led to the development of the controlled automated rigs described in the next section.

ii. Semi-automated bonding rig 1

Successful bonds were achieved using this bonding rig when the setup was aligned correctly and the temperature on the Gefran controller was set between 160 – 180°C (see Figure 68 **A**). The machining tolerances needed to successfully bond scaffold to stent struts less than 1 mm in width, were challenging and inherent play within the rig (see Figure 47) limited the accuracy that the two rollers could be aligned with, potentially leading to uneven bonding (see Figure 68 **B**). The cam used to give the device the ability to do one full rotation and then disengage also required fine tolerancing so that intimate contact was made evenly across the surface that was being bonded. Improper contact across the surface lead to uneven bonding. When manual pressure was applied, temperatures as low as 140°C resulted in bonds forming. Misalignment and excessive pressure however led to uneven and misdirected bonding (see Figure 68 **C**). The main drawback however was that repeatable axial and rotational alignment of the skirt-stent mandrel with the bonding tool mandrel was difficult due to the inability to visualize the stent underneath the scaffold. Also, the screw thread used to mount the mandrel, further made alignment variable due to the lack of a reliable fastening mechanism.

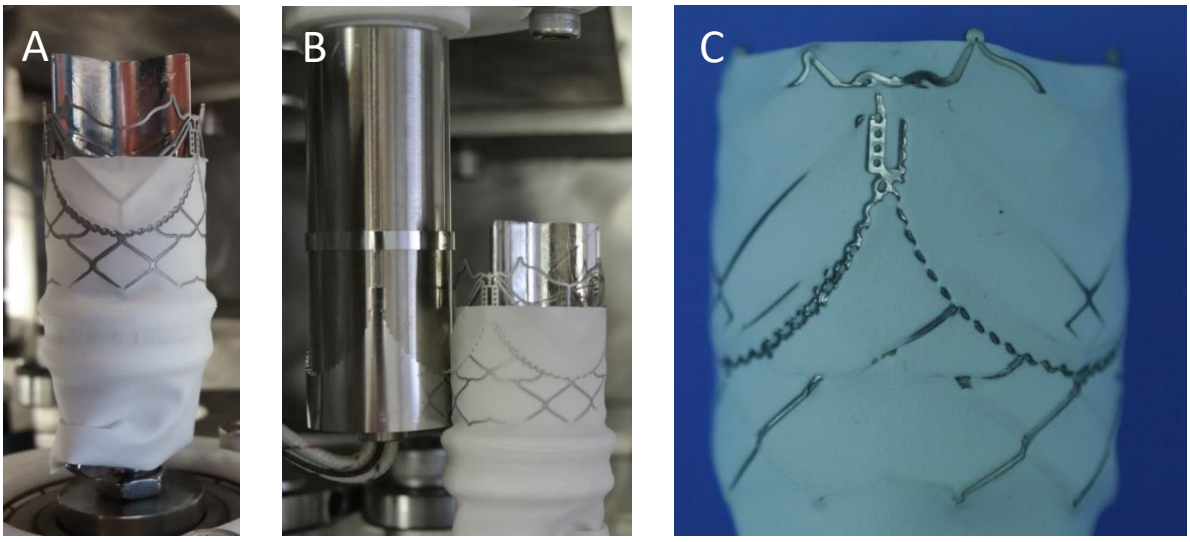

*Figure 68: Photographs showing successful bonding (**A**), uneven bonding due to misalignment (**B**) and uneven misdirected bonding due to excessive pressure (**C**) using the first semi-automated bonding rig.*

iii. Semi-automated bonding rig 2

The addition of the keyed 3D printed sleeve in the second bonding rig (see Figure 48) solved the axial and rotational alignment issues and reduced handling of the stent-skirt combination. The compliance of the added silicone sleeve also compensated for tolerancing and applied pressure variations and solved uneven bonding along the circumference of the stent. (see Figure 69 **A**). This ensured better contact distribution during bonding. The bonding rig was also smaller than its predecessor, making the effect of compounded tolerancing issues less significant.

Drawbacks of this bonding rig include mismatch of mandrel diameters due to material unavailability, a gap in the heating mandrel, limiting the bonding process to one full rotation per step and the lack of a rotation indicator, leading to premature or delayed removal of the stent-skirt combination. Further, the weight of the mandrels was meant to supply the needed pressure for bonding, but it was found that additional manual pressure had to be applied for successful boding. This potentially led to pinching of the scaffold (see Figure 69 **B**).

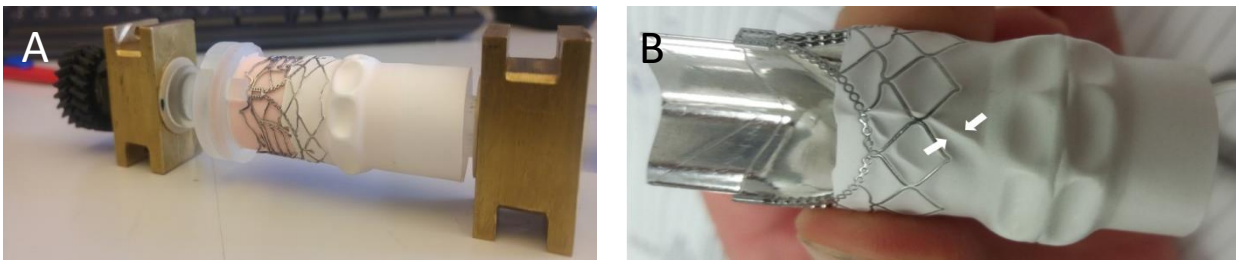

*Figure 69: Photograph of successful bonding (**A**) and pinching (white arrows) of scaffold due to unevenly applied pressure using bonding rig 2 (**right**)*

As is evident from the previous paragraphs, using conductive heat and pressure resulted in the best bond between scaffold and stent considering quality, accuracy and reproducibility of the bond. Automation of this method however proved quite challenging and time consuming and requires more engineering input.

4.2.3. Attachment strength

Strong attachment of the scaffold to the stent is crucial for successful and continued sealing. The skirt is subjected to various forces during its lifetime and should survive crimping, deployment and continuous pulsatile deformation. The direction of the two main forces experienced by bonds can be grouped in either the radial outward direction as experienced during function, or longitudinally, in the direction the stent elongates during crimping.

4.2.3.1. FEA results

Analyzing the strain in the longitudinal elongation direction using FEA on the stent showed dimensions A and H (see Figure 52) to have the largest deformations, with 11 and 9.5 mm respectively. This correlated to 67% and 134% strain for dimensions A and H respectively (see Table 13). As bonds are more likely to fail at larger strain values, debonding during crimping was mainly seen in the FLAT and H-FFF skirts as their 1st layer bonding pattern included dimension H (see Figure 70).

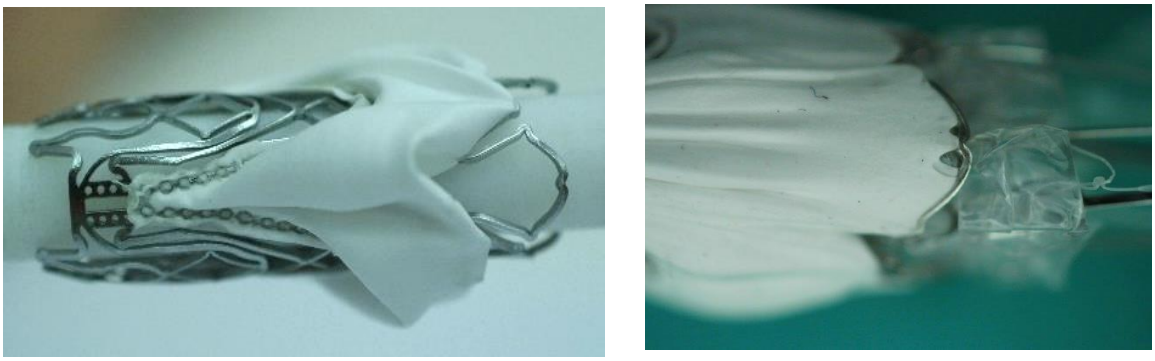

*Figure 70: Photographs showing high (**left**) and low (**right**) levels of bond delamination from the pre-coated stent on areas that undergo the largest amount strain*

This relative difference between dimension A and H and the corresponding strain led to the bonding pattern employed on the H-BFF skirt, namely bonding only to the bottom row of struts and the scallop of the stent. The other stent dimensions were not considered since their percentage corresponding strain was markedly lower than those associated with dimensions A and H.

Table 13: Dimensions of interest (shown on Figure 52) and the relative amounts of displacement they undergo before and after crimping with corresponding % strain values for dimensions A - I

Dimension	Before crimp	Crimped @ 8mm	Difference (mm)	% Strain
A	16.4	27.4	11	67
B	18.1	24.8	6.7	37
C	9.1	9.6	0.5	5
D	9.7	10.8	1.1	11
E	6.8	9.5	2.7	40
F	7.1	10.3	3.2	45
G	8.4	12.4	4	48
H	7.1	16.6	9.5	134
I	8.7	10.9	2.2	25

FEA of individual elements showed the maximum stresses in the radial outward direction experienced by the big and small diamond shaped elements to be 0.60 MPa and 0.35 MPa

respectively at 140 mmHg as calculated for a single layer. Peak displacements of scaffold in the radially outward direction over the big and small diamonds were 1.50 and 0.75 mm respectively. These peak stresses and displacements were experienced in the middle of the element (see Figure 71).

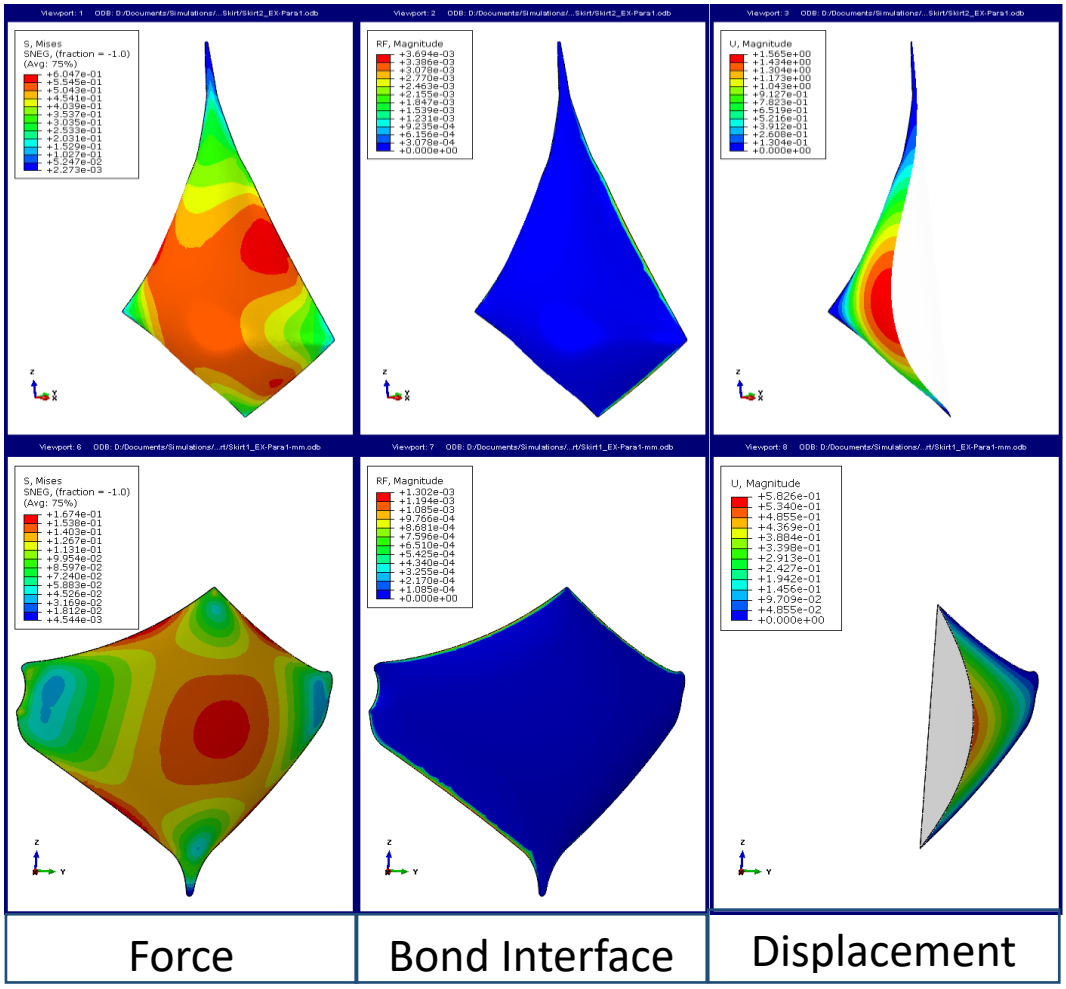

*Figure 71: FEA visualizations of modelled elements (big (**top row**) and small (**bottom row**) diamond) with accompanying stress, bond interface and displacement values experienced by the scaffold.*

The stress experienced at the bond interface due to an applied pressure was 2.2 and 1.0 kPa for the big and small diamonds respectively. The bond interfaces of the bigger diamond element experience double the stress associated with the small diamond element. As these stresses are much lower than the strength of the scaffolds as well as being an order of magnitude lower than what is experienced by the scaffold, the effect of an applied pressure in the pulsating direction on the bond interface of such small elements was not deemed a risk.

4.2.3.2. Debonding test results

i. Micro-tensile specimen pull-off

The pull-off forces in the micro-tensile test ranged from 1.04 to 1.86 N (1.45 ± 0.37 N), compared to the tensile breaking forces of 2.9 N and 3.8 N for the scaffold controls in the PARA and PERP directions. In these pull off tests, the scaffolds did not separate from the stent strut, instead, the scaffold either broke at the bond (see Figure 72, right) or just adjacent to the bonded area (see Figure 72, left). In some instances, the scaffold failed at various places before the bonds failed, indicating that a bond strength higher than the scaffold was achieved. The force required to break the bonded scaffold is however lower than the UTS of the scaffold alone, indicating that the bonding process weakened the surrounding scaffold.

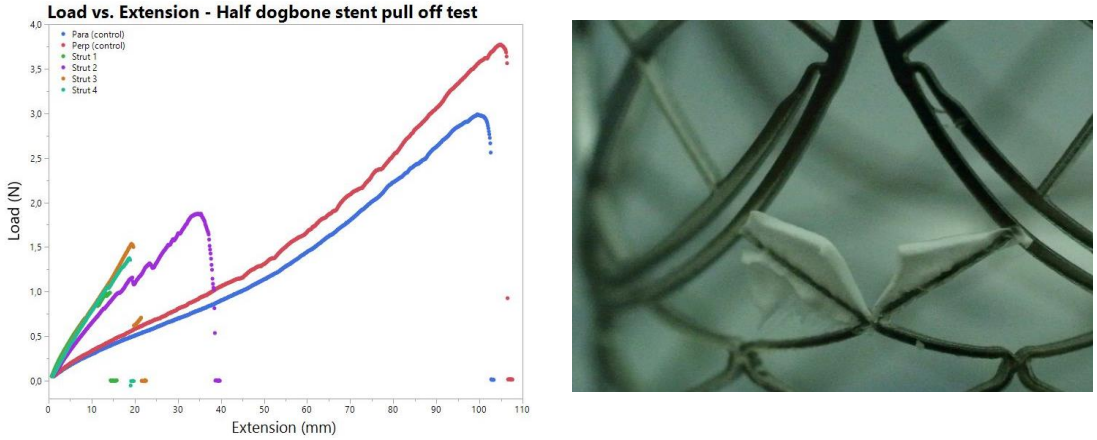

*Figure 72: Graph showing Load vs Extension of pull of test (**left**) and a photograph of failure mechanisms after pull-off test (**right**)*

ii. Bonding pattern comparison

Bonding patterns correlating to the 1st layers of the H-FFF and H-BFF skirts (see section Table 12) showed pull off forces in the same range for both patterns (2.5 - 3 N) (see Figure 73).

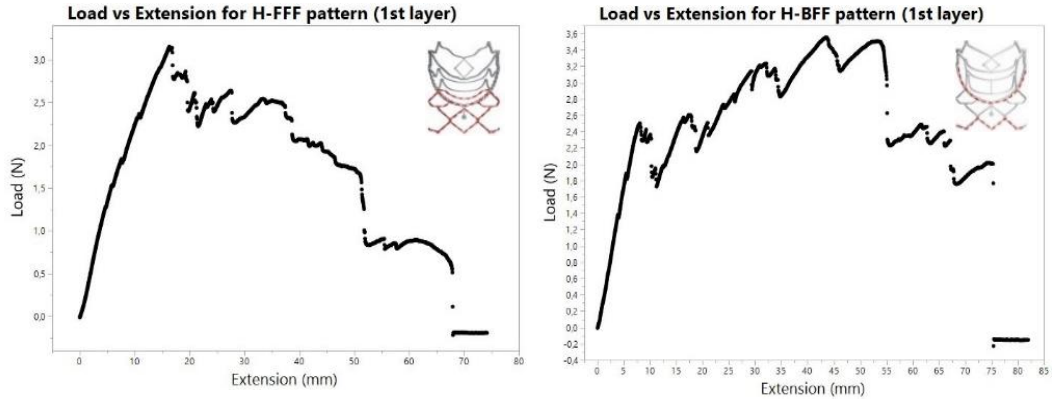

Figure 73: Load vs Extension graphs of stent pull off tests, showing results for two different bonding patterns

Considering the minimum force required to break the bonded scaffold (~1 N) coupled with predicted FEA results (maximum force of 0.6 N), the bond strength was deemed adequate for pull off type forces.

iii. Ring pull-off test

The mean stresses experienced at the bonds in the ring pull off tests were 0.29 ± 0.25, 0.67 ± 0.18 and 1.06 ± 0.08 MPa for 30, 120 and 180 µm pre-coating thicknesses, respectively. On the stress-strain graph, one can see only 33 % of bonds in the 30 µm pre-coating group (blue dots) could withstand more than 67% strain (as indicated by Reference line A, see Figure 74). The bond survival rate increased significantly in the 120 µm pre-coating group with 75% of the bonds surviving more than 67% strain. In the 180 µm group, all bonds survived over 150 % strain. The strain range across which the failures occur show the inherent variation in the bond strength property. The ring pull-off tests evaluated the stresses experienced by the scaffold and bonded area in the longitudinal crimping direction and increased with pre-coating thickness.

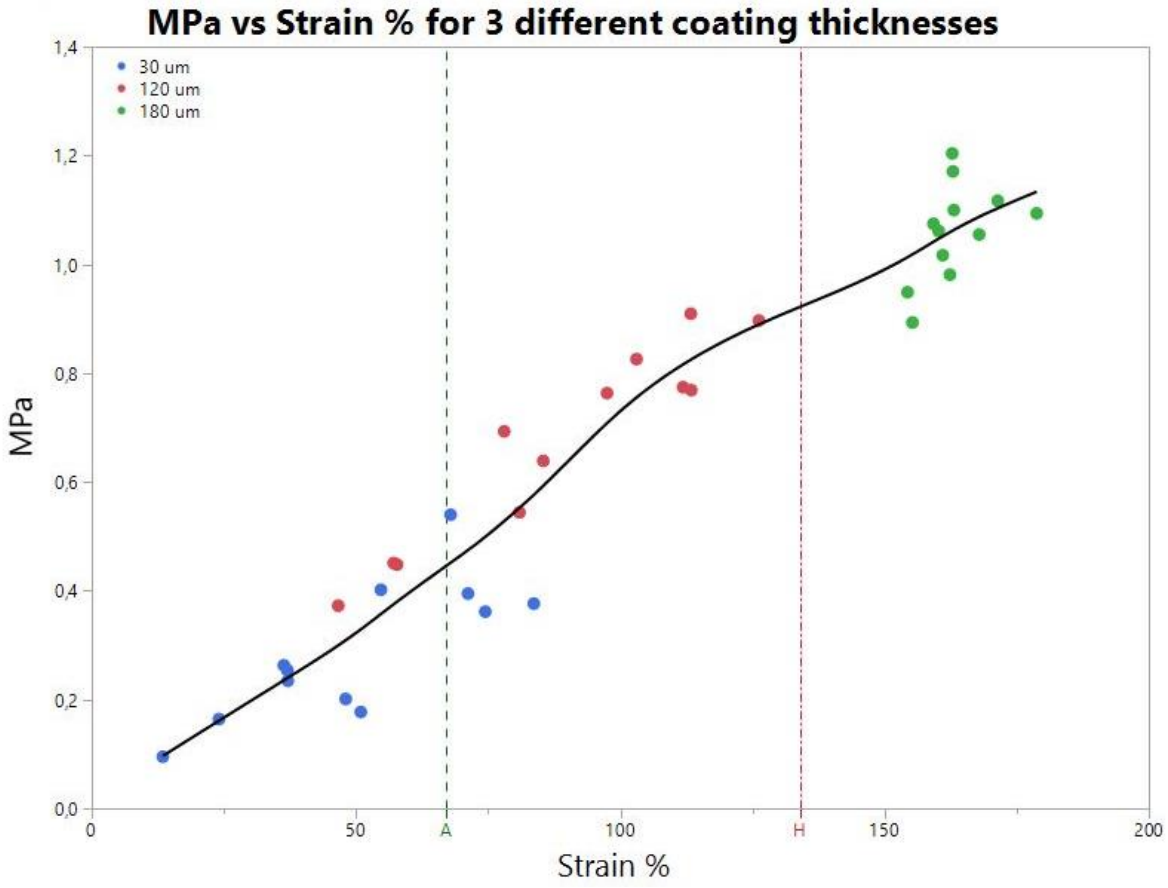

Figure 74: Graph of MPa vs Strain %. Colored markers indicate different thickness groups of pre-coating and reference lines on the x-axis indicate strain that dimension A and H undergo

Different failure modes were observed in the 30 and 120 µm pre-coating thickness groups compared to the 180 µm pre-coating thickness group. Within the 30 and 120 µm groups, specimen detachment was caused by tearing of the sections of the bond area that were adequately fused. The rest of the bond that did not tear, delaminated, indicating inadequate fusion of the scaffold to the pre-coating layer. The number of torn and delaminated areas varied between samples (see Figure 75). Another failure mechanism observed was when the bond failed along its entire length, indicating excessive bonding time. Applying heat on the bond for too long can lead to either the pre-coating or scaffold migrating away from the heat, essentially thinning the bond. As all samples were prepared manually using localized welding, this resulted from operator variability in applying pressure.

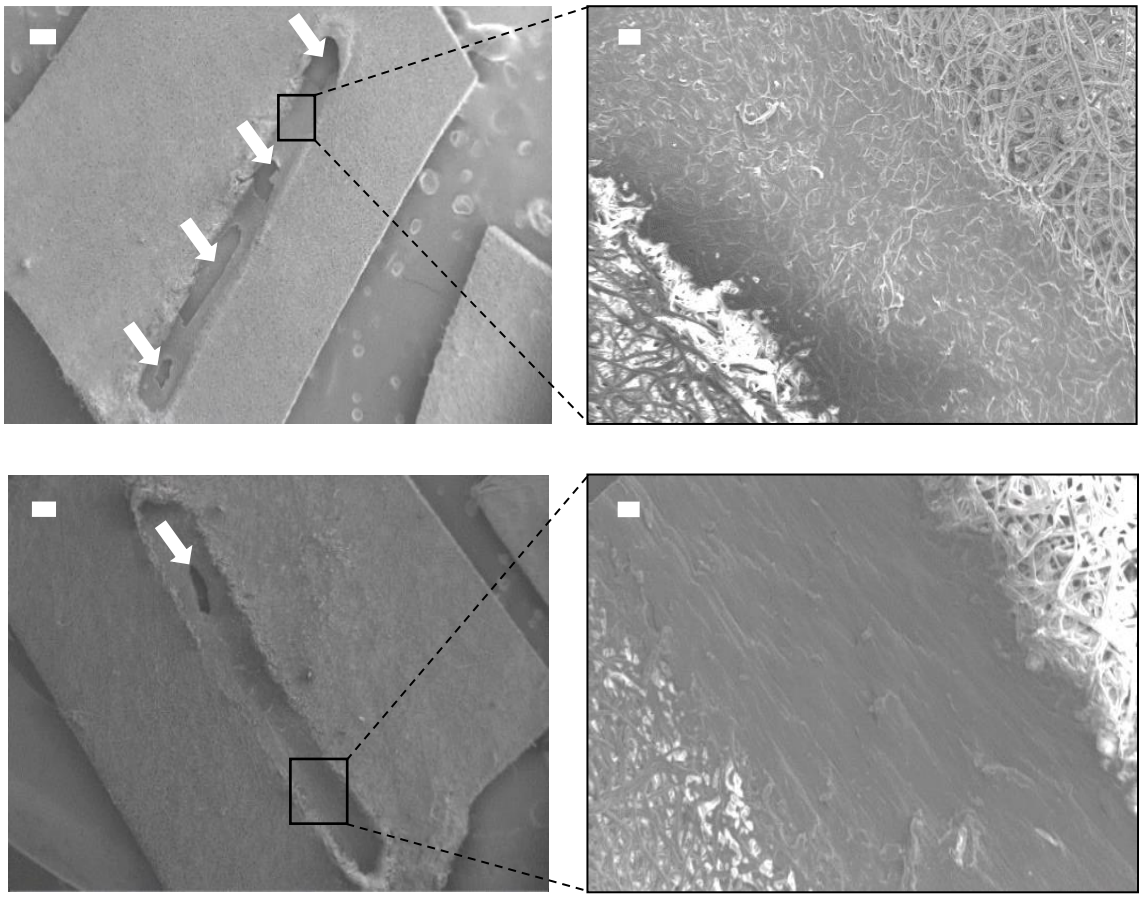

*Figure 75: SEM images of failure mechanism in ring pull-off tests (30 and 120 µm goups). White arrows indicate multiple instances of the bond breaking relative to adjacent areas only delaminating. Prominent level of bond breakage (**top left**) with close-up of delaminated area that was attached to the pre-coating (**top right**). Visible fibers in delaminated area shows insufficient fusion. Low level of bonds breakage (**bottom left**) and close-up of delaminated area that experienced the heat. Fusion is seen to be more complete. White bars represent 200 (**left**) and 20 (**right**) µm*

For the 180 µm group, a different failure mechanism was observed (for all the specimens). Instead of failure or delamination of the bond, the scaffold broke adjacent to the bond after which tearing of the scaffold ensued (see Figure 76), leaving a strip bonded scaffold on the stent. Delamination seen as an imprint at the ends of the bond (see Figure 76), was

observed, indicating the onset of bond failure. This tearing of the scaffold rather than full bond failure indicated that the attachment strength in the crimping direction was higher than the tear strength of the scaffold.

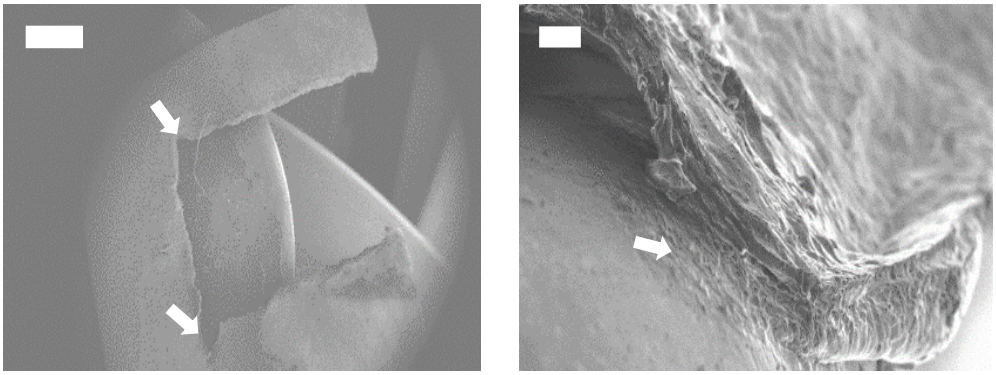

*Figure 76: SEM images of failure mechanisms in ring pull-off test (180 µm group). White arrows indicate the ends of the bond (**left**) and the imprint left after some delamination (**right**). White bars represent 1 mm, and 20 µm respectively.*

From a side on view it could be seen that the bonded area reduced in thickness to a *ca* 20 µm film which fused with the pre-coated layer (see Figure 76). It must be noted that increasing the pre-coating layer thickness may lead to undesirable increase in crimped valve profile dimension.

4.2.3.3. Accelerated wear testing results

The skirt withstood more than 500 million cycles at 100 mmHg in the accelerated fatigue tester, which is equivalent to more than 12 years in the body. The scaffold as well as the bonds survived the continuous flexing caused by the pulsatile pressure. The way the valve was placed in the fatigue tester exposed the area between the scallops (big diamond) to physiological conditions. This could be seen by the fouling of the scaffold in the area between the scallops by contaminants in the driving fluid (water) (see Figure 77). Although this result is from a single valve, it shows the potential durability of the skirt.

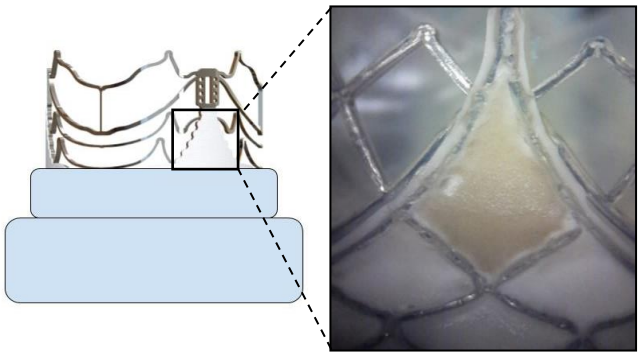

Figure 77: Schematic representation of valve placement within silicone ring with photograph of fouling of scaffold after testing in the accelerated Heart Valve Wear Test

4.3. Conclusion

This chapter described the attachment of electropun scaffolds to pre-coated stents using various bonding techniques, of which conductive heat bonding proved the most successful in terms of reproducibility and accessibility. Further steps to automation of the bonding process have been initiated. Quantification of the attachment strength by FEA and experimental methods led to the improvement of bonding patterns and the identification of ideal pre-coating thickness for good attachment strength. The analysis of failure mechanisms indicated the variability found in the bond as imparted by the manual heat bonding technique. Accelerated fatigue life of bond and scaffold were seen to exceed half a billion cycles.

5. Sealing study

This chapter describes an *in-vitro* test method used to evaluate the paravalvular sealing efficacy of four different sealing skirt designs, two of which had inherent filling mechanisms to aid sealing. After successful scaffold manufacturing (Ch. 3) and skirt bonding, (Ch. 4) pericardial leaflets were sutured onto the cobalt-chrome alloy stent to complete a transcatheter aortic valve prosthesis. Valves were tested within a pulse duplicator (Model: 10647) system using various cast silicone rings to simulate different paravalvular regurgitation (PVR) scenarios. Leakage fractions (LF's) were calculated from the PD data to determine the sealing efficacy of the different skirt designs. Statistical analysis was used to compare the sealing efficacy, followed by discussions of the outcomes.

5.1. Experimental

5.1.1. Materials

Materials used to manufacture the stent and electrospun scaffold have been described in detail in chapter 2 and 3. Ticron sutures (5-0, braided PET) were bought from Medtronic (Minneapolis, USA). Bovine pericardium was sourced from MeatCo (Windhoek, Nambia) and underwent a proprietary chemical treatment that crosslinks the pericardium for use as bio-prosthetic heart valve leaflets.

5.1.2. Transcatheter heart valve assembly

The bio-prosthetic heart valves were assembled in several steps. After stent cutting, pickling, electropolishing and pre-coating, scaffolds were heat bonded to the stent. This yielded stent-skirt sub-assemblies with single scaffold thickness of 100 ± 20 µm which were ready for leaflet attachment. Valves were manufactured by die-cutting treated bovine pericardium into leaflet shapes and suturing them to the stent-skirt sub-assembly along the scallop using the suture holes. Thickness measurements of the pericardial leaflets were done using a Mitutoyo Quick Mini digital thickness gauge. Photographs of complete valves with accompanying renderings and schematically depicted filling mechanisms can be seen in Table 1. The final stent-skirt assemblies were classified by type and shape as FLAT, H-FFF, H-NF and H-BFF (see Table 14).

Table 14: Summary of the different skirt types tested with respective filling mechanisms, renderings and photographs of completed valves

SKIRT	Filling Mechanism	Rendering	Photograph
FLAT	N/A 		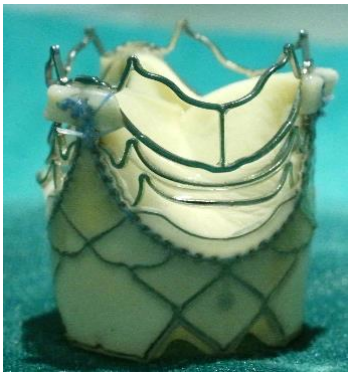
H-FFF (HUMP-FORWARD FLOW FILLING)	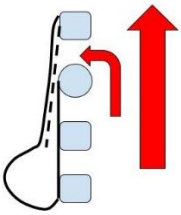	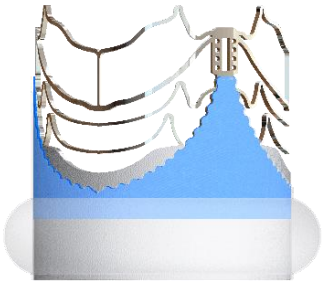	
H-NF (HUMP-NO FILLING)	N/A 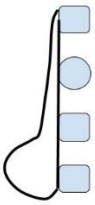	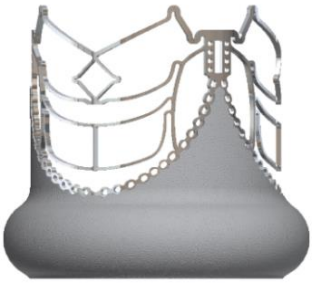	
H-BFF (HUMP-BACK FLOW FILLING)	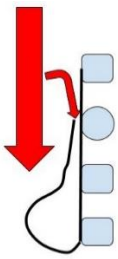	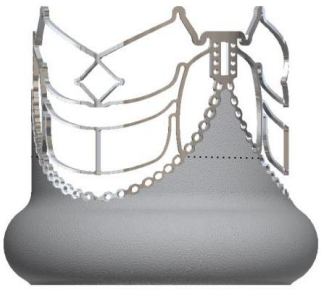	

5.1.3. Test setup and procedure

5.1.3.1. Pulse duplicator system

The pulse duplicator (PD) system (ViVitroLabs, Inc., Canada, see Figure 78) consists of a Super Pump connected to a chamber system representing a model heart. The model heart comprises an (**1**) atrium chamber housing a standard spring valve, an (**2**) aortic chamber with a root section and a (**3**) ventricular chamber with a silicone membrane (see Figure 78). Two chambers allow for adjustability of systematic compliance, while resistance can be set using the peripheral resistance controller. Valves to be tested were housed within the aortic root section, mounted within silicone rings. The stroke of the Super Pump is set to the required cardiac outputs, which is measured by a square-wave electromagnetic flowmeter (Carolina Medical Electronics Inc, NC), while the resistance is adjusted to the desired pressures as measured by three pressure transducers (Utah Medical Products, Inc, UT). The test fluid is 0.9 M sodium chloride solution at 37 °C.

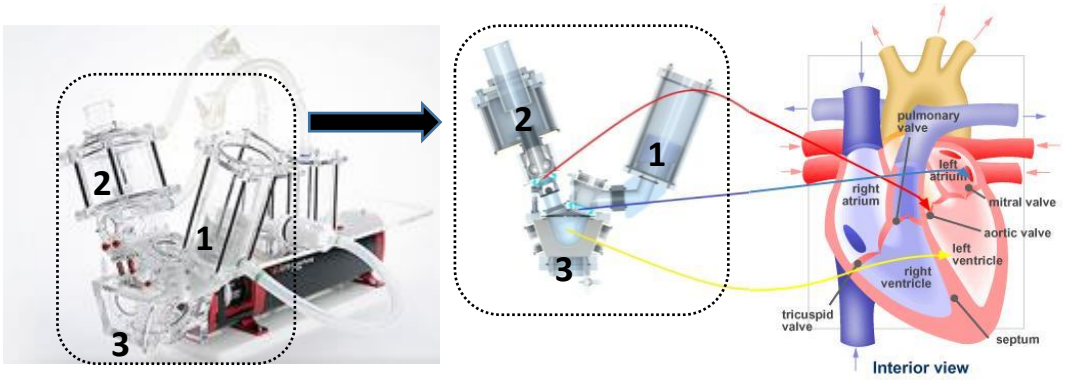

Figure 78: ViVitro Super Pump and model heart with schematic representation of correlation to the left side of the heart

The valves tested in the study comprised a single layered skirt (FLAT) and three double layered skirts (H-FFF, H-NF and H-BFF). All 8 valves (2 per different skirt type) were tested at cardiac outputs (C/O) of 3.5, 5 and 7 liters per minute (lpm) with mean aortic pressure (MAP) adjusted to 100 mmHg. The S35 waveform was selected since it complies with regulatory FDA tests and it corresponds to a 35 % systolic time. The valves were mounted within 4 different silicone rings, which represent different PVR scenarios. Ten cycles were gathered in triplicate per test point at 70 beats per minute.

5.1.3.2. Mock-silicone roots

Rings were cast from Mold Max® 20 (Smooth-On, Macungie, PA), a 2-part tin cure silicone with a shore hardness of 20A using the supplied moulding jig and custom 3D printed pedestal inserts (see Figure 79) to create semi-circular voids along the inner circumference of the ring.

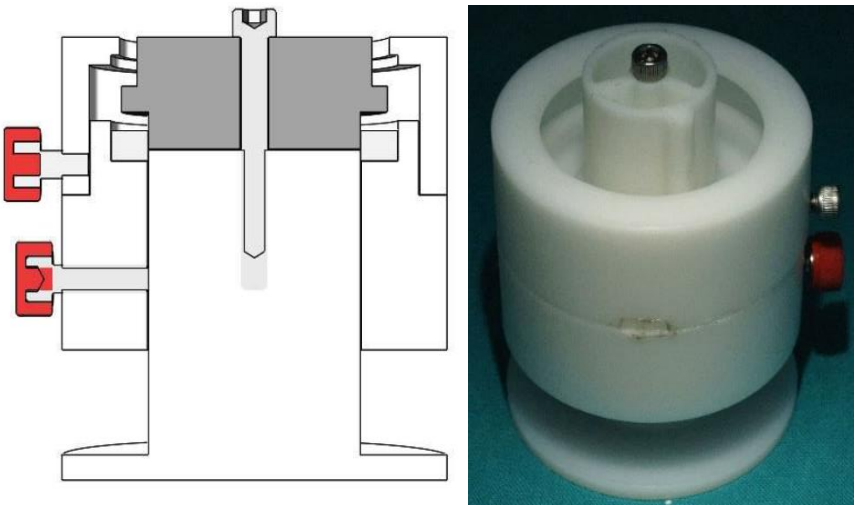

*Figure 79: Engineer drawing of moulding jig (**left**), photograph of moulding jig with custom pedestal in (**right**)*

The inner diameter of the rings was chosen as 21 mm to match levels of oversizing which would be encountered *in-vivo* when using a 23 mm diameter prosthesis (Mylotte, Martucci, & Piazza, 2012). Ultimately, 4 rings were cast having 0,1,2 and 3 voids denoted as R0, R1, R2 and R3 respectively (see Figure 80). This was done to simulate different size paravalvular voids which can be encountered within calcified roots.

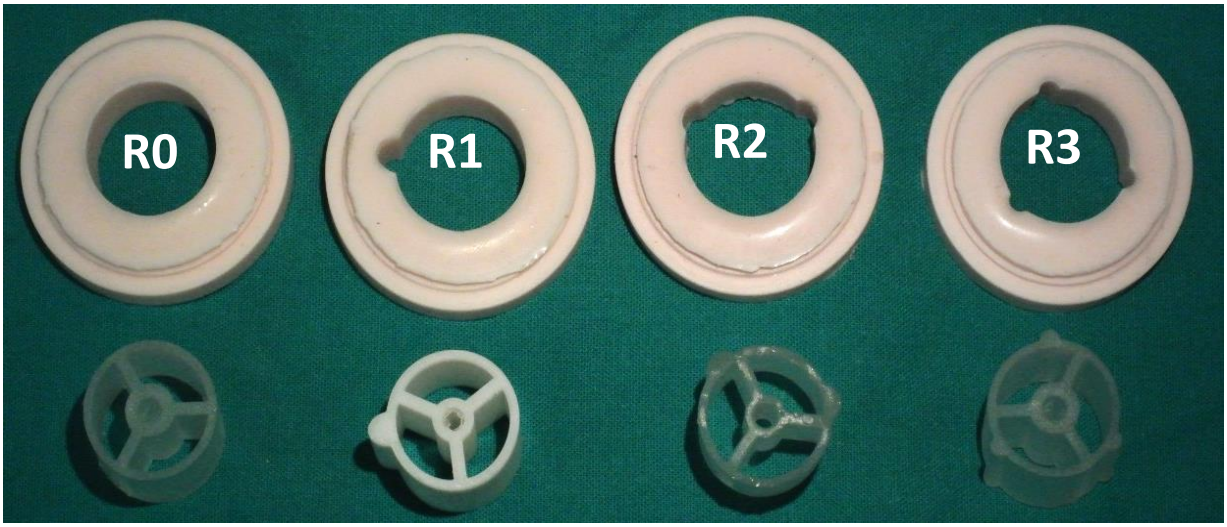

Figure 80: Photograph of resulting rings and corresponding pedestals used for casting

The total void size for each ring was ~12 mm^2, which can be correlated to a similar test found in the literature (Burriesci et al., 2016).

5.1.3.3. Void geometry and valve positioning

For testing in the PD system, silicone rings are suggested to mount valves since they offer a good fluid seal. Typically, rings are cast without voids at different diameters to assess valve hydrodynamic function. The following table shows the relative shape, size and number of semi-elliptical voids cast into the inner circumference (by means of the 3D printed pedestal inserts) of the silicone rings used in the PD system to mount the valves.

Table 15: Relative shapes, size and number of holes in different rings used in sealing study

Ring	Void geometry	Axis		Total Leak area (mm^2)
		Semi-major (mm)	Semi-minor (mm)	
	N/A	N/A	N/A	0
	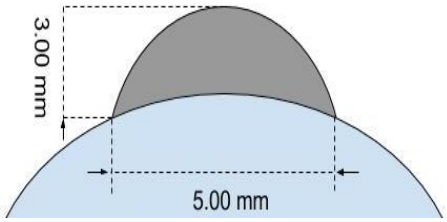	5	3	11.78
	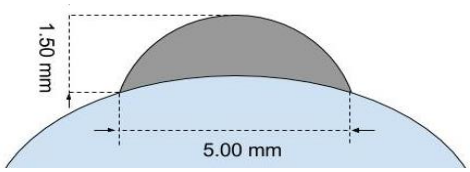	5	1.5	11.78
	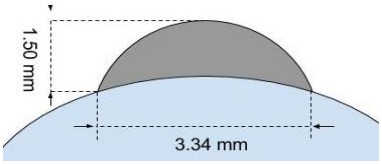	3.34	1.5	11.805

Valves were positioned within the silicone rings so that the lowest arm members of the stents were resting on the ring (see Figure 81).

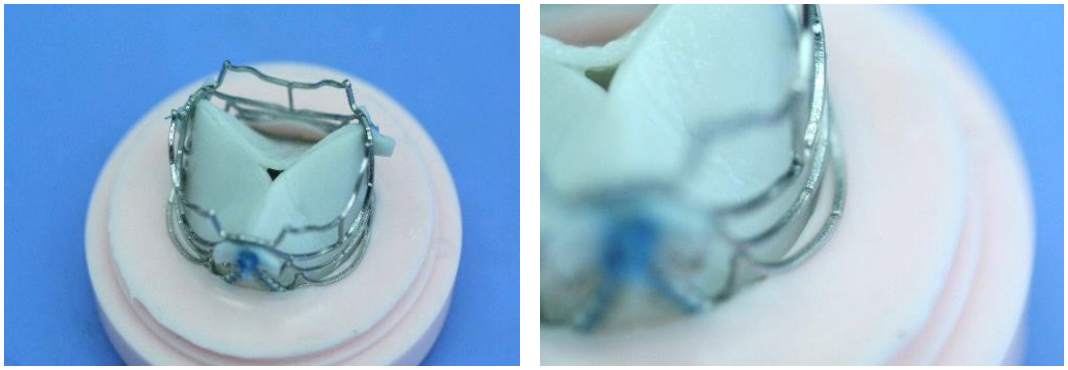

Figure 81: Photographs showing placement of valves within silicone ring (R0), especially, being anchored on the lower arm of the stent.

5.1.3.4. Data obtained from pulse duplicator experiments

A flow cycle of a valve can be divided into aortic forward volume (AFV), closing volume (CV) and leakage volume (LV) (see Figure 82). The sum of CV and LV is defined as the regurgitation volume. The PD system software calculates these values from the measurements based on the flow meter and pressure transducers together with the extrapolation as depicted in Figure 82 below.

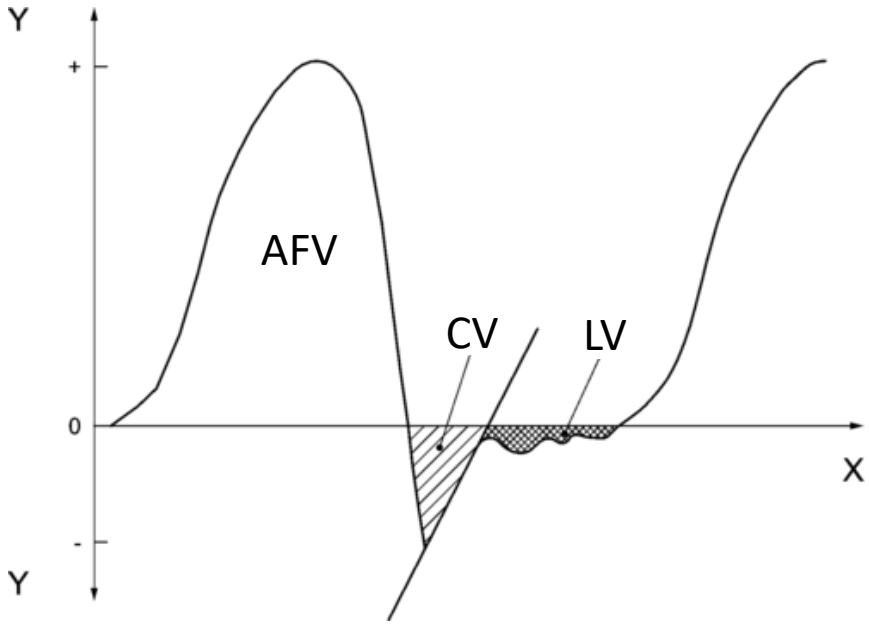

Figure 82: Graphical representation of flow during one heart cycle, indicating AFV closing volume (CV, area 1) and leakage volumes (LV, area 2)

The aortic regurgitation fraction (ARF) can then be defined as follows:

$$ARF\ (\%) = \frac{|CV + LV|}{AFV} \times 100 \qquad (1)$$

and the leakage (LF) and closing (CF) fractions are calculated as:

$$LF\ (\%) = \frac{|LV|}{AFV} \times 100 \qquad (2)$$

$$and$$

$$CF\ (\%) = \frac{|CV|}{AFV} \times 100 \qquad (3)$$

The LV and CV were captured as negative values and hence the absolute value was taken for the equation. Per ISO 5840-3 the LV of a valve is the component of the regurgitation volume associated with leakage that occurs when the valve is closed for a single cycle which corresponds to the sum of the transvalvular and paravalvular leakage.

Total energy loss across a unit time (cardiac cycle) can be calculated as energy loss during forward flow (systole) and energy loss during closing and leakage (diastole). It can be defined as:

$$Energy\ consumption\backslash unit\ time = Q_f(\Delta P_f + \Delta P_{reg} \times RF) \qquad (4)$$

where Q_f is forward flow, ΔP_f is the pressure drop across the valve during forward flow, ΔP_{reg} is the pressure drop through the closed valve and RF is the regurgitant fraction (Hoskins, Lawford, & Doyle, 2017). This quantity is automatically calculated by the PD.

5.1.4. Statistical Analysis

Statistical calculations were performed with JMP 13 (JMP®, Version 13. SAS Institute Inc., Cary, NC, 1989-2007). All data are expressed as mean values with corresponding standard deviations (or standard errors of mean where applicable). Normality of data distribution was tested using the normality test function. For multiple comparisons between data sets a two-way ANOVA was done and for further single comparisons, student t-tests were used. Values were deemed statistically significant if the p-value was 0.05 or less.

5.2. Results and discussion

5.2.1. Aortic regurgitation fraction

Even though the aortic regurgitation fraction (ARF) includes the closing volume of a valve, it is still deemed a useful indicator for assessing procedural success. Mean total ARF across all rings (R0-R3) and cardiac outputs (3.5 lpm, 5 lpm and 7 lpm) were 13.84 ± 1.38, 8.51 ± 0.85. 8.26 ± 1.14 and 6.85 ± 0.67 % for FLAT, H-FFF, H-NF and H-BFF skirts respectively. Minimum device performance requirements for a deployed 23mm valve in the aortic position include a total regurgitation fraction less or equal to 20%.

ARF (solid blue) was seen to be proportional to LF (dashed red), as expected (see Eq. 1) with a relatively constant CF (dashed green) (see Figure 83). Statistical differences in LF between the FLAT skirt and the H-FFF ($p<0.0001$), H-NF ($p<0.0001$) and the H-BFF ($p<0.0001$) skirts were observed. This indicates superior sealing efficacy of dual layered skirts compared to a single layered FLAT skirt. Interestingly, a significant difference was observed between the LF's of the skirts H-FFF and H-BFF, both of which have filling mechanisms ($p=0.007$), with ARF of 6.85% for H-BFF and 8.51% for H-FFF.

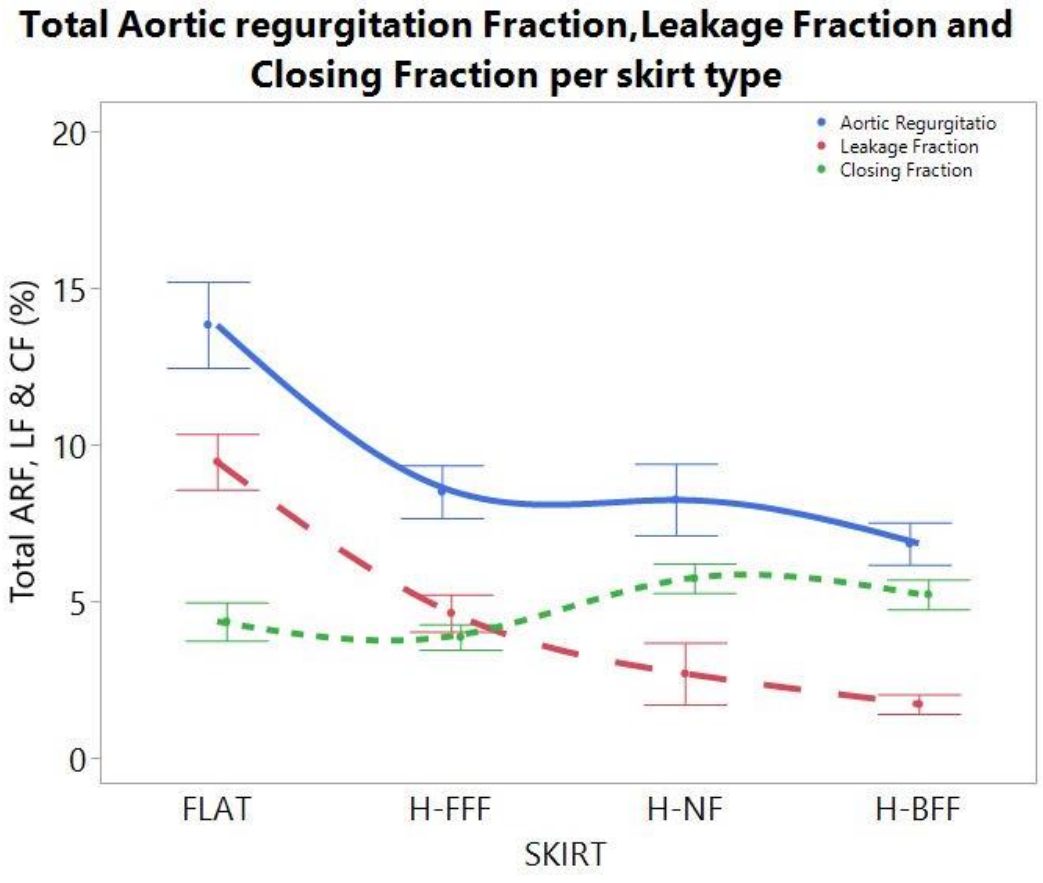

Figure 83: Total Aortic Regurgitation Fraction and respective components per skirt type. Colored lines are for display purposes only.

Reduction in LF's relative to the FLAT skirt can be ascribed to either filling mechanisms present in the H-FFF and H-BFF skirts, extra material in the dual-layered skirts or a combination of the two. To delineate why decreases in LF's relative to the FLAT skirt was observed in H-FFF and H-BFF, a H-NF skirt with excess material but no filling mechanism was tested. The H-NF skirt with excess materials does result in a lower LF when compared to the H-FFF skirt (see Figure 83). This result shows that extra material could influence the sealing efficacy. This difference however is not statistically significant (p=0.07). It must be noted that these results are across all rings and C/O's and subsequent analysis of the results will show the differences of the skirts within varying ring configurations and at different cardiac outputs. See Appendix for further deconvolution of LF results.

5.2.2. Closing and leakage fractions

ARF in R0 is defined as the baseline function for the valves i.e. a 23 mm valve functioning within a 21 mm ring without any paravalvular voids. Dividing ARF_{R0} into its respective components indicated that the FLAT skirt has the highest LF_{R0} (6.33 ± 1.11%). LF_{R0} of the FLAT skirt differs significantly from that of the H-NF (5.91 ± 1.73%, p=0.0009) and H-BFF (6.01 ± 1.73%, p=0.0008). This can possibly be explained by the following; First, placement of the valves within the silicone rings mainly exposes the area between the scallops (big diamond) to diastolic pressures. This area has either one or two layers (depending on skirt type) with the result that the area exposed to the diastolic backflow are of differing thicknesses. An increase in accumulated thickness can lead to higher bending stiffness of the scaffold over the big diamond, which would lead to lower leakage volume through the area. Observing a valve during testing in the PD from a side profile, visualized the section of the skirt that experiences the strongest diastolic backflow to bellow motion (see Figure 84), which supports the hypothesis.

*Figure 84: Photograph of bellowing action of scaffold over 'big diamond' during testing in sealing study. During diastole (**left**) the scaffold region exposed to the back pressure is seen to bend inwards, potentially allowing increased LFs. During systole (**right**) the scaffold is seen to be flush with the silicone ring.*

Secondly, the PD can distinguish between the leakage and closing volumes but does not discern the leakage volume further into its respective transvalvular and paravalvular components. Differences between LF_{R0} could also be due to possible malcoaption of the leaflets (see Figure 85) while tissue selection and leaflet placement prior to suturing may result in possible variations within coaptation behavior and lead to variations within the observed leakage volumes.

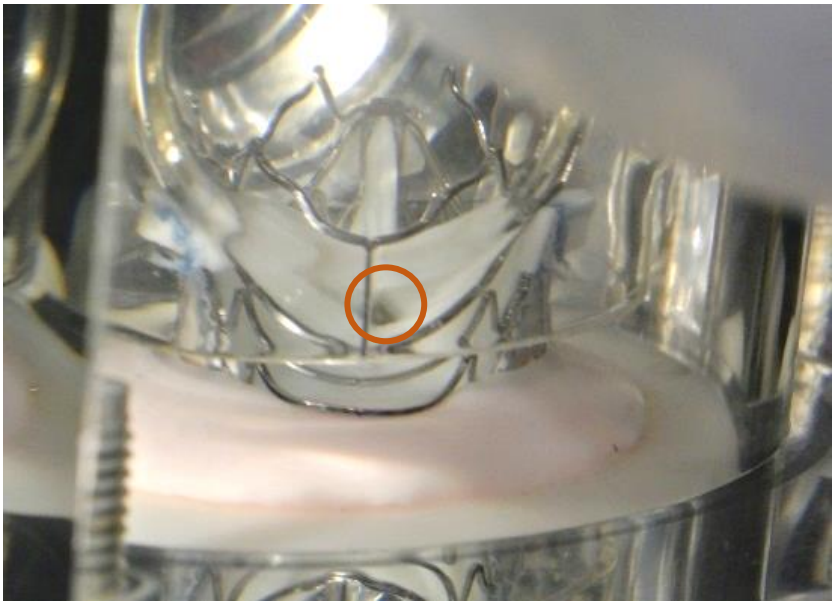

Figure 85: Photograph of malcopation of leaflets, exaggerated example. Silicone ring can be seen as pink surface. Valve was not included in the study

As with the ARF results (see previous section), the FLAT skirt showed the highest LF in all rings. CFs across all valves are relatively constant showing no significant differences. The relationship between LF and CF, where LF is below CF for all skirt types bar FLAT can be seen (see Figure 86) in R0, R2 and R3. In contrast, in R1, the LF of only the H-BFF skirt is lower than that of the CF indicating that the H-BFF skirt seals effectively in single (R1) and multiple (R2 & R3) voided PVR scenarios.

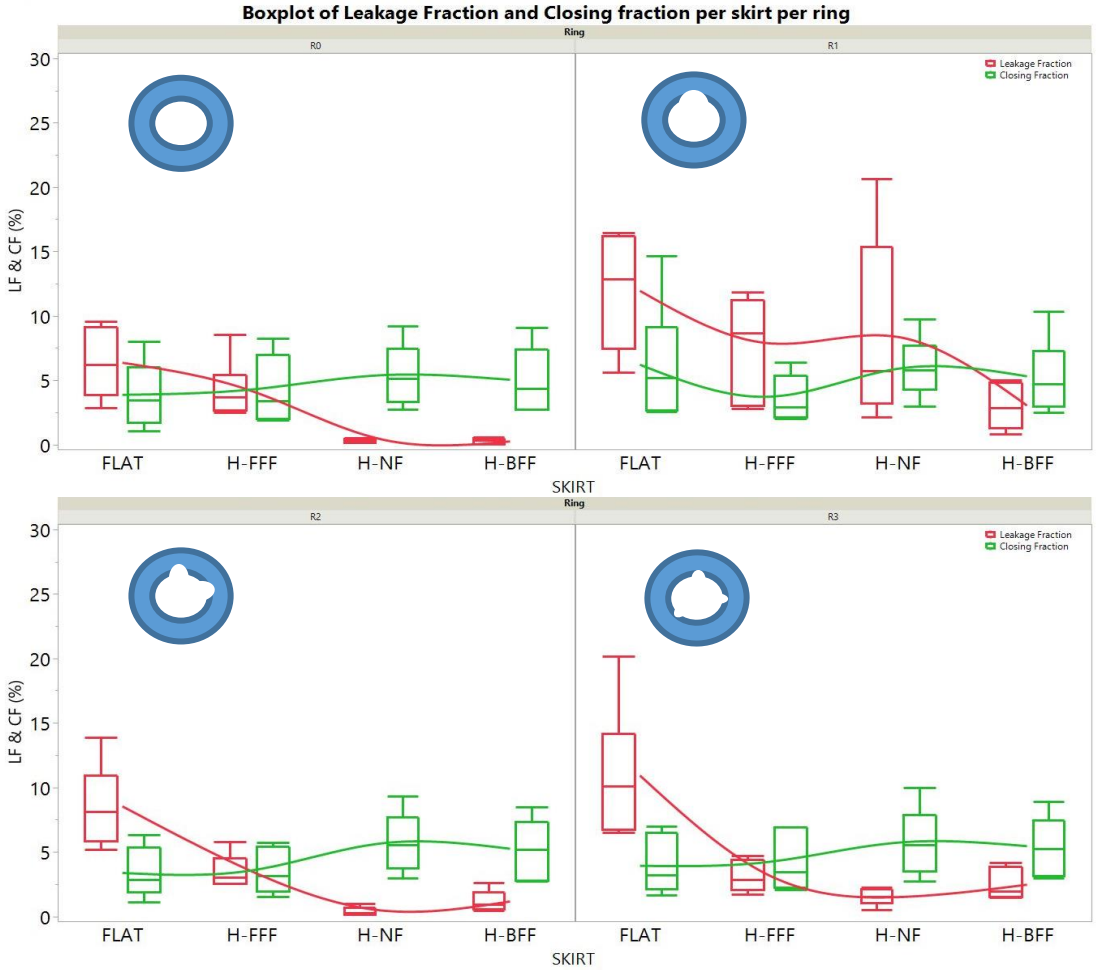

Figure 86: Leakage and closing fractions per skirt in different rings. Lines are for display purposes only.

The worst-case scenario for PVR and in which one needs the best seal, is the scenario depicted with R1 (centralized large void volume). A situation such as this would lead to the most adverse effects in long term mortality and co-morbidities of the patient. In our experiments, valves within R1 did indeed give the highest overall LF.

In R1, the H-BFF skirt resulted in the lowest LF (2.96 ± 0.72%) showing significant differences to the FLAT (12.00 ± 1.84%, $p<0.0001$), H-FFF (7.68 ± 1.58%, $p=0.0081$) and H-NF (8.56 ± 2.94%, $p=0.0018$), respectively. The data for R1 also showed the largest significant differences between the H-BFF skirt (filling) and non-filling skirts (FLAT & H-NF).

Valves tested in R2 and R3 showed the same trend of LF being lower than CF for the H-BFF and H-NF when looking at ARF across all rings and C/O's (see Figure 86). Once again significant differences in LF between the FLAT skirt and all the dual layered skirts were observed.

5.2.3. Leakage fraction as function of cardiac output

As C/O increases the LF decreases in all valves within all ring configurations (see Figure 87). This trend corresponds to the definition by which these parameters are determined (see section 5.1.3.4, Eq. 1). With increasing C/O, the aortic forward volume (AFV) increases but the leakage volume stays relatively constant, leading to a decrease in LF as C/O increases.

The dual layered skirts yielded lower mean LF's than the single layer FLAT skirt in all situations. The H-NF skirt sealed well in R2 and R3 illustrating that a second layer of extra material significantly improves the sealing capabilities of the skirt when sealing against void areas smaller than 6 mm^2. However, the H-NF skirt sealed less effectively in R1 with larger deviation across the mean. These results indicate that in the absence of an active filling mechanism but with a second scaffold layer, sealing improves for smaller PVR voids. Similarly, the H-FFF skirt, that contains a forward flow filling mechanism and has the same amount of material as the H-NF, yields low LF's in R2, but higher LF's in R1. This indicates that the forward flow filling mechanism is less effective than the back-flow filling mechanism and that improved sealing in R2 and R3 (small PVR voids) could be due to the extra material in the second layer. The mechanism by which the H-FFF skirt undergoes filling does not rely on a pressure differential like the H-BFF skirt and may explain the higher LF compared to the H-BFF. In contrast, the possibility exists that the extra material aiding in the sealing of the H-NF and H-FFF skirts move during diastole, effectively reducing the sealing efficacy.

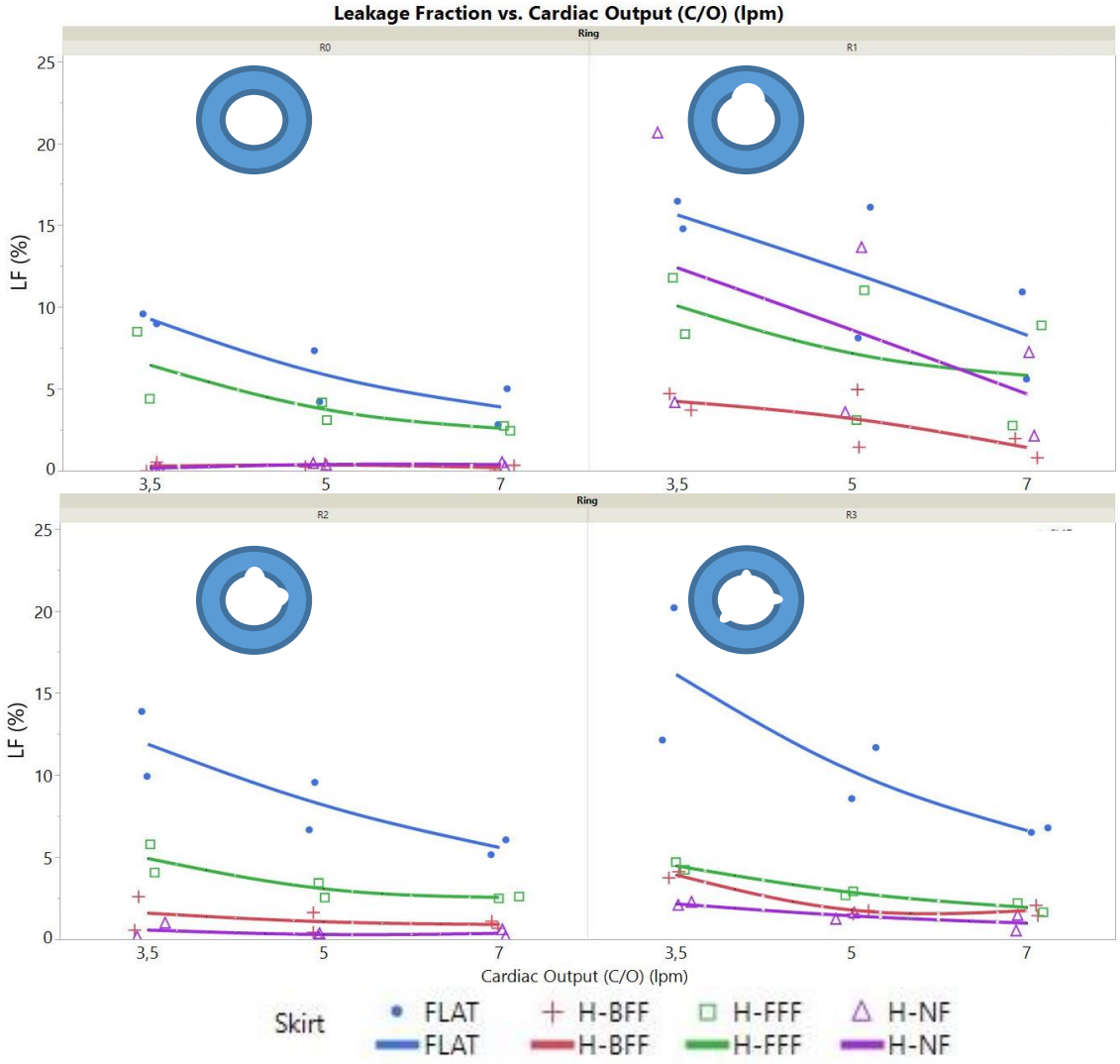

Figure 87: Leakage fraction vs. Cardiac Output for different rings. Colors of lines represent different skirt embodiments

From the results discussed thus far, sealing efficacy (across all conditions) can be correlated to the extra material incorporated as a second layer in conjunction with a successful filling mechanism. Both these features have aspects to consider. Firstly, the amount of excess material in the second layer is determined by the size of the hump. Scaffold thickness in the hump region has an effect since it will influence congruence of the extra material to the geometry of the void. For instance, thicker hump regions would imply increased stiffness, which will refrain the extra material from conforming to the geometry of the leak. On the other hand, the big diamond shaped window on the stent (see previous section) would benefit from a thicker scaffold since the sealing membrane would not undergo large deformations due to bellowing (and lead to decreased LFs).

Secondly, the diastolic filling mechanism of the H-BFF skirt (best sealing design) relies on the inlets being unhindered. For example, the outer skirt of the Edwards Sapien 3 valve is

intended to be placed sub annularly, with 12 inlets spaced around the circumference of the valve. Compared to the H-BFF skirt which has 3 inlets, rotational positioning of the valve is of increased importance. Undesired axial or rotational positioning of the valve, the level of calcification in the native anatomy as well as procedural success all play an important part in whether the bladder fill correctly and aids in sealing.

5.2.4. Energy Loss

To measure the hemodynamic performance across a complete cardiac cycle for natural and prosthesis performance, a useful indicator is energy loss. It combines the effect of pressure differences and leakage giving a more complete picture of valve hydrodynamic performance. Total energy loss was the highest in R1 for all skirt designs. Energy loss due to leakage (red) for all concepts is the lowest in the H-BFF skirt while being the highest in the FLAT skirt (see Figure 88). Even though the energy loss due to leakage for the H-NF skirt in R2 and R3 is slightly lower, no significant differences are observed when compared to the H-BFF skirt. The higher leakage energy loss of the FLAT skirt, within all rings, potentially indicates an increased LF due to only having one layer across the big diamond. Closing energy loss of the H-FFF and FLAT skirts was seen to be the lowest across all rings except for the FLAT skirt in R1. This lower energy loss could be explained by variations in leaflet thickness and valve construction as thinner leaflets would require less energy to close the valve.

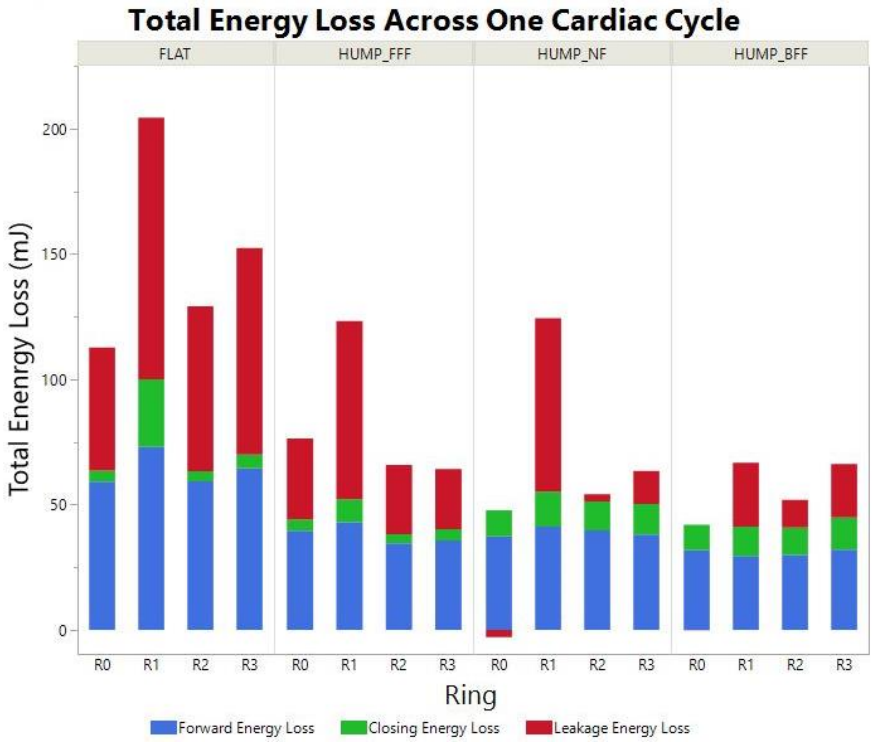

Figure 88: Stacked bar graph of energy loss in different rings (grouped by skirt type).

5.3. Conclusion

In this chapter, bio-prosthetic valves with 4 different skirt designs were tested in an in-vitro pulsatile model with different PVR scenarios. Dual layered skirts were found to seal more effectively against PVR as compared to a single layered skirt. Regurgitation fractions and energy loss were found to be greatest in a simulated environment with a centralized void volume compared to having smaller decentralized void volumes. ARF for all valves were below the ISO requirement of 20%. The H-BFF skirt sealed the most effectively in all situations.

6. Conclusion

By comparison of available materials used as sealing skirts on other TAVR valves in conjunction with the consideration for manufacturability and attachment method, the thermoplastic polyurethane, CarboSil 80A, was identified as a workable sealing skirt material.

Identifying process and solution parameters that have an influence on the resulting scaffold led to the iterative optimization of the electrospinning process. From these, polymer molecular weight, solution feed flow rate, mandrel rotation speed and environmental conditions were identified as important in electrospinning successful scaffolds. The influence of molecular weight on the solution properties was investigated and it was found that solution viscosity is better to optimize to than solution concentration. Mechanical and morphological characterization showed the sensitivity of the above-mentioned parameters on the resulting scaffold. Ultimately, suitable spinning parameters were identified as follow: +13kV applied voltage (-1 kV), 260mm tip to collector distance, 1500 rpm rotation speed, 2 ml/hour feed flow rate, 35 – 45% relative humidity and 16 wt% solution concentration (batch 3(449 kDa), heat pressed, 2580 cP solution viscosity)

Suturing of treated pericardium and PET fabrics to stents have been the principal method of attaching sealing skirts to stents. Having a thermoplastic material allowed for heat bonding and subsequent process automation to be explored. After successful pre-coating of the stent, conductive heat bonding was identified as the superior method of attachment in terms of reproducibility, cost and accessibility. Semi-automated bonding rigs to reduce labor input and improve consistency were initiated with promising initial results, but further development and optimization is still needed.

FEA analysis determined strain values of relevant points before and after crimping, leading to improvement of the bonding pattern for the final sealing skirt design. It also showed displacement of, and forces acting on scaffolds over two single stent elements to not be a concern at a pressure of 140mmHg. Experimental debonding tests allowed for comparison to FEA results and further elucidation of the ideal pre-coating thickness. Long term fatigue results showed a heat bonded skirt to withstand more than 500 million cycles.

After successful manufacture of valves with four different sealing skirts (FLAT, H-FFF, H-NF, H-BFF), an in-vitro pulsatile test setup allowed for testing of the sealing skirts in different PVR scenarios.

Sealing efficiency with regards to PVR improved with the use of a dual layered electrospun sealing skirt as tested in an *in-vitro* pulsatile model. Even though total aortic regurgitation fraction was below the ISO required 20% for all skirt types, the dual layered skirts showed superior sealing efficacy when compared to the FLAT control. From the dual layered skirts, the H-BFF showed the best sealing efficacy with the lowest leakage fraction, even in the most demanding simulated environment, R1 (single void).

The process presented in this study allows for the successful manufacture and attachment of electrospun scaffolds to pre-coated balloon expandable stents for use as a sealing skirts on TAVR valves.

7. Study limitations and future work

Although the study yielded valuable insights into understanding electrospinning, heat bonding and different sealing skirt types and the effects they have on PVR, some limitations could not be avoided.

Further improvement of environmental control, especially temperature, would be beneficial for future work and improve the repeatability of the electrospinning process. Both residual solvent determination and tensile testing would benefit from greater sample numbers. The small sample size (n=1) of the residual solvent determination was due to the prohibitive cost of analysis. The lack of adequate sample numbers in the tensile tests for batch 1 were due to samples being prepared from the last remaining polymer pellets of batch 1. Further, it has been suggested to explore the biaxial tensile nature of electrospun scaffolds for a more in depth mechanical analysis of electrospun scaffolds. The lack of such facilities made biaxial analyses impossible. Therefore, biaxial tensile testing is highly recommended for future work since it would deepen the understanding of the mechanical properties of electrospun scaffolds and allow for comparison to biological tissue.

Design improvements, together with thorough testing of the resulting attachment, would lead to improved automated bonding rigs and hence remove the variability imparted to manual bonding. Especially, investigating other possible methods of applying pressure during the bonding process requires more investigation together with an improved laser system (that has at least 3 axis of freedom), would make this method viable for bonding electrospun skirts to pre-coated stents.

Evaluating the significant differences across the experiments, more valves per group would have minimized statistical variability. The number of valves per group was mainly governed by the resource intensive nature in the manufacturing and production of the valves. Having many valves to test may have quashed the inherent variable nature of hand-made valves, especially negating the effect of variable leaflet thickness.

As TAVR valves are crimped and deployed, this study would be more aligned with *in-vivo* situations if the valves were crimped and deployed into the silicone rings and is recommended for further studies.

Further long term *in-vivo* studies are currently being conducted and results in terms of paravalvular sealing and long-term durability of electrospun scaffolds as a sealing skirt would greatly support the current work discussed in this thesis.

8. Appendix

8.1. Pore size macro script

The following code was used as a macro in FIJI to determine the pore sizes from SEM images at 500× magnification:

```
macro "PoreSizes_new [f1]"

//print ("Pore size calculator for fibres taken at x500 (4.5pix/um) using the LEO SEM.\n\nThis Macro was compiled (2015) and finalized (2016) by Wian van den Bergh")

run("Enhance Contrast...", "saturated=0.3 normalize equalize");
run("Statistical Region Merging", "q=25 showaverages");
run("Set Scale...", "distance=90 known=20 unit=um");
makeRectangle(0, 0, 1024, 678);
run("Crop");
setAutoThreshold("Default dark");
setAutoThreshold("Default dark");
setOption("BlackBackground", false);
run("Convert to Mask");
run("Median...", "radius=3.5");
run("Find Edges");
run("Fill Holes");
run("Analyze Particles...", "size=0-infinity show=[Overlay Masks] display exclude summarize in_situ"); }
```

8.2. Coherency determination

The following settings were used when using the quantitative orientation measurement mode in the OrientationJ plugin for determination of coherency for a region of interest (entire image) which was taken as a measure of isotropy. 0 = 100% isotropic and 1 = 100% anisotropic

Laplacian of Gaussian (sigma) as pre-filter: 0.0

Ellipse thickness: 0.5

Ellipse opacity: 100

Color: 255

Area Opacity: 50

8.3. Aortic regurgitation fraction, leakage fraction and closing fraction (expanded)

The following graph and table are added for further explanation of leakage fraction (LF) and closing fraction (CF) results of valves used in the sealing study. It shows the magnitude of the differences between LF's at the various cardiac outputs.

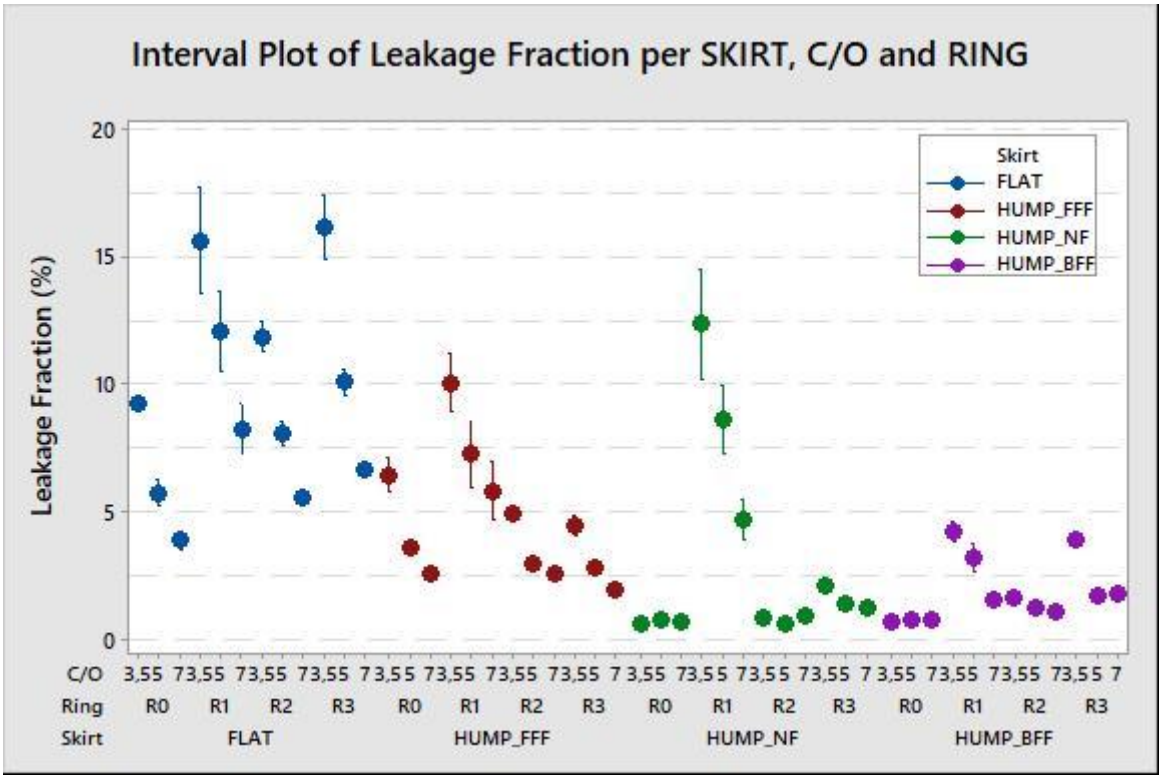

Figure 89: Interval plot of LF per skirt type (FLAT, HUMP-BFF, HUMP-NF and HUMP-FFF), cardiac output (3.5, 5, and 7 lpm) and silicone ring (R0, R1, R2 amd R3)

Table 16: Leakage and closing fractions (per ring, skirt type and cardiac output) of valves tested in the sealing study

			Leakage Fraction		Closing Fraction	
Ring	Skirt	Cardiac Output...	Mean	Std Err	Mean	Std Err
R0	FLAT	3,5	9,28	0,30	6,71	1,32
		5	5,78	1,56	3,42	0,64
		7	3,92	1,09	1,49	0,44
	HUMP_BFF	3,5	0,28	0,27	7,95	1,13
		5	0,37	0,10	4,35	0,06
		7	0,19	0,17	2,75	0,01
	HUMP_FFF	3,5	6,47	2,05	7,38	0,84
		5	3,66	0,53	3,37	0,02
		7	2,62	0,15	1,97	0,10
	HUMP_NF	3,5	0,16	0,00	8,02	1,17
		5	0,40	0,05	5,13	0,87
		7	0,38	0,13	3,13	0,42
R1	FLAT	3,5	15,62	0,84	10,97	3,68
		5	12,10	3,99	5,17	0,28
		7	8,26	2,66	2,63	0,05
	HUMP_BFF	3,5	4,23	0,51	8,28	2,03
		5	3,23	1,76	4,68	0,78
		7	1,41	0,59	2,82	0,31
	HUMP_FFF	3,5	10,09	1,72	5,70	0,67
		5	7,09	3,96	2,92	0,14
		7	5,85	3,06	2,09	0,10
	HUMP_NF	3,5	12,40	8,23	8,27	1,47
		5	8,60	5,03	5,93	1,12
		7	4,68	2,55	3,87	0,89
R2	FLAT	3,5	11,90	1,97	5,71	0,64
		5	8,12	1,44	2,86	0,33
		7	5,61	0,45	1,62	0,48
	HUMP_BFF	3,5	1,61	1,02	7,72	0,76
		5	1,06	0,60	5,16	0,53
		7	0,92	0,21	2,77	0,04
	HUMP_FFF	3,5	4,95	0,86	5,53	0,22
		5	3,01	0,45	3,13	0,09
		7	2,58	0,05	1,80	0,30
	HUMP_NF	3,5	0,58	0,42	8,22	1,07
		5	0,28	0,07	5,54	0,79
		7	0,38	0,21	3,47	0,53
R3	FLAT	3,5	16,16	4,03	6,66	0,34
		5	10,13	1,55	3,19	0,24
		7	6,65	0,14	1,98	0,33
	HUMP_BFF	3,5	3,96	0,19	7,92	0,97
		5	1,67	0,10	5,27	0,36
		7	1,79	0,31	3,09	0,15
	HUMP_FFF	3,5	4,49	0,23	6,92	0,02
		5	2,82	0,12	3,43	0,45
		7	1,96	0,28	2,18	0,14
	HUMP_NF	3,5	2,17	0,09	8,57	1,43
		5	1,42	0,19	5,55	1,00
		7	0,99	0,47	3,22	0,52

8.4. Finite Element Analysis

8.4.1. Mesh topology and boundary conditions

The stent was discretized with hexahedral elements. The latter were C3D8R elements, 8-node linear bricks with reduced integration (ABAQUS 2016 User Manual). The stent was meshed with an approximate global size of 0.1 and with 4 elements across the thickness. A mesh convergence study was performed but is not presented in the thesis. The skirt was

meshed with S4 shell elements with an approximate global size of 0.075. The mesh was fine enough that no convergence was deemed necessary.

It is assumed that the skirt is fixed to the stent, as such a zero displacement was prescribed at the edges to prevent displacement in the x, y and z direction. The pressure of 140 mmHg was applied by using a smooth function which provides numerical stability at the start of the simulation.

8.4.2. Contact model and material properties

The general contact model is a contact model available in ABAQUS. The model is available for both Abaqus/Standard and Abaqus/Explicit. For the latter, the model can create interactions for three-dimensional surfaces as well as analytical rigid surfaces (Abaqus Analysis User's Manual, Volume 5). The implementation was performed by using the interaction module in Abaqus and by creating contact properties to define the tangential and normal behaviours. A frictionless formulation was used for the tangential behaviour and a "Hard" contact was used for the pressure-overclosure in view of defining the normal behaviour of the contact.

The material model used (shown in Figure below) was based on the stress-strain curve performed on three samples. The data from sample 3 was used. A Young's Modulus 239.5 GPa and a Poisson's ratio of 0.3775 were used.

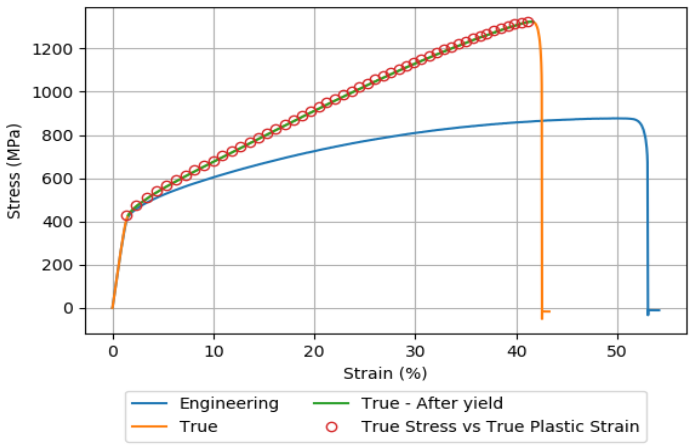

Figure 90: Material model as was used for FEM of stent

9. References

Agarwal, S., Kapadia, S., Tuzcu, E. M., & Krishnaswamy, A. (2016). Safety and efficacy of transcatheter aortic valve replacement in intermediate risk patients sets the stage for contemporary trials in lower risk groups. *Cardiovasc Diagn Ther, 6*(5), 459-461. doi:10.21037/cdt.2016.05.01

Agatston, A. S., Janowitz, W. R., Hildner, F. J., Zusmer, N. R., Viamonte, M., Jr., & Detrano, R. (1990). Quantification of coronary artery calcium using ultrafast computed tomography. *J Am Coll Cardiol, 15*(4), 827-832.

Ali, O., Salinger, M. H., Levisay, J. P., & Feldman, T. (2014). High pacing rates for management of aortic insufficiency after balloon aortic valvuloplasty or transcatheter aortic valve replacement. *Catheterization and Cardiovascular Interventions, 83*(1), 162-168. doi:10.1002/ccd.24902

Balguid, A., Mol, A., van Marion, M. H., Bank, R. A., Bouten, C. V., & Baaijens, F. P. (2009). Tailoring fiber diameter in electrospun poly(epsilon-caprolactone) scaffolds for optimal cellular infiltration in cardiovascular tissue engineering. *Tissue Eng Part A, 15*(2), 437-444. doi:10.1089/ten.tea.2007.0294

Bates, E. R. (2011). Treatment options in severe aortic stenosis. *Circulation, 124*(3), 355-359. doi:10.1161/circulationaha.110.974204

Beachley, V., & Wen, X. (2009). Effect of electrospinning parameters on the nanofiber diameter and length. *Materials Science and Engineering: C, 29*(3), 663-668. doi:https://doi.org/10.1016/j.msec.2008.10.037

Bergmeister, H., Schreiber, C., Grasl, C., Walter, I., Plasenzotti, R., Stoiber, M., Schima, H. (2013). Healing characteristics of electrospun polyurethane grafts with various porosities. *Acta Biomater, 9*(4), 6032-6040. doi:10.1016/j.actbio.2012.12.009

Bhowmick, A. K., & Stephens, H. (2000). *Handbook of Elastomers, Second Edition*: Taylor & Francis.

Binder, R. K., Rodés-Cabau, J., Wood, D. A., Mok, M., Leipsic, J., De Larochellière, R., Webb, J. G. (2013). Transcatheter Aortic Valve Replacement With the SAPIEN 3A New Balloon-Expandable Transcatheter Heart Valve. *JACC: Cardiovascular Interventions, 6*(3), 293-300. doi:10.1016/j.jcin.2012.09.019

Boland, E. D., Coleman, B. D., Barnes, C. P., Simpson, D. G., Wnek, G. E., & Bowlin, G. L. (2005). Electrospinning polydioxanone for biomedical applications. *Acta Biomaterialia, 1*(1), 115-123. doi:10.1016/j.actbio.2004.09.003

Bonino, C. A., Efimenko, K., Jeong, S. I., Krebs, M. D., Alsberg, E., & Khan, S. A. (2012). Three-dimensional electrospun alginate nanofiber mats via tailored charge repulsions. *Small, 8*(12), 1928-1936. doi:10.1002/smll.201101791

Bracco, P., Zanetti, M., Cipriani, E., & Costa, L. (2010). Characterization of a Polycarbonate-urethane elastomer for orthopedic applications. . *Poster No. 1191 • 56th Annual Meeting of the Orthopaedic Research Society*.

Braunwald, E. (2000). Aortic valve replacement: an update at the turn of the millennium. *Eur Heart J, 21*(13), 1032-1033. doi:10.1053/euhj.1999.2052

Burman, E. D., Keegan, J., & Kilner, P. J. (2008). Aortic root measurement by cardiovascular magnetic resonance: specification of planes and lines of measurement and corresponding normal values. *Circ Cardiovasc Imaging, 1*(2), 104-113. doi:10.1161/circimaging.108.768911

Burriesci, G., Peruzzo, P., Susin, F. M., Tarantini, G., & Colli, A. (2016). In vitro hemodynamic testing of Amplatzer plugs for paravalvular leak occlusion after transcatheter aortic valve implantation. *Int J Cardiol, 203*, 1093-1099. doi:10.1016/j.ijcard.2015.11.106

Cadafalch Gazquez, G., Smulders, V., Veldhuis, S. A., Wieringa, P., Moroni, L., Boukamp, B. A., & Ten Elshof, J. E. (2017). Influence of Solution Properties and Process Parameters on the Formation and Morphology of YSZ and NiO Ceramic Nanofibers by Electrospinning. *Nanomaterials (Basel), 7*(1). doi:10.3390/nano7010016

Callister, T. Q., Cooil, B., Raya, S. P., Lippolis, N. J., Russo, D. J., & Raggi, P. (1998). Coronary artery disease: improved reproducibility of calcium scoring with an electron-beam CT volumetric method. *Radiology, 208*(3), 807-814. doi:10.1148/radiology.208.3.9722864

Carabello, B. A., & Paulus, W. J. (2009). Aortic stenosis. *Lancet, 373*(9667), 956-966. doi:10.1016/s0140-6736(09)60211-7

Charitos, E. I., & Sievers, H. H. (2013). Anatomy of the aortic root: implications for valve-sparing surgery. *Ann Cardiothorac Surg, 2*(1), 53-56. doi:10.3978/j.issn.2225-319X.2012.11.18

Chowdhury, M., & Stylios, G. (2010). *Effect of experimental parameters on the morphology of electrospun Nylon 6 fibres* (Vol. 10).

Cipriani, E., Bracco, P., Kurtz, S. M., Costa, L., & Zanetti, M. (2013). In-vivo degradation of poly(carbonate-urethane) based spine implants. *Polymer degradation and stability, 98*(6), 1225-1235. doi:10.1016/j.polymdegradstab.2013.03.005

Cipriani, E., Zanetti, M., Brunella, V., Costa, L., & Bracco, P. (2012). Thermoplastic polyurethanes with polycarbonate soft phase: Effect of thermal treatment on phase morphology. *Polymer Degradation and Stability, 97*(9), 1794-1800. doi:http://dx.doi.org/10.1016/j.polymdegradstab.2012.06.004

Colli, A., D'Amico, R., Kempfert, J., Borger, M. A., Mohr, F. W., & Walther, T. (2011). Transesophageal echocardiographic scoring for transcatheter aortic valve implantation: impact of aortic cusp calcification on postoperative aortic regurgitation. *J Thorac Cardiovasc Surg, 142*(5), 1229-1235. doi:10.1016/j.jtcvs.2011.04.026

Corciu, A. I., Siciliano, V., Poggianti, E., Petersen, C., Venneri, L., & Picano, E. (2010). Cardiac calcification by transthoracic echocardiography in patients with known or suspected coronary artery disease. *Int J Cardiol, 142*(3), 288-295. doi:10.1016/j.ijcard.2009.01.021

Cribier, A., Eltchaninoff, H., Bash, A., Borenstein, N., Tron, C., Bauer, F., . . . Leon, M. B. (2002). Percutaneous Transcatheter Implantation of an Aortic Valve Prosthesis for Calcific Aortic Stenosis: First Human Case Description. *Circulation, 106*(24), 3006-3008. doi:10.1161/01.cir.0000047200.36165.b8

Cribier, A. G. (2014). The Odyssey of TAVR from Concept to Clinical Reality. *Texas Heart Institute Journal, 41*(2), 125-130. doi:10.14503/THIJ-14-4137

Daneault, B., Koss, E., Hahn, R. T., Kodali, S., Williams, M. R., Généreux, P., . . . Leon, M. B. (2013). Efficacy and Safety of Postdilatation to Reduce Paravalvular Regurgitation During Balloon-Expandable Transcatheter Aortic Valve Replacement. *Circulation: Cardiovascular Interventions, 6*(1), 85-91. doi:10.1161/circinterventions.112.971614

Del Gaudio, C., Bianco, A., & Grigioni, M. (2008). Electrospun bioresorbable trileaflet heart valve prosthesis for tissue engineering: in vitro functional assessment of a pulmonary cardiac valve design. *Ann Ist Super Sanita, 44*(2), 178-186.

Delgado, V., Ng, A. C. T., van de Veire, N. R., van der Kley, F., Schuijf, J. D., Tops, L. F., . . . Bax, J. J. (2010). Transcatheter aortic valve implantation: role of multi-detector row computed tomography to evaluate prosthesis positioning and deployment in relation to valve function. *European Heart Journal, 31*(9), 1114-1123. doi:10.1093/eurheartj/ehq018

Detaint, D., Lepage, L., Himbert, D., Brochet, E., Messika-Zeitoun, D., Iung, B., & Vahanian, A. (2009). Determinants of significant paravalvular regurgitation after transcatheter aortic valve: implantation impact of device and annulus discongruence. *JACC Cardiovasc Interv, 2*(9), 821-827. doi:10.1016/j.jcin.2009.07.003

Ding, B., Wang, M., Wang, X., Yu, J., & Sun, G. (2010). Electrospun nanomaterials for ultrasensitive sensors. *Materials Today, 13*(11), 16-27. doi:http://dx.doi.org/10.1016/S1369-7021(10)70200-5

Eichhorn, S. J., & Sampson, W. W. (2010). Relationships between specific surface area and pore size in electrospun polymer fibre networks. *J R Soc Interface, 7*(45), 641-649. doi:10.1098/rsif.2009.0374

Ewe, S. H., Ng, A. C., Schuijf, J. D., van der Kley, F., Colli, A., Palmen, M., . . . Delgado, V. (2011). Location and severity of aortic valve calcium and implications for aortic regurgitation after transcatheter aortic valve implantation. *Am J Cardiol, 108*(10), 1470-1477. doi:10.1016/j.amjcard.2011.07.007

Feng, Y., Meng, F., Xiao, R., Zhao, H., & Guo, J. (2011). Electrospinning of polycarbonate urethane biomaterials. *Frontiers of Chemical Science and Engineering, 5*(1), 11-18. doi:10.1007/s11705-010-1011-x

Feuchtner, G., Plank, F., Bartel, T., Mueller, S., Leipsic, J., Schachner, T., . . . Bonaros, N. (2013). Prediction of paravalvular regurgitation after transcatheter aortic valve implantation by computed tomography: value of aortic valve and annular calcification. *Ann Thorac Surg, 96*(5), 1574-1580. doi:10.1016/j.athoracsur.2013.06.049

Fonck, E., Feigl, G. G., Fasel, J., Sage, D., Unser, M., Rufenacht, D. A., & Stergiopulos, N. (2009). Effect of aging on elastin functionality in human cerebral arteries. *Stroke, 40*(7), 2552-2556. doi:10.1161/STROKEAHA.108.528091

Fonseca, P., Figueiredo, B., Almeida, C., Almeida, J., Bettencourt, N., Sampaio, F., . . . Ribeiro, V. G. (2016). Aortic Valve Calcium Volume Predicts Paravalvular Regurgitation and the Need for Balloon Post-Dilatation After Transcatheter Aortic Valve Implantation. *J Interv Cardiol, 29*(1), 117-123. doi:10.1111/joic.12267

Frantz, C., Stewart, K. M., & Weaver, V. M. (2010). The extracellular matrix at a glance. *Journal of Cell Science, 123*(24), 4195-4200. doi:10.1242/jcs.023820

Ghanbari, H., de Mel, A., & Seifalian, A. M. (2011). Cardiovascular application of polyhedral oligomeric silsesquioxane nanomaterials: a glimpse into prospective horizons. *Int J Nanomedicine, 6*, 775-786. doi:10.2147/IJN.S14881

Gibson, P. S., & Powrie, R. (2009). Anticoagulants and pregnancy: when are they safe? *Cleve Clin J Med, 76*(2), 113-127. doi:10.3949/ccjm.75a.072272

Gotzmann, M., Lindstaedt, M., & Mugge, A. (2012). From pressure overload to volume overload: aortic regurgitation after transcatheter aortic valve implantation. *Am Heart J, 163*(6), 903-911. doi:10.1016/j.ahj.2012.03.017

Guidoin, R., King, M., Marceau, D., Cardou, A., De La Faye, D., Legendre, J.-M., & Blais, P. (1987). Textile arterial prostheses: Is water permeability equivalent to porosity? *J Biomed Mater Res, 21*(1), 65-87. doi:10.1002/jbm.820210111

Gunatillake, P. A., Meijs, G. F., McCarthy, S. J., & Adhikari, R. (2000). Poly(dimethylsiloxane)/poly(hexamethylene oxide) mixed macrodiol based polyurethane elastomers. I. Synthesis and properties. *Journal of Applied Polymer Science, 76*(14), 2026-2040. doi:10.1002/(SICI)1097-4628(20000628)76:14<2026::AID-APP5>3.0.CO;2-X

Hahn, R. T., Pibarot, P., Weissman, N. J., Rodriguez, L., & Jaber, W. A. (2015). Assessment of paravalvular aortic regurgitation after transcatheter aortic valve replacement: intra-core laboratory variability. *J Am Soc Echocardiogr, 28*(4), 415-422. doi:10.1016/j.echo.2015.01.007

Hamdan, A., Guetta, V., Konen, E., Goitein, O., Segev, A., Raanani, E., Schwammenthal, E. (2012). Deformation dynamics and mechanical properties of the aortic annulus by 4-dimensional computed tomography: insights into the functional anatomy of the aortic valve complex and implications for transcatheter aortic valve therapy. *J Am Coll Cardiol, 59*(2), 119-127. doi:10.1016/j.jacc.2011.09.045

Höllriegel, R., Woitek, F., Stativa, R., Mangner, N., Haußig, S., Fuernau, G., Linke, A. (2016). Hemodynamic Assessment of Aortic Regurgitation After Transcatheter Aortic Valve ReplacementThe Diastolic Pressure-Time Index. *JACC: Cardiovascular Interventions, 9*(10), 1061-1068. doi:10.1016/j.jcin.2016.02.012

Holzhey, D., Linke, A., Treede, H., Baldus, S., Bleiziffer, S., Wagner, A., Falk, V. (2013). Intermediate follow-up results from the multicenter engager European pivotal trial. *Ann Thorac Surg, 96*(6), 2095-2100. doi:10.1016/j.athoracsur.2013.06.089

Hong, C., Becker, C. R., Schoepf, U. J., Ohnesorge, B., Bruening, R., & Reiser, M. F. (2002). Coronary artery calcium: absolute quantification in nonenhanced and contrast-enhanced multi-detector row CT studies. *Radiology, 223*(2), 474-480. doi:10.1148/radiol.2232010919

Hoskins, P. R., Lawford, P. V., & Doyle, B. J. (2017). *Cardiovascular Biomechanics*: Springer International Publishing.

Huber, C., Wenaweser, P., Windecker, S., & Carrel, T. (2014). Transapical transcatheter aortic valve implantation using the second-generation self-expanding Symetis ACURATE TA valve. *Multimedia Manual of Cardio-Thoracic Surgery, 2014*. doi:10.1093/mmcts/mmu017

Iqbal, J., & Serruys, P. W. (2014). Comparison of Medtronic CoreValve and Edwards Sapien XT for Transcatheter Aortic Valve ImplantationThe Need for an Imaging-Based Personalized Approach in Device Selection∗. *JACC: Cardiovascular Interventions, 7*(3), 293-295. doi:10.1016/j.jcin.2014.01.147

Iung, B., Baron, G., Butchart, E. G., Delahaye, F., Gohlke-Barwolf, C., Levang, O. W., Vahanian, A. (2003). A prospective survey of patients with valvular heart disease in Europe: The Euro Heart Survey on Valvular Heart Disease. *Eur Heart J, 24*(13), 1231-1243. Retrieved from http://eurheartj.oxfordjournals.org/content/ehj/24/13/1231.full.pdf

Jamalzadeh, L., Ghafoori, H., Sariri, R., Rabuti, H., Nasirzade, J., Hasani, H., & Aghamaali, M. R. (2016). Cytotoxic Effects of Some Common Organic Solvents on MCF-7, RAW-264.7 and Human Umbilical Vein Endothelial Cells. *Avicenna J Med Biochem, 4*(1), 10-33453. doi:10.17795/ajmb-33453

John, D., Buellesfeld, L., Yuecel, S., Mueller, R., Latsios, G., Beucher, H., Grube, E. (2010). Correlation of Device landing zone calcification and acute procedural success in patients undergoing transcatheter aortic valve implantations with the self-expanding CoreValve prosthesis. *JACC Cardiovasc Interv, 3*(2), 233-243. doi:10.1016/j.jcin.2009.11.015

Kaneko, T., Cohn, L. H., & Aranki, S. F. (2013). Tissue Valve Is the Preferred Option for Patients Aged 60 and Older. *Circulation, 128*(12), 1365-1371. doi:10.1161/circulationaha.113.002584

Kappetein, A. P., Head, S. J., Genereux, P., Piazza, N., van Mieghem, N. M., Blackstone, E. H., . . . Leon, M. B. (2012). Updated standardized endpoint definitions for transcatheter aortic valve implantation: the Valve Academic Research Consortium-2 consensus document. *Eur Heart J, 33*(19), 2403-2418. doi:10.1093/eurheartj/ehs255

Kempfert, J., Rastan, A. J., Beyersdorf, F., Schönburg, M., Schuler, G., Sorg, S., . . . Walther, T. (2011). Trans-apical aortic valve implantation using a new self-expandable bioprosthesis: initial outcomes. *European Journal of Cardio-Thoracic Surgery, 40*(5), 1114-1119. doi:10.1016/j.ejcts.2011.01.078

Khan, I., Smith, N., Jones, E., Finch, D. S., & Cameron, R. E. (2005). Analysis and evaluation of a biomedical polycarbonate urethane tested in an in vitro study and an ovine arthroplasty model. Part I: materials selection and evaluation. *Biomaterials, 26*(6), 621-631. doi:10.1016/j.biomaterials.2004.02.065

Kim, G., & Kim, W. (2007). Highly porous 3D nanofiber scaffold using an electrospinning technique. *J Biomed Mater Res B Appl Biomater, 81*(1), 104-110. doi:10.1002/jbm.b.30642

Kriegel, C., Arecchi, A., Kit, K., McClements, D. J., & Weiss, J. (2008). Fabrication, functionalization, and application of electrospun biopolymer nanofibers. *Crit Rev Food Sci Nutr, 48*(8), 775-797. doi:10.1080/10408390802241325

Kulik, A., Rubens, F. D., Mesana, T. G., & Lam, B. K. (2006). Early postoperative anticoagulation: more questions than answers? *Ann Thorac Surg, 82*(4), 1573-1574; author reply 1574-1575. doi:10.1016/j.athoracsur.2005.09.058

Kuraishi, K., Iwata, H., Nakano, S., Kubota, S., Tonami, H., Toda, M., Taki, W. (2009). Development of nanofiber-covered stents using electrospinning: in vitro and acute phase in vivo experiments. *J Biomed Mater Res B Appl Biomater, 88*(1), 230-239. doi:10.1002/jbm.b.31173

Kwon, I. K., Kidoaki, S., & Matsuda, T. (2005). Electrospun nano- to microfiber fabrics made of biodegradable copolyesters: structural characteristics, mechanical properties and cell adhesion potential. *Biomaterials, 26*(18), 3929-3939. doi:10.1016/j.biomaterials.2004.10.007

Lavielle, N., Hébraud, A., Schlatter, G., Thöny-Meyer, L., Rossi, R. M., & Popa, A.-M. (2013). Simultaneous Electrospinning and Electrospraying: A Straightforward Approach for Fabricating Hierarchically Structured Composite Membranes. *ACS Applied Materials & Interfaces, 5*(20), 10090-10097. doi:10.1021/am402676m

Lee, C. H., Lin, Y. H., Chang, S. H., Tai, C. D., Liu, S. J., Chu, Y., Huang, Y. (2014). Local sustained delivery of acetylsalicylic acid via hybrid stent with biodegradable nanofibers reduces adhesion of blood cells and promotes reendothelialization of the denuded artery. *Int J Nanomedicine, 9*, 311-326. doi:10.2147/ijn.s51258

Lee, J. B., Jeong, S. I., Bae, M. S., Yang, D. H., Heo, D. N., Kim, C. H., . . . Kwon, I. K. (2011). Highly porous electrospun nanofibers enhanced by ultrasonication for improved cellular infiltration. *Tissue Eng Part A, 17*(21-22), 2695-2702. doi:10.1089/ten.TEA.2010.0709

Lelah, M. D., Lambrecht, L. K., Young, B. R., & Cooper, S. L. (1983). Physicochemical characterization and in vivo blood tolerability of cast and extruded Biomer. *J Biomed Mater Res, 17*(1), 1-22. doi:10.1002/jbm.820170102

Lemos, P. A., Saia, F., Mariani Jr, J., Marrozzini, C., Filho, A. E., Kajita, L. J., Marzocchi, A. (2012). Residual aortic regurgitation is a major determinant of late mortality after transcatheter aortic valve implantation. *International Journal of Cardiology, 157*(2), 288-289. doi:http://dx.doi.org/10.1016/j.ijcard.2012.03.099

Leon, M. B., Piazza, N., Nikolsky, E., Blackstone, E. H., Cutlip, D. E., Kappetein, A. P., Serruys, P. W. (2011). Standardized endpoint definitions for transcatheter aortic valve implantation clinical trials: a consensus report from the Valve Academic Research Consortium. *Eur Heart J, 32*(2), 205-217. doi:10.1093/eurheartj/ehq406

Leopold, J. A. (2012). Cellular mechanisms of aortic valve calcification. *Circ Cardiovasc Interv, 5*(4), 605-614. doi:10.1161/CIRCINTERVENTIONS.112.971028

Lerakis, S., Hayek, S. S., & Douglas, P. S. (2013). Paravalvular aortic leak after transcatheter aortic valve replacement: current knowledge. *Circulation, 127*(3), 397-407. doi:10.1161/CIRCULATIONAHA.112.142000

Limited, R. T. (1999). *Polymers for the Medical Industry: A Two-day Conference Held at Church House Conference Centre, London, UK, 29th & 30th November 1999*: Rapra Technology Limited.

Liu, L., Li, D. B., Tong, Y. F., & Zhu, Y. F. (2017). The Influences of Assisting Gas Type and Process Parameters on the Fiber Laser Microprofiling of Thin CoCr Tubes for Vascular Stents. *Applied Sciences-Basel, 7*(6). doi:ARTN 60810.3390/app7060608

Lysaght, M., & Webster, T. J. (2010). *Biomaterials for Artificial Organs*: Elsevier Science.

Maganti, K., Rigolin, V. H., Sarano, M. E., & Bonow, R. O. (2010). Valvular Heart Disease: Diagnosis and Management. *Mayo Clinic Proceedings, 85*(5), 483-500. doi:10.4065/mcp.2009.0706

Martin, D. J., Meijs, G. F., Gunatillake, P. A., McCarthy, S. J., & Renwick, G. M. (1997). The effect of average soft segment length on morphology and properties of a series of polyurethane elastomers. II. SAXS-DSC annealing study. *Journal of Applied Polymer Science, 64*(4), 803-817. doi:10.1002/(SICI)1097-4628(19970425)64:4<803::AID-APP20>3.0.CO;2-T

Martin, D. J., Meijs, G. F., Gunatillake, P. A., Yozghatlian, S. P., & Renwick, G. M. (1999). The influence of composition ratio on the morphology of biomedical polyurethanes. *Journal of Applied Polymer Science, 71*(6), 937-952. doi:10.1002/(SICI)1097-4628(19990207)71:6<937::AID-APP9>3.0.CO;2-0

Martin, D. J., Meijs, G. F., Renwick, G. M., Gunatillake, P. A., & McCarthy, S. J. (1996). Effect of soft-segment CH2/O ratio on morphology and properties of a series of polyurethane elastomers. *Journal of Applied Polymer Science, 60*(4), 557-571. doi:10.1002/(SICI)1097-4628(19960425)60:4<557::AID-APP9>3.0.CO;2-N

Mazoochi, T., Ahmadi, S. M., hamadnian, M., & Jabbari, V. (2012). *Investigation on the Morphological Characteristic of Nanofiberous Membrane as Electrospun in the Different Processing Parameters* (Vol. 3).

Meredith Am, I. T., Walters, D. L., Dumonteil, N., Worthley, S. G., Tchetche, D., Manoharan, G., Dawkins, K. D. (2014). Transcatheter aortic valve replacement for severe symptomatic aortic stenosis using a repositionable valve system: 30-day primary endpoint results from the REPRISE II study. *J Am Coll Cardiol, 64*(13), 1339-1348. doi:10.1016/j.jacc.2014.05.067

Meredith Am, I. T., Walters, D. L., Dumonteil, N., Worthley, S. G., Tchétché, D., Manoharan, G., Dawkins, K. D. (2014). Transcatheter Aortic Valve Replacement for Severe Symptomatic Aortic Stenosis Using a Repositionable Valve System30-Day Primary Endpoint Results From the REPRISE II Study. *Journal of the American College of Cardiology, 64*(13), 1339-1348. doi:10.1016/j.jacc.2014.05.067

Merten, C., Beurich, H. W., Zachow, D., Mostafa, A. E., Geist, V., Toelg, R., Abdel-Wahab, M. (2013). Aortic regurgitation and left ventricular remodeling after transcatheter aortic valve implantation: a serial cardiac magnetic resonance imaging study. *Circ Cardiovasc Interv, 6*(4), 476-483. doi:10.1161/CIRCINTERVENTIONS.112.000115

Messika-Zeitoun, D., Serfaty, J. M., Brochet, E., Ducrocq, G., Lepage, L., Detaint, D., Vahanian, A. (2010). Multimodal assessment of the aortic annulus diameter: implications for transcatheter aortic valve implantation. *J Am Coll Cardiol, 55*(3), 186-194. doi:10.1016/j.jacc.2009.06.063

Michel, P. L., Vahanian, A., Besnainou, F., & Acar, J. (1987). Value of qualitative angiographic grading in aortic regurgitation. *Eur Heart J, 8 Suppl C*, 11-14. Retrieved from http://eurheartj.oxfordjournals.org/content/8/suppl_C/11.long

Milleret, V., Hefti, T., Hall, H., Vogel, V., & Eberli, D. (2012). Influence of the fiber diameter and surface roughness of electrospun vascular grafts on blood activation. *Acta Biomater, 8*(12), 4349-4356. doi:10.1016/j.actbio.2012.07.032

Milleret, V., Simona, B., Neuenschwander, P., & Hall, H. (2011). Tuning electrospinning parameters for production of 3D-fiber-fleeces with increased porosity for soft tissue engineering applications. *Eur Cell Mater, 21*, 286-303.

Mit-uppatham, C., Nithitanakul, M., & Supaphol, P. (2004). Effects of Solution Concentration, Emitting Electrode Polarity, Solvent Type, and Salt Addition on Electrospun Polyamide-6 Fibers: A Preliminary Report. *Macromolecular Symposia, 216*(1), 293-300. doi:10.1002/masy.200451227

Moat, N. E., Ludman, P., de Belder, M. A., Bridgewater, B., Cunningham, A. D., Young, C. P., Mullen, M. J. (2011). Long-term outcomes after transcatheter aortic valve implantation in high-risk patients with severe aortic stenosis: the U.K. TAVI (United Kingdom Transcatheter Aortic Valve Implantation) Registry. *J Am Coll Cardiol, 58*(20), 2130-2138. doi:10.1016/j.jacc.2011.08.050

Morganti, S., Brambilla, N., Petronio, A. S., Reali, A., Bedogni, F., & Auricchio, F. (2016). Prediction of patient-specific post-operative outcomes of TAVI procedure: The impact of the positioning strategy on valve performance. *Journal of Biomechanics, 49*(12), 2513-2519. doi:http://dx.doi.org/10.1016/j.jbiomech.2015.10.048

Morganti, S., Conti, M., Aiello, M., Valentini, A., Mazzola, A., Reali, A., & Auricchio, F. (2014). Simulation of transcatheter aortic valve implantation through patient-specific finite element analysis: Two clinical cases. *Journal of Biomechanics, 47*(11), 2547-2555. doi:http://dx.doi.org/10.1016/j.jbiomech.2014.06.007

Myerson, S. G., d'Arcy, J., Mohiaddin, R., Greenwood, J. P., Karamitsos, T. D., Francis, J. M., Neubauer, S. (2012). Aortic regurgitation quantification using cardiovascular magnetic resonance: association with clinical outcome. *Circulation, 126*(12), 1452-1460. doi:10.1161/circulationaha.111.083600

Mylotte, D., Martucci, G., & Piazza, N. (2012). Patient selection for transcatheter aortic valve implantation: An interventional cardiology perspective. *Ann Cardiothorac Surg, 1*(2), 206-215. Retrieved from http://www.annalscts.com/article/view/790

Nam, J., Huang, Y., Agarwal, S., & Lannutti, J. (2007). Improved cellular infiltration in electrospun fiber via engineered porosity. *Tissue Eng, 13*(9), 2249-2257. doi:10.1089/ten.2006.0306

Neragi-Miandoab, S., & Michler, R. E. (2013). A review of most relevant complications of transcatheter aortic valve implantation. *ISRN Cardiol, 2013*, 956252. doi:10.1155/2013/956252

Nezarati, R. M., Eifert, M. B., & Cosgriff-Hernandez, E. (2013a). Effects of Humidity and Solution Viscosity on Electrospun Fiber Morphology. *Tissue Engineering Part C: Methods, 19*(10), 810-819. doi:10.1089/ten.tec.2012.0671

Nezarati, R. M., Eifert, M. B., & Cosgriff-Hernandez, E. (2013b). Effects of Humidity and Solution Viscosity on Electrospun Fiber Morphology. *Tissue Engineering. Part C, Methods, 19*(10), 810-819. doi:10.1089/ten.tec.2012.0671

Ngadiman, N. H. A., Noordin, M. Y., Idris, A., Shakir, A. S. A., & Kurniawan, D. (2015). Influence of Polyvinyl Alcohol Molecular Weight on the Electrospun Nanofiber Mechanical Properties. *Procedia Manufacturing, 2*, 568-572. doi:https://doi.org/10.1016/j.promfg.2015.07.098

Nijenhuis, V. J., Swaans, M. J., Michiels, V., de Kroon, T., Heijmen, R. H., & ten Berg, J. M. (2015). “First experience with JenaValve™: a single-centre cohort”. *Netherlands Heart Journal, 23*(1), 35-41. doi:10.1007/s12471-014-0619-8

Niu, H., & Lin, T. (2012). Fiber Generators in Needleless Electrospinning. *Journal of Nanomaterials, 2012*, 13. doi:10.1155/2012/725950

Oğulata, R. T., & İçoğlu, H. İ. (2015). Interaction between effects of ambient parameters and those of other important parameters on electrospinning of PEI/NMP solution. *The Journal of The Textile Institute, 106*(1), 57-66. doi:10.1080/00405000.2014.902561

Okkema, A. Z., Yu, X. H., & Cooper, S. L. (1991). Physical and blood contacting characteristics of propyl sulphonate grafted Biomer. *Biomaterials, 12*(1), 3-12.

Padsalgikar, A., Cosgriff-Hernandez, E., Gallagher, G., Touchet, T., Iacob, C., Mellin, L., Runt, J. (2015). Limitations of predicting in vivo biostability of multiphase polyurethane elastomers using temperature-accelerated degradation testing. *J Biomed Mater Res B Appl Biomater, 103*(1), 159-168. doi:10.1002/jbm.b.33161

Pham, Q. P., Sharma, U., & Mikos, A. G. (2006). Electrospun poly(epsilon-caprolactone) microfiber and multilayer nanofiber/microfiber scaffolds: characterization of scaffolds and measurement of cellular infiltration. *Biomacromolecules, 7*(10), 2796-2805. doi:10.1021/bm060680j

Pibarot, P., & Dumesnil, J. G. (2009). Prosthetic heart valves: selection of the optimal prosthesis and long-term management. *Circulation, 119*(7), 1034-1048. doi:10.1161/CIRCULATIONAHA.108.778886

Pibarot, P., Hahn, R. T., Weissman, N. J., & Monaghan, M. J. (2015). Assessment of paravalvular regurgitation following TAVR: a proposal of unifying grading scheme. *JACC Cardiovasc Imaging, 8*(3), 340-360. doi:10.1016/j.jcmg.2015.01.008

Pinchuk, L., Martin, J. B., Esquivel, M. C., & Macgregor, D. C. (1988). The Use of Silicone/Polyurethane Graft Polymers as a Means of Eliminating Surface Cracking of Polyurethane Prostheses. *Journal of Biomaterials Applications, 3*(2), 260-296. doi:10.1177/088532828800300206

Prisacariu, C. (2011). Structural studies on polyurethane elastomers *Polyurethane Elastomers: From Morphology to Mechanical Aspects* (pp. 23-60). Vienna: Springer Vienna.

Prisacariu, C., Scortanu, E., & Prisacariu, A. (2010). Optimizing Physical and Chemical Properties of Hard Segment Reinforced Polyurethane Elastomers Via Control of Hydrogen Bonding. *Proceedings of the World Congress on Engineering 2010 Vol II WCE 2010, June 30 - July 2, 2010, London, U.K*.

Qin, X.-H., & Wang, S.-Y. (2006). Filtration properties of electrospinning nanofibers. *Journal of Applied Polymer Science, 102*(2), 1285-1290. doi:10.1002/app.24361

Rahmani, B., Tzamtzis, S., Sheridan, R., Mullen, M. J., Yap, J., Seifalian, A. M., & Burriesci, G. (2016). In Vitro Hydrodynamic Assessment of a New Transcatheter Heart Valve Concept (the TRISKELE). *J Cardiovasc Transl Res*. doi:10.1007/s12265-016-9722-0

Ratner, B. D., Hoffman, A. S., Schoen, F. J., & Lemons, J. E. (2012). *Biomaterials Science: An Introduction to Materials in Medicine*: Elsevier Science.

Ribeiro, H. B., Le Ven, F., Larose, E., Dahou, A., Nombela-Franco, L., Urena, M., . . . Rodes-Cabau, J. (2014). Cardiac magnetic resonance versus transthoracic echocardiography for the assessment and quantification of aortic regurgitation in patients undergoing transcatheter aortic valve implantation. *Heart, 100*(24), 1924-1932. doi:10.1136/heartjnl-2014-305615

Rnjak, J., Li, Z., Maitz, P. K. M., Wise, S. G., & Weiss, A. S. (2009). Primary human dermal fibroblast interactions with open weave three-dimensional scaffolds prepared from synthetic human elastin. *Biomaterials, 30*(32), 6469-6477. doi:http://dx.doi.org/10.1016/j.biomaterials.2009.08.017

Roy, D., Sharma, R., & Brecker, S. J. (2013). Native aortic valve regurgitation: transcatheter therapeutic options. *EuroIntervention, 9 Suppl*, S55-62. doi:10.4244/eijv9ssa11

Ruiz, C. E., Jelnin, V., Kronzon, I., Dudiy, Y., Del Valle-Fernandez, R., Einhorn, B. N., . . . Cohen, H. A. (2011). Clinical outcomes in patients undergoing percutaneous closure of periprosthetic paravalvular leaks. *J Am Coll Cardiol, 58*(21), 2210-2217. doi:10.1016/j.jacc.2011.03.074

Santerre, J. P., Woodhouse, K., Laroche, G., & Labow, R. S. (2005). Understanding the biodegradation of polyurethanes: from classical implants to tissue engineering materials. *Biomaterials, 26*(35), 7457-7470. doi:10.1016/j.biomaterials.2005.05.079

Schindelin, J., Arganda-Carreras, I., Frise, E., Kaynig, V., Longair, M., Pietzsch, T., Cardona, A. (2012). Fiji: an open-source platform for biological-image analysis. *Nat Meth, 9*(7), 676-682. doi:http://www.nature.com/nmeth/journal/v9/n7/abs/nmeth.2019.html#supplementary-information

Schultz, C. J., Moelker, A., Piazza, N., Tzikas, A., Otten, A., Nuis, R. J., de Jaegere, P. P. T. (2010). Three dimensional evaluation of the aortic annulus using multislice computer tomography: are manufacturer's guidelines for sizing for percutaneous aortic valve replacement helpful? *European Heart Journal, 31*(7), 849-856. doi:10.1093/eurheartj/ehp534

Schultz, C. J., Tzikas, A., Moelker, A., Rossi, A., Nuis, R. J., Geleijnse, M. M., de Jaegere, P. P. (2011). Correlates on MSCT of paravalvular aortic regurgitation after transcatheter aortic valve implantation using the Medtronic CoreValve prosthesis. *Catheter Cardiovasc Interv, 78*(3), 446-455. doi:10.1002/ccd.22993

Schymik, G., Schrofel, H., Heimeshoff, M., Luik, A., Thoenes, M., & Mandinov, L. (2015). How to adapt the implantation technique for the new SAPIEN 3 transcatheter heart valve design. *J Interv Cardiol, 28*(1), 82-89. doi:10.1111/joic.12165

Scotten, L. N., & Siegel, R. (2014). Thrombogenic potential of transcatheter aortic valve implantation with trivial paravalvular leakage. *Ann Transl Med, 2*(5), 43. doi:10.3978/j.issn.2305-5839.2014.05.04

Sellers, R. D., Levy, M. J., Amplatz, K., & Lillehei, C. W. (1964). Left retrograde cardioangiography in acquired cardiac disease: Technic, indications and interpretations in 700 cases. *Am J Cardiol, 14*, 437-447.

Seo, E. H., & Na, K. (2014). Polyurethane membrane with porous surface for controlled drug release in drug eluting stent. *Biomaterials Research, 18*(1), 1-5. doi:10.1186/2055-7124-18-15

Shah, S., Gnanasegaran, G., Sundberg-Cohon, J., & Buscombe, J. R. (2009). The Heart: Anatomy, Physiology and Exercise Physiology. In A. Movahed, G. Gnanasegaran,

J. Buscombe, & M. Hall (Eds.), *Integrating Cardiology for Nuclear Medicine Physicians* (pp. 3-22): Springer Berlin Heidelberg.

Sherif, M. A., Abdel-Wahab, M., Stöcker, B., Geist, V., Richardt, D., Tölg, R., & Richardt, G. (2010). Anatomic and Procedural Predictors of Paravalvular Aortic Regurgitation After Implantation of the Medtronic CoreValve Bioprosthesis. *Journal of the American College of Cardiology, 56*(20), 1623-1629. doi:http://dx.doi.org/10.1016/j.jacc.2010.06.035

Sill, T. J., & von Recum, H. A. (2008). Electrospinning: Applications in drug delivery and tissue engineering. *Biomaterials, 29*(13), 1989-2006. doi:https://doi.org/10.1016/j.biomaterials.2008.01.011

Simonet, M., Schneider, O. D., Neuenschwander, P., & Stark, W. J. (2007). Ultraporous 3D polymer meshes by low-temperature electrospinning: Use of ice crystals as a removable void template. *Polymer Engineering & Science, 47*(12), 2020-2026. doi:10.1002/pen.20914

Sinning, J.-M., Hammerstingl, C., Vasa-Nicotera, M., Adenauer, V., Lema Cachiguango, S. J., Scheer, A.-C., . . . Werner, N. (2012). Aortic Regurgitation Index Defines Severity of Peri-Prosthetic Regurgitation and Predicts Outcome in Patients After Transcatheter Aortic Valve Implantation. *Journal of the American College of Cardiology, 59*(13), 1134-1141. doi:10.1016/j.jacc.2011.11.048

Sinning, J. M., Vasa-Nicotera, M., Chin, D., Hammerstingl, C., Ghanem, A., Bence, J., Werner, N. (2013). Evaluation and management of paravalvular aortic regurgitation after transcatheter aortic valve replacement. *J Am Coll Cardiol, 62*(1), 11-20. doi:10.1016/j.jacc.2013.02.088

Sisson, K., Zhang, C., Farach-Carson, M. C., Chase, D. B., & Rabolt, J. F. (2010). Fiber diameters control osteoblastic cell migration and differentiation in electrospun gelatin. *J Biomed Mater Res A, 94*(4), 1312-1320. doi:10.1002/jbm.a.32756

Sliwa, K., & Zilla, P. (2012). Rheumatic heart disease: the tip of the iceberg. *Circulation, 125*(25), 3060-3062. doi:10.1161/CIRCULATIONAHA.112.114199

Smith , C. R., Leon , M. B., Mack , M. J., Miller , D. C., Moses , J. W., Svensson , L. G., Pocock , S. J. (2011). Transcatheter versus Surgical Aortic-Valve Replacement in High-Risk Patients. *New England Journal of Medicine, 364*(23), 2187-2198. doi:doi:10.1056/NEJMoa1103510

Smolka, G., Pysz, P., Jasinski, M., Roleder, T., Peszek-Przybyla, E., Ochala, A., & Wojakowski, W. (2016). Multiplug paravalvular leak closure using Amplatzer Vascular Plugs III: A prospective registry. *Catheter Cardiovasc Interv, 87*(3), 478-487. doi:10.1002/ccd.25992

Soliman, S., Sant, S., Nichol, J. W., Khabiry, M., Traversa, E., & Khademhosseini, A. (2011). Controlling the porosity of fibrous scaffolds by modulating the fiber diameter and packing density. *J Biomed Mater Res A, 96*(3), 566-574. doi:10.1002/jbm.a.33010

Stähli, B. E., Maier, W., Corti, R., Lüscher, T. F., Jenni, R., & Tanner, F. C. (2013). Aortic regurgitation after transcatheter aortic valve implantation: mechanisms and implications. *Cardiovascular Diagnosis and Therapy, 3*(1), 15-22. Retrieved from http://cdt.amegroups.com/article/view/1552

Stokes, K., & Cobian, K. (1982). Polyether polyurethanes for implantable pacemaker leads. *Biomaterials, 3*(4), 225-231. doi:http://dx.doi.org/10.1016/0142-9612(82)90024-2

Stokes, K., Coury, A., & Urbanski, P. (1987). Autooxidative degradation of implanted polyether polyurethane devices. *J Biomater Appl, 1*(4), 411-448.

Stokes, K., McVenes, R., & Anderson, J. M. (1995). Polyurethane elastomer biostability. *J Biomater Appl, 9*(4), 321-354. doi:10.1177/088532829500900402

Stokes, K., Urbanski, P., & Upton, J. (1990). The in vivo auto-oxidation of polyether polyurethane by metal ions. *J Biomater Sci Polym Ed, 1*(3), 207-230.

Sturla, F., Ronzoni, M., Vitali, M., Dimasi, A., Vismara, R., Preston-Maher, G., Redaelli, A. (2016). Impact of different aortic valve calcification patterns on the outcome of transcatheter aortic valve implantation: A finite element study. *Journal of Biomechanics*. doi:http://dx.doi.org/10.1016/j.jbiomech.2016.03.036

Sun, B., Jiang, X.-J., Zhang, S., Zhang, J.-C., Li, Y.-F., You, Q.-Z., & Long, Y.-Z. (2015). Electrospun anisotropic architectures and porous structures for tissue engineering. *J. Mater. Chem. B, 3*(27), 5389-5410. doi:10.1039/c5tb00472a

Sundermann, S. H., Grunenfelder, J., Corti, R., Rastan, A. J., Linke, A., Lange, R., Bleiziffer, S. (2012). Feasibility of the Engager aortic transcatheter valve system using a flexible over-the-wire design. *Eur J Cardiothorac Surg, 42*(4), e48-52. doi:10.1093/ejcts/ezs389

Sundermann, S. H., Holzhey, D., Bleiziffer, S., Treede, H., Jacobs, S., & Falk, V. (2014). Second-generation transapical valves: the Medtronic Engager system. *Multimedia Manual of Cardio-Thoracic Surgery, 2014*(0), mmu001-mmu001. doi:10.1093/mmcts/mmu001

Theron, S. A., Yarin, A. L., Zussman, E., & Kroll, E. (2005). Multiple jets in electrospinning: experiment and modeling. *Polymer, 46*(9), 2889-2899. doi:http://dx.doi.org/10.1016/j.polymer.2005.01.054

Tillquist, M. N., & Maddox, T. M. (2011). Cardiac crossroads: deciding between mechanical or bioprosthetic heart valve replacement. *Patient Prefer Adherence, 5*, 91-99. doi:10.2147/PPA.S16420

Treede, H., Mohr, F. W., Baldus, S., Rastan, A., Ensminger, S., Arnold, M., Figulla, H. R. (2012). Transapical transcatheter aortic valve implantation using the JenaValve system: acute and 30-day results of the multicentre CE-mark study. *Eur J Cardiothorac Surg, 41*(6), e131-138. doi:10.1093/ejcts/ezs129

Tzikas, A., Chrissoheris, M., Halapas, A., & Spargias, K. (2014). Next Generation Transcatheter Aortic Valve Systems: the PorticoTM Valve. *Hospital Chronicles, 9*, 154-156.

Ushiki, T. (2002). Collagen fibers, reticular fibers and elastic fibers. A comprehensive understanding from a morphological viewpoint. *Arch Histol Cytol, 65*(2), 109-126. Retrieved from https://www.jstage.jst.go.jp/article/aohc/65/2/65_2_109/_pdf

Vahidkhah, K., & Azadani, A. (2016). TCT-710 Drawback of the Circumferential Extent of Paravalvular Regurgitation as a Semi-quantitative Parameter to Evaluate the Severity of Transcatheter Aortic Valve Leakage. *Journal of the American College of Cardiology, 68*(18_S), B287-B288. doi:10.1016/j.jacc.2016.09.123

Van Belle, E., Juthier, F., Susen, S., Vincentelli, A., Iung, B., Dallongeville, J., Teiger, E. (2014). Post-Procedural Aortic Regurgitation in Balloon-expandable and Self-Expandable TAVR Procedures: Analysis of Predictors and Impact on Long-Term Mortality: Insights from the FRANCE2 Registry. *Circulation*. doi:10.1161/circulationaha.113.002677

van Geldorp, M. W. A., Eric Jamieson, W. R., Kappetein, A. P., Ye, J., Fradet, G. J., Eijkemans, M. J. C., Takkenberg, J. J. M. (2008). Patient outcome after aortic valve replacement with a mechanical or biological prosthesis: Weighing lifetime anticoagulant-related event risk against reoperation risk. *The Journal of Thoracic and Cardiovascular Surgery, 137*(4), 881-886.e885. doi:10.1016/j.jtcvs.2008.09.028

Vaquette, C., & Cooper-White, J. J. (2011). Increasing electrospun scaffold pore size with tailored collectors for improved cell penetration. *Acta Biomater, 7*(6), 2544-2557. doi:10.1016/j.actbio.2011.02.036

Vavouranakis, M., Vrachatis, D. A., Toutouzas, K. P., Chrysohoou, C., & Stefanadis, C. (2010). "Bail out" procedures for malpositioning of aortic valve prosthesis (CoreValve). *Int J Cardiol, 145*(1), 154-155. doi:10.1016/j.ijcard.2009.07.040

Voorneveld, J., Oosthuysen, A., Franz, T., Zilla, P., & Bezuidenhout, D. (2016). Dual electrospinning with sacrificial fibers for engineered porosity and enhancement of tissue ingrowth. *Journal of Biomedical Materials Research Part B: Applied Biomaterials*, n/a-n/a. doi:10.1002/jbm.b.33695

Wang, N., Burugapalli, K., Song, W., Halls, J., Moussy, F., Zheng, Y., Li, K. (2013). Tailored fibro-porous structure of electrospun polyurethane membranes, their size-dependent properties and trans-membrane glucose diffusion. *Journal of membrane science, 427*, 207-217. doi:10.1016/j.memsci.2012.09.052

Ward, B., Anderson, J., Ebert, M., McVenes, R., & Stokes, K. (2006). In vivo biostability of polysiloxane polyether polyurethanes: Resistance to metal ion oxidation. *Journal of Biomedical Materials Research Part A, 77A*(2), 380-389. doi:10.1002/jbm.a.30553

Webb, J. G., & Binder, R. K. (2012). Post-dilating transcatheter heart valves. *JACC Cardiovasc Interv, 5*(5), 513-514. doi:10.1016/j.jcin.2012.02.011

Wilczek, K., Bujak, K., Reguła, R., Chodór, P., & Osadnik, T. (2015). Risk factors for paravalvular leak after transcatheter aortic valve implantation. *Kardiochirurgia i Torakochirurgia Polska = Polish Journal of Cardio-Thoracic Surgery, 12*(2), 89-94. doi:10.5114/kitp.2015.52848

Wu, J., & Hong, Y. (2016). Enhancing cell infiltration of electrospun fibrous scaffolds in tissue regeneration. *Bioactive Materials*. doi:http://dx.doi.org/10.1016/j.bioactmat.2016.07.001

Wu, Y., Dong, Z., Wilson, S., & Clark, R. (2010). *Template-assisted assembly of electrospun fibers* (Vol. 51).

Xie, J., Li, X., & Xia, Y. (2008). Putting Electrospun Nanofibers to Work for Biomedical Research. *Macromolecular rapid communications, 29*(22), 1775-1792. doi:10.1002/marc.200800381

Yang, J., Gao, Y., Li, J., Ding, M., Chen, F., Tan, H., & Fu, Q. (2013). Synthesis and microphase separated structures of polydimethylsiloxane/polycarbonate-based polyurethanes. *RSC Advances, 3*(22), 8291-8297. doi:10.1039/C3RA40515J

Ye, J., Soon, J. L., & Webb, J. (2012). Aortic valve replacement vs. transcatheter aortic valve implantation: Patient selection. *Annals of Cardiothoracic Surgery, 1*(2), 194-199. Retrieved from http://www.annalscts.com/article/view/788

Yuan, Y. T., Chen, Y. H., Chen, P. L., Tsai, H. C., Chen, I. M., Weng, Z. C., Chang, H. H. (2013). One-year results of transcatheter aortic valve implantation as an alternative treatment for severe aortic stenosis in high-risk patients. *J Chin Med Assoc, 76*(12), 698-702. doi:10.1016/j.jcma.2013.08.007

Zamorano, J. L., Badano, L. P., Bruce, C., Chan, K. L., Goncalves, A., Hahn, R. T., Gillam, L. D. (2011). EAE/ASE recommendations for the use of echocardiography in new transcatheter interventions for valvular heart disease. *J Am Soc Echocardiogr, 24*(9), 937-965. doi:10.1016/j.echo.2011.07.003

Zhang, C., Hu, J., Chen, S., & Ji, F. (2010). Theoretical study of hydrogen bonding interactions on MDI-based polyurethane. *Journal of Molecular Modeling, 16*(8), 1391-1399. doi:10.1007/s00894-010-0645-4

Zhao, Q., Casas-Bejar, J., Urbanski, P., & Stokes, K. (1995). Glass wool-H2O2/CoCl2 test system for in vitro evaluation of biodegradative stress cracking in polyurethane elastomers. *J Biomed Mater Res, 29*(4), 467-475. doi:10.1002/jbm.820290406

Zhu, R., Wang, Y., Zhang, Z., Ma, D., & Wang, X. (2016). Synthesis of polycarbonate urethane elastomers and effects of the chemical structures on their thermal, mechanical and biocompatibility properties. *Heliyon, 2*(6), e00125. doi:10.1016/j.heliyon.2016.e00125

Zilla, P. P., & Greisler, H. P. (1999). *Tissue Engineering of Vascular Prosthetic Grafts*: R.G. Landes Company.

Zoghbi, W. (2003). American Society of Echocardiography: recommendations for evaluation of the severity of native valvular regurgitation with two-dimensional and Doppler echocardiography A report from the American Society of Echocardiography's Nomenclature and Standards Committee and The Task Force on Valvular Regurgitation, developed in conjunction with the American College of Cardiology Echocardiography Committee, The Cardiac Imaging Committee, Council on Clinical Cardiology, The American Heart Association, and the European Society of Cardiology Working Group on Echocardiography, represented by. *European Journal of Echocardiography, 4*(4), 237-261. doi:10.1016/j.euje.2003.07.001

Zoghbi, W. A., Chambers, J. B., Dumesnil, J. G., Foster, E., Gottdiener, J. S., Grayburn, P. A., Zabalgoitia, M. (2009). Recommendations for evaluation of prosthetic valves with echocardiography and doppler ultrasound: a report From the American Society of

Echocardiography's Guidelines and Standards Committee and the Task Force on Prosthetic Valves, developed in conjunction with the American College of Cardiology Cardiovascular Imaging Committee, Cardiac Imaging Committee of the American Heart Association, the European Association of Echocardiography, a registered branch of the European Society of Cardiology, the Japanese Society of Echocardiography and the Canadian Society of Echocardiography, endorsed by the American College of Cardiology Foundation, American Heart Association, European Association of Echocardiography, a registered branch of the European Society of Cardiology, the Japanese Society of Echocardiography, and Canadian Society of Echocardiography. *J Am Soc Echocardiogr, 22*(9), 975-1014; quiz 1082-1014. doi:10.1016/j.echo.2009.07.013